2015

Real-time source tracking for quality assurance in HDR prostate brachytherapy

Zhangbo Han
University of Wollongong, zh594@uowmail.edu.au

University of Wollongong 

REAL-TIME SOURCE TRACKING FOR QUALITY ASSURANCE IN HDR PROSTATE BRACHYTHERAPY

A Dissertation Submitted in Fulfilment of
the Requirements for the Award of the Degree of

Doctor of Philosophy

from

UNIVERSITY OF WOLLONGONG

by

Zhangbo Han

Bachelor of Science (Mathematics and Applied Mathematics)
Tianjin Normal University, 2008
Master of Medical Radiation Physics
University of Wollongong, 2010

Centre for Medical Radiation Physics
Faculty of Engineering and Information Sciences

2015

Dedicated to

My family

Table of Contents

List of Tables

List of Figures

Abbreviation

AAPM	American Association of Physicists in Medicine
ABS	American Brachytheapy Society
ACIM	Australian Cancer Incidence and Mortality workbooks
AIHW	Australian Institute of health and Welfare
AJCC	American Joint Committee on Cancer
BSDF	Backscatter dose fraction
BT	Brachytherapy
CCD	Charge-coupled device
CIRS	Computerized Imaging Reference Systems
CMRP	Centre for Medical Radiation Physics
CoG	Geometrical centre
CoM	Centre of mass
CoM_i	Ideal centre of mass
CRT	Conformal radiation therapy
DHT	Dihydrotestosterone
DRE	Digital rectal examination
DSP	Direct source projection
EBRT	External bean radiotherapy
ESP	Extensive source projection
ESTRO	The European Society for Radiotherapy and Oncology
FoV	Field of view
FWHM	Full width at half maximum
HDR	High dose rate
IAEA	International Atomic Energy Agency
IGRT	Image-guided radiation therapy
IMRT	Intensity modulated radiation therapy
ISUP	International Society of Urological Pathology
LCP	The line determined by the CoM and the centre of its corresponding pinhole
LDR	Low dose rate
LET	Linear energy transfer
LH	Luteinizing hormone
LHRH	Luteinizing hormone - releasing hormone
LRP	Laparoscopic radical prostatectomy
MOSFET	Metal oxide semiconductor field effect transistor

NIST	National Institute of Standards and Technology
ORP	Open radical prostatectomy
PAP	Prostate acid phosphatas
PBT	Prostate brachytherapy
PCB	Printed circuit board
PCR	Pixel Configuration Register
PMMA	Polymethylmethacrylate
PP	Penetration penumbra
PSA	Prostate specific antigen
PSD	Plastic scintillation detector
PSS	Penetration source shadow
QA	Quality assurance
SD	Standard deviation
SBR	Signal to background ratio
SDD	Source to detector distance
SEM	Error of the sample mean
SNR	Signal to noise ratio
TLD	Thermoluminescent detector
ToA	Time of arrival mode
ToT	Time over threshold mode
TRUS	Transrectal ultrasound
TSSE	Thermally stimulated exoelectron mission
WED	Water-equivalent depth

Real-time Source Tracking for Quality Assurance in HDR Prostate Brachytherapy

Zhangbo Han

A Thesis for Doctor of Philosophy

Centre for Medical Radiation Physics
University of Wollongong

ABSTRACT

High dose rate (HDR) brachytherapy is the preferred treatment option for clinically localised prostate cancer. The underlying principle is simple: temporarily inserting a highly radioactive source inside the target volume and moving it through a sequence of predefined positions for pre-calculated dwell times. HDR brachytherapy is capable of achieving a highly conformal dose distribution which cannot be matched by external beam radiation therapy.

The success of HDR prostate brachytherapy treatment is highly dependent on the accuracy of source placement within the prostate volume. In addition, ensuring minimum deviation from the planned source positions relative to the prostate minimises the occurrence and severity of radiation toxicity in nearby organs such as the rectum, urethra and bladder.

Several factors can result in an incorrect dose distribution, such as anatomical changes between the time of planning and surgery, human error in measuring and entering data to the afterloader system and changes in catheter location during the treatment or between fractions. Therefore, a quality assurance method which can perform accurate real-time source tracking will greatly assist in providing better target coverage with reduced acute and secondary side effects.

In this Thesis, *HDR BrachyView* , a novel intra-fraction source position monitoring system for quality assurance in HDR prostate brachytherapy, is presented. *HDR BrachyView* is an in-body (trans-rectal) imaging system which is capable of independently tracking the source position within the target volume in real time during the source delivery operation. It consists of a multi-pinhole tungsten collimator which projects images of the source onto an array of high resolution pixelated silicon detectors (Timepix). The source position within the treatment volume is calculated by back-projecting the centres of mass of the recorded projections through the corresponding pinholes.

The design of *HDR BrachyView* is presented, followed by extensive validation and characterisation via detailed Monte Carlo simulations. Preliminary experimental results from a prototype of *HDR BrachyView* confirm that the device is capable of monitoring the source position with sub-millimetre accuracy within a sub-second acquisition time.

KEYWORDS: Prostate Cancer, HDR brachytherapy, Quality Assurance

Acknowledgements

My deepest gratitude goes to my supervisors, Dr. Mitra Safavi-Naeini, Professor Anatoly Rosenfeld and Associate Professor Michael Lerch, for their strong and clear guidance. Their have walked me through all the stages of my Ph.D. project with their brilliant ideas and rigorous supervision. This thesis won't be possible without their consistent and illuminating instruction.

I would like to express my heartfelt gratitude to Dr. Dean Cutajar, Dr. Susanna Guatelli and Dr. Marco Petasecca, for all their advice and support. It was the Geant4 workshop held by Dean and Susanna brought me into the world of Monte Carlo simultion.

My gratitude would also go to Kaiyang Li, Kevin Loo and Saree Alnaghy, for all the interesting discussions through my Ph.D. study.

In addition, I would like to thank all other CMRP members, especially Karen Ford. Her outstanding skill in administration ensured the smooth running of our centre and made us able to focus on our research.

Last my thanks would go to my beloved family for their loving considerations, unconditional support and great confidence in me all through these years.

Chapter 1

Introduction

The discovery of ionising radiation and its toxicity to cells has inspired the development of radiation therapy as an alternative or complementary method to surgical interventions in the treatment of cancer. It avoids incision or resection of the diseased organ, and due to its penetrative nature provides a mechanism for reaching deep-seated tumours. However, radiation deposits energy along its path which also damages healthy tissue and may lead to serious complications, including the induction of secondary cancers. Therefore, conformal delivery of the radiation to the target volume (i.e. the cancerous region) is an important goal in radiotherapy.

Brachytherapy is a radiation delivery technique capable of providing excellent dose conformity within the target volume. It involves the pre-implantation of a matrix of catheters directly into the target volume. Depending on whether the form of brachytherapy is low dose rate (LDR) or high dose rate (HDR), radioactive material is either permanently implanted (LDR) or sequentially stepped through a series of positions within each catheter. The desired dose distribution is achieved by the permanent position of multiple radioactive seeds (in the case of LDR brachytherapy) or by the positions occupied by the source and the dwell time in each position (in the case of HDR brachytherapy). Ensuring that the planned dose distribution is correctly

administered to the target organ is critically dependent on the accuracy of source positioning with respect to the target organ. Improper radioactive source placement (^{192}Ir in case of HDR, ^{125}I or ^{103}Pd in case of LDR brachytherapy) may result in sub-optimal treatment of the cancer while potentially resulting in radiation toxicity to nearby organs.

Brachytherapy treatment is particularly well-suited to the treatment of prostate cancer. The anatomical location of the prostate facilitates the insertion of catheters, and its proximity to critical organs (including the rectum, urethra and bladder) necessitates excellent dose conformity. Errors in dose delivery may lead to post-treatment complications such as incontinence and sexual dysfunction.

Although both forms of brachytherapy are widely used for treating prostate cancer, HDR brachtherapy has a number of advantages over LDR brachytherapy. In particular, it results in much less exposure of clinicians to radiation, as the source is sequentially moved through each of the catheters by an automated afterloader, and is retracted within a shielded enclosure before and after treatment. Additionally, there is some clinical evidence that prostate cancer is more effectively treated with a small number of high-dose fractions rather than continuous low dose irradiation over a longer time period. This Thesis exclusively deals with HDR prostate brachytherapy (HDR-PBT).

During a typical HDR-PBT procedure, the patient is anaesthetised while 18 to 25 catheters are inserted into the prostate gland, guided by a transrectal ultrasound (TRUS) image. A post-implant CT scan of the prostate is used to confirm the relative positioning of the catheters with respect to the prostate; this is also used by the treatment planning system (TPS) to calculate the specific duration and placement of the radioactive source within each of the catheters. Typically, two to three dose fractions are delivered within 24 hours, during which the catheters are connected to

the afterloader system. Although the patient is kept immobile during the procedure (on the hospital bed), catheter displacement still occurs during the interval between the catheter implantation and the source delivery. Penetration of the bladder wall can reduce the catheter movement and a repeat of the CT scans prior to the subsequent dose fractions may be used to update the treatment plan. Anatomical changes and movements may still result in a change in catheter position between treatment planning and the source delivery. In addition, afterloader uncertainty ($\pm$1 mm), the possibility of human error and afterloader malfunction all may result in significant differences between the planned and delivered dose distributions, incidents of which have been reported in previously published literature.

A reliable, accurate, real-time system for continuous independent monitoring of the source position during the HDR-PBT procedure would be an important advance in quality assurance (QA) and for prostate brachytherapy treatment. It would allow the clinician to terminate or modify the treatment plan if anomalous source movement is detected. To date, most current methods for providing real-time three dimensional source position information are based on external imaging systems. The large distance between the prostate and the detector in these systems leads to either a significant uncertainty in the determination of source position or an acquisition time exceeding that required for real-time source position monitoring.

An alternative approach is to insert the source imaging system into the patient's body. A concept of in-body imaging system for source tracking using highly spatial resolution pixelated solid state detector was proposed at Centre for Medical Radiation Physics (CMRP) by Prof. Anatoly Rosenfeld. The proximity of prostate to rectum provides an ideal opportunity for the use of an in-body imaging system for HDR-PBT. In-body imaging reduces the target-to-detector distance by a factor of four compared to external imaging systems, and significantly reduces the acquisition time by reducing

the signal attenuation. Additionally, by combining the source imaging system with a colocated TRUS probe, it is straightforward to co-register the source position with the prostate volume and minimise the impact of patient movement on the accuracy of the tracked source position.

1.1 Objectives, Overview of this Thesis

The principal objective of this Thesis is to develop a robust, high-accuracy, real-time in-body (trans-rectal) source imaging and position monitoring system for HDR prostate brachytherapy intra-fraction QA. The main challenge in the design of such a system is the limited space available inside the rectum, which places severe constraints on the dimensions and composition of the components of the imaging system. The image analysis and source tracking algorithms are also critical factors in the correct performance of the system; each of these aspects is comprehensively investigated in this Thesis. To ensure the safety of using the proposed system during the source delivery, the additional dose delivered to the patient as a result of backscatter radiation from the collimator was also thoroughly evaluated via simulation and experimental studies. Based on these results, a prototype trans-rectal probe, *HDR BrachyView* , was designed and fabricated.

The device consists of an array of four Timepix detectors (with a total sensitive area of 14 mm $\times$ 56 mm), placed within a 4 mm thick, multi-pinhole cylindrical tungsten collimator and encased within a thin rigid shell made of medical grade sterilisable plastic. For every source position, multiple projection images are recorded by the detector array. By backprojecting the centres of mass (CoMs) through the corresponding pinholes, the 3-dimensional position of the source is determined. To accommodate the poor signal to background ratio (SBR) obtained with a pinhole collimator yet still provide accurate source monitoring within a sub-second acquisition time, a novel seg-

mentation and thresholding method was developed to isolate all the projections from background signal. The design of the *HDR BrachyView* probe, together with the short prostate to detector distance results in a system capable of obtaining the source position with sub-millimetre accuracy within a sub-second dwell time

The design of *HDR BrachyView* was evaluated by extensive validation and characterisation through detailed Monte Carlo simulations. Preliminary experimental studies were conducted with a prototype probe, which confirm the results of the simulation studies. *HDR BrachyView* has been was recognised by the European Society for Radiotherapy & Oncology (ESTRO) and American Brachytherapy Society (ABS) as one of the most important recent advances in assisting with the provision of high quality brachytherapy.

1.2 Structure and Summary of Contributions of this Thesis

The thesis is divided into the following Chapters:

- Chapter 2 presents a comprehensive literature review.
- Chapters 3 and 4 present the details of *HDR BrachyView* design, and the methods for image analysis and 3-dimensional source tracking.

  Z. Han, M. Safavi-Naeini, M. Petasecca, D. Cutajar, K. Loo, M. Lerch, J.A. Bucci, A.B. Rosenfeld, "*BrachyView* for High Dose Rate (HDR) Brachytherapy," in *21st Annual Scientific Meeting of the Australasaian Brachytherapy Group*, March, 2012

- Chapters 5 presents the evaluation of the effect of dose enhancement on rectum wall due to the back-scatter radiation from *HDR BrachyView* probe. This work

has resulted in the following publications:

Z. Han, M. Safavi-Naeini, S. Alnaghy, D. Cutajar, S. Guatelli, M. Petasecca, D. Franklin, A. Malaroda, M. Carrara, J. Bucci, M. Zaider, M. Lerch, A. Rosenfeld, "Radiation dose enhancement at tissue-tungsten interfaces in HDR brachytherapy," *Physics in Medicine and Biology*, vol. 59, no. 21, pp. 6659, 2014.

Z. Han, M. Safavi-Naeini, S. Alnagy, D. Cutajar, S. Guatelli, M. Petasecca, M. Lerch, D.R. Franklin, J.A. Bucci, M. Zaider, A.B. Rosenfeld, "Dose Enhancement at tungsten-tissue interfaces with ^{192}Ir source in HDR brachytherapy," in *Nuclear Science Symposium and Medical Imaging Conference (NSS/MIC), 2014 IEEE*, 2014

- Chapters 6 and 7 present the validation of *HDR BrachyView* probe design through simulation and experimental investigation, and have resulted in the following publications:

  Z. Han, M. Safavi-Naeini, M. Petasecca, M. Lerch, D. Cutajar, S. Guatelli, J.A. Bucci, A.B. Rosenfeld, "*BrachyView* : Real-time Quality Assurance for HDR Prostate Brachytherapy," in *Engineering & Physical Sciences in Medicine Conference (EPSM)*, December, 2012

  M. Safavi-Naeini, Z. Han, D. Cutajar, S. Guatelli, M. Petasecca, M. Lerch, D. Franklin, J. Bucci, M. Zaider, A. Rosenfeld, "BrachyView, a novel inbody imaging system for HDR prostate brachytherapy: design and Monte Carlo feasibility study," *Medical Physics*, vol. 40, pp. 071715, 2013

  Z. Han, M. Safavi-Naeini, S. Alnaghy, D. Cutajar, S. Guatelli, M. Petasecca, M. Lerch, D. Franklin, M. Carrara, J. Bucci, M. Zaider, A. Rosenfeld, "BrachyView, A novel inbody imaging system for HDR prostate brachytherapy: Experimental evaluation," *Physics in Medicine and Biology*, 2015 (submitted)

Z. Han, M. Safavi-Naeini, M. Petasecca, D. Cutajar, M. Lerch, D. Franklin, J. Jakubek, J. Zemlicka, S. Pospisil, J. Bucci, M. Zaider, A. Rosenfeld, "Brachyview: An in-body imaging system for real-time QA in HDR prostate brachytherapy," in *Nuclear Science Symposium and Medical Imaging Conference Record (NSS/MIC), 2013 IEEE*, 2013, pp. 1-4

- Chapter 8 presents a concluding summary of this thesis and offers suggestions for potential future work.

Chapter 2

Literature review

This Chapter presents a comprehensive literature review. It starts with a brief discussion of the prostate and prostate cancer (Section 2.1), followed by an introduction to the main treatment options - namely, surgery, hormonal therapy and radiation therapy, with a particular focus on high dose rate prostate brachytherapy (HDR-PBT) (Section 2.2). Section 2.3 reviews a number of studies of the problem of source misplacement in HDR-PBT. Finally, quality assurance methods specifically designed for HDR brachytherapy are reviewed in detail in Section 2.4.

2.1 Prostate and Prostate Cancer

2.1.1 The Anatomy and Function of the Prostate

The prostate is a walnut-shaped glandular organ found in males[1] of most species, with a maximum diameter in humans of around 40 mm. It is located anterior to the rectum and immediately inferior to the bladder. The prostate encircles the urethra as it exits the bladder and the ejaculatory duct as it exits the seminal vesicle [1, 2]. The

[1] A female homolog to the prostate gland, formerly known as Skeane's gland, also exists, however it is much less susceptible to cancer compared to the male organ.

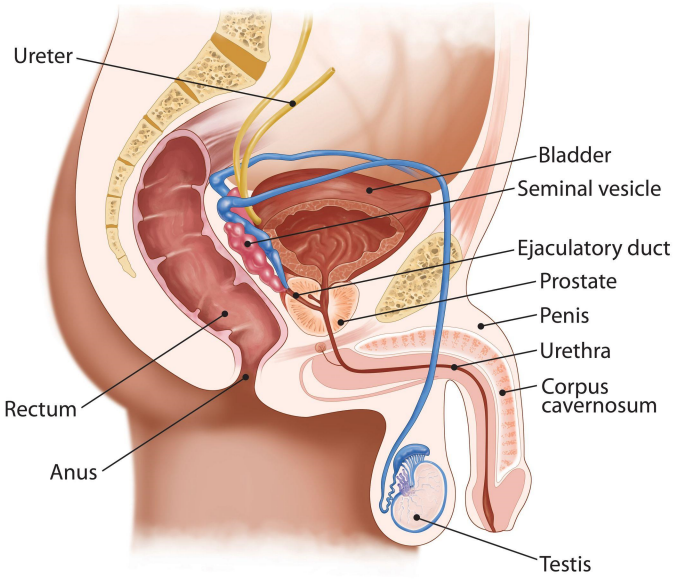

Figure 2.1: Sagittal cross-section showing prostate anatomy.

primary function of the prostate relates to the secretion of alkaline ejaculatory fluids; it also includes smooth muscle which assists the expulsion of semen during ejaculation Figure 2.1 and 2.2 illustrate the anatomy of the prostate in the sagittal and transverse planes.

The peri-prostatic anatomy of the prostate is shown in Figure 2.2. The distance between the posterior wall of the prostate and the anterior wall of the rectum in healthy male adults is approximately 5.8 ± 0.7 mm. This space is primarily occupied by fat tissue and venous plexus [4]. The median thickness of healthy rectal wall is approximately 2.6 mm [5].

2.1.2 Incidence and Mortality of Prostate Cancer in Australia

The first mention of prostate cancer recorded in medical literature is from 1853, 315 years after the first description of the prostate gland itself [6]. Currently, prostate cancer is one of the most common cancers diagnosed in Australia. Statistical data on the incidence (to 2010) and mortality (to 2011) for all categories of cancer have been

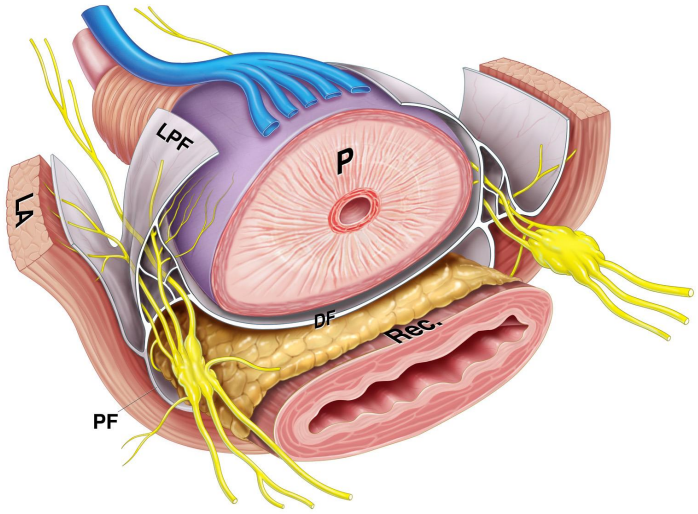

Figure 2.2: Transverse cross-section illustrating the peri-prostatic anatomy. The abbreviations are: Denonviller's fascia (DF), levator ani (LA), lateral prostatic fascia (LPF), pararectal fat (PF), prostate (P), rectum (Rec) [3].

collected by the Australian Institute of Health and Welfare (AIHW) and published through the 2014 Australian Cancer Incidence and Mortality (ACIM) workbooks [7]. The incidence and mortality rate of prostate cancer from 1982 to 2011 are plotted in Figure 2.3. In Australia, 19821 new cases of prostate cancer were diagnosed in 2010 and 3294 new deaths caused by prostate cancer in 2011, while the risk of diagnosis is 20.8% and the risk of death is 4% for males below the age of 85. Prostate cancer is responsible for 13.4% of all male deaths from cancer. According to AIHW's statistics, prostate cancer has the highest diagnosis rate of any cancers amongst the male population in Australia, being detected at more than twice of the rate of bowel cancer, which is the second-most frequently diagnosed cancer in men[7].

2.1.3 Factors Affecting the Risk of Prostate Cancer

Several well-known factors significantly increase the risk of developing prostate cancer, of which age is the most pronounced. The diagnosis of prostate cancer is very rare for

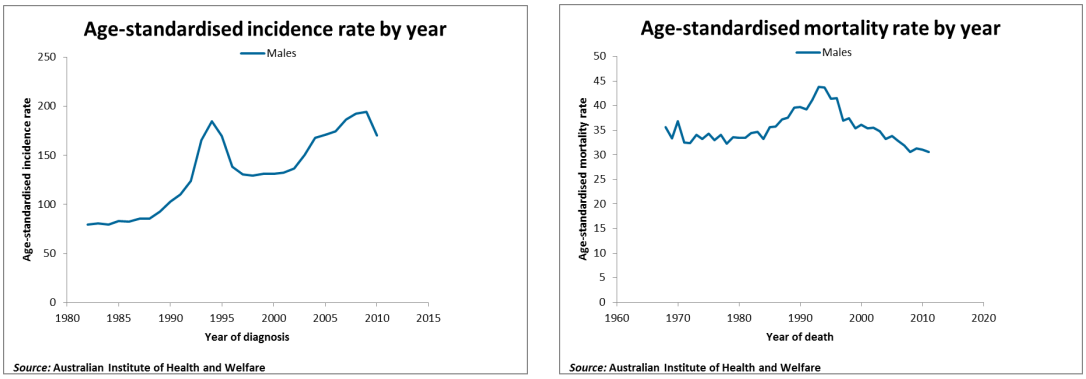

(a) Incidence rate of prostate cancer in Australia

(b) Mortality rate of prostate cancer in Australia

Figure 2.3: Incidence and mortality rate (per 100000 males) of prostate cancer in Australia published in ACIM 2014, which is standardised to the Australian 2001 standard population.[7]

men under the age of 40. However, diagnosis rates increase rapidly beyond 50 years and reach a maximum at around the age of 70 [7, 8].

Another important factor related to the risk of developing prostate cancer is genetics. A man has a higher incidence risk of prostate cancer if his genetic relatives have been diagnosed with prostate cancer. Studies also indicate that this increased risk depends on the how many family members have been diagnosed and the proximity of their relationship [9, 10]. One possible effect of genetic factors on the development of prostate cancer is through variations in sensitivity to androgens via androgen receptor genes. The effect of androgens such as testosterone seems to be an essential condition for the development of prostate cancer, since no case of prostate cancer is known in animals or humans who have been spayed before sexual maturation [11].

The incidence of prostate cancer amongst different human populations is known to vary significantly [12]. According to the global cancer statistics published in 2011, Australia has the highest incidence of prostate cancer in the world. However, the incidence rates in many Asian countries are less than one tenth of this value [13]. This effect is likely be a combination of different factors, including the genetic predisposition

of different ethnic groups, environment, lifestyle habits and diet. A higher incidence of prostate cancer is observed amongst Asian emigrants living in Western countries compared to their former compatriots, indicating that environmental, dietary or lifestyle factors are significant contributory factors [14].

Besides age, genetics and location, other factors such as obesity and exposure to sunlight appear to be involved in the development of prostate cancer. The relation between obesity and the risk of prostate cancer is still obscure; although no significant and constant association between obesity and the risk of low grade prostate cancer has been found to date, a positive relation between obesity and high grade prostate cancer has been observed in several studies [15, 16]. Although sunlight is usually associated with an increased risk of skin cancer, studies indicate that exposure to sunlight leads to a reduction of incidence of prostate cancer and certain other cancers [17, 18]. This may be associated with exposure to the ultraviolet radiation [19, 20] or its influence on the production of vitamin D [21, 22, 23].

2.1.4 Symptoms and Diagnosis of Prostate Cancer

Most prostate tumours are slow growing, often with no significant symptoms detectable for less developed tumours. Due to the anatomical location and function of the prostate, the symptoms of later stage prostate cancer are mostly related to the urinary system symptoms, such as difficulty in starting or stopping the flow of urine, high frequency of urination, weak or discontinuous flow of urine, or pain during urination. Prostate cancer can also lead to erectile dysfunction, blood in the urine or semen and frequent pain in the lower back hips, or upper thighs [24]

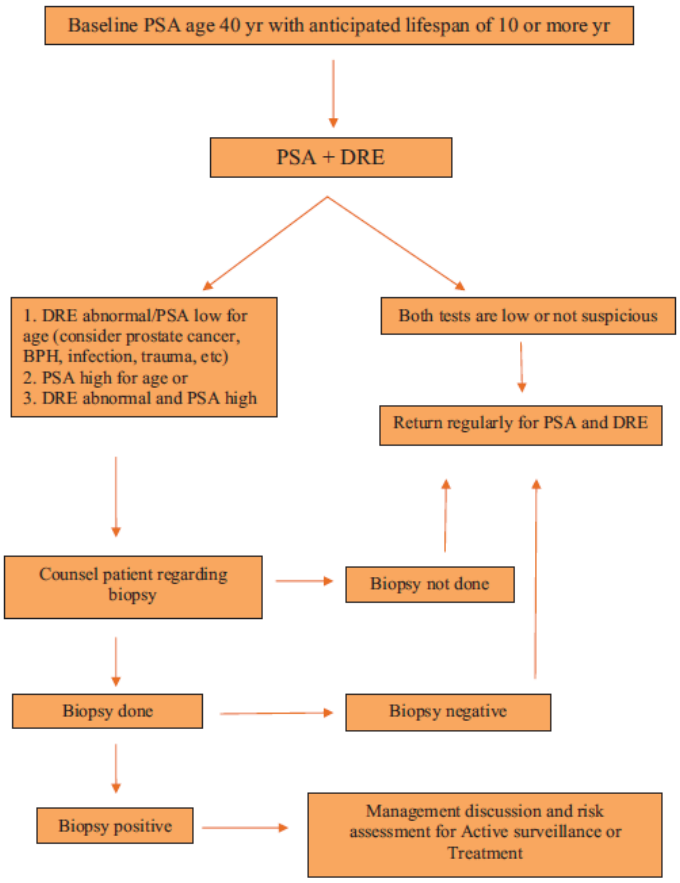

Figure 2.4: Strategy for diagnosis of prostate cancer suggested by American Urological Association guideline [25].

2.1.5 Diagnosis of Prostate Cancer

The symptoms of early stage prostate cancer are not necessarily clear or specific, with the result that many prostate cancers are not detected until the disease has significantly progressed. Figure 2.4 illustrates the recommended procedure for definitive prostate cancer diagnosis [25].

A number of biochemical markers associated with prostate cancer can be detected in the blood. One of the earliest to be clinically applied was prostate acid phosphatase (PAP), which was first isolated in men's ejaculate in 1935 [26]. High levels of PAP in serum indicate the probable presence of prostate cancer. However the application of PAP is limited due to its fast deactivation at room temperature and the fact that it can easily become contaminated by platelets and leukocytes [27]. In addition, PAP level is unable to identify localised prostate cancer as less than 20% of patients with localised prostate cancer exhibit abnormal PAP levels [28, 29].

The marker which is most commonly used to diagnose prostate cancer today is the prostate specific antigen (PSA). PSA is a serine protease which is predominantly secreted in the prostate. It was first identified in 1971 and detected in the serum of patients with prostate cancer in 1980. Usually, the PSA level is determined through a blood test; the level of PSA in serum for a normal man is generally less than 4 ng/ml [30]. Presence of prostate cancer leads to the progressive destruction of the prostate. which results in progressively higher levels of PSA released into circulation [31, 32]. Therefore, an abnormally high PSA level (in particular, where there is a sudden increase in PSA level for a given patient) is a likely indicator of the presence of prostate cancer. The association between PSA and the existence of prostate cancer is not absolute, and there are many instances where the PSA tests of men without prostate cancer gave positive results, and conversely, where patients with prostate cancer exhibited a normal level of PSA [33, 34, 35]. This might due to that other factors besides

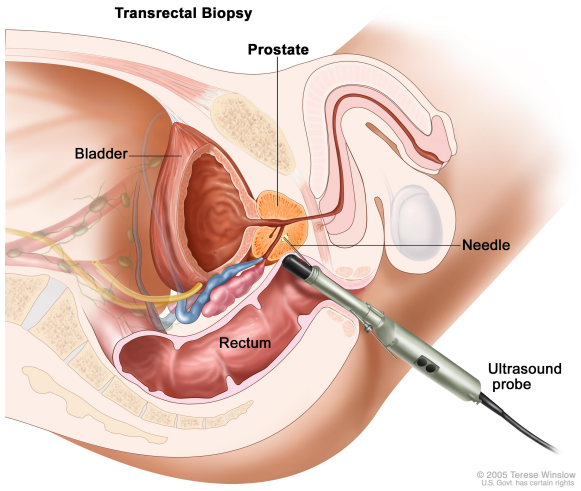

Figure 2.5: Diagram illustrating ultrasound guided prostate biopsy [40]

the presence of prostate cancer can also affect the serum PSA level, such as benign prostate enlargement, sexual activity and infection in the prostate [36]. Thus, instead of being used as a monoindicator of prostate cancer, PSA is usually combined with a digital rectal examination (DRE), and followed up by more invasive tests (including biopsy) if there is a positive indication for cancer [37, 38].

DRE is a procedure performed to examine the physical status of prostate. During DRE, a gloved finger is inserted into the rectum of the patient to check for any palpable abnormality of the prostate by pressing and rubbing the prostate through the rectum wall. Since DRE depends on the tactile impression of the prostate from within the rectum, its efficacy in detecting tumours which are small or located to the posterior of the prostate is poor [39]. Consequently, as with PSA, DRE alone cannot provide a definitive diagnosis of prostate cancer.

The recommended course of action for patients with abnormal results for PSA and/or DRE is to undergo a needle prostate biopsy. Prostate biopsy refers to a microscopical examination of small tissue samples taken from different parts of prostate by ultra-fine biopsy needles. The needles can be inserted through rectum, urethra or perineum, of which transrectal method is the most common. Transrectal needle

insertion is usually guided by real-time transrectal ultrasound (TRUS) imaging [41]. A biopsy needle is mounted on the TRUS probe and guided to the desired insertion position (Figure2.5). Typically, 12 cylindrical tissue samples, the majority from the base and the apex of the peripheral prostate, are sampled for the further microscopical examination [42, 41]. Provided that at least one needle intersects a cancerous region of the prostate, a biopsy provides both a definitive diagnosis of prostate cancer and an evaluation of its aggressiveness.

2.1.6 Prostate Cancer Classification

Like all cancers, prostate cancer can be categorised based its severity (grading) and level of spreading (staging). Grading measures the degree of cell abnormality, which is correlated with the aggressiveness of the cancer, while staging measures the degree of disease progression.

To grade the severity of prostate cancer, Donald Gleason and his colleagues developed a histological grading system, based on clinical trials from 1960 to 1975. In the early version of Gleason grading system, it defined nine histological patterns based on the unique appearance of prostate cancer. These patterns are then integrated into five grades according to the associations between the pattens and their biologic phenotypes [43, 44]. The five Gleason patterns are shown in Figure 2.6.

By comparing the appearance of prostate biopsy samples under a microscope with the Gleason pattens, the samples are given a Gleason score, indicating the grade of the cancer. As mentioned in Section 2.1.5, usually, 12 samples are removed from prostate for biopsy. However, the Gleason scores of these samples may not necessarily be the same; the mortality rate for patients with prostate cancer exhibiting a range of Gleason scores - for example, in the range a to b - is higher than for patients whose prostate cancer has a uniform Gleason score of a and lower than for patients with prostate

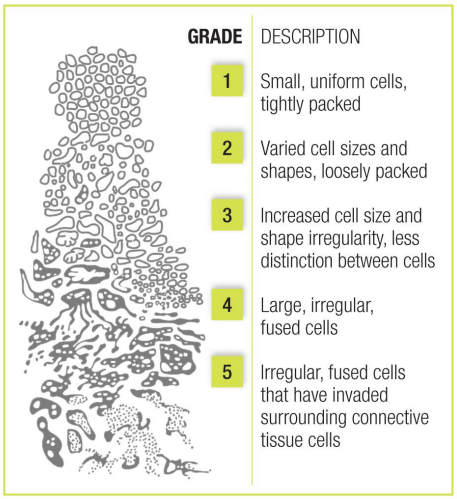

Figure 2.6: Gleason pattens of prostate cancer cells and a brief description for each grade.

cancers exhibiting uniform Gleason scores of b. To provide an overall indicator of the severity of a particular prostate cancer, Gleason and his colleagues suggested to use the sum of the Gleason scores of the two most dominant patterns among all the samples from a prostate biopsy as the total Gleason score of a cancer Gleason1992. This calculation of the total Gleason score was changed following the 2005 International Society of Urological Pathology (ISUP) consensus conference on Gleason grading of prostatic carcinoma. The new calculation uses the sum of the Gleason score of the most dominant pattern and the highest Gleason score as the total Gleason score of prostate cancer whose biopsy samples have three or more Gleason scores [45]. Since the total Gleason score is always the sum of two Gleason scores, it is in a range from 2 to 10. A prognosis can be vaguely made according to total Gleason score. Patients with prostate cancer of total Gleason score higher than 7 may die in a short period of time while patients with prostate cancer with a total Gleason score less than 7 may not exhibit any symptoms at all [46].

The most popular method for staging prostate cancer is *TNM* system, introduced by the International Union Against Cancer in 1974 [48]. This systems classifies the

Table 2.1: Stages of prostate cancer defined in the TNM system [47]

T	TX	Primary tumour cannot be assessed	
	T0	No evidence of primary tumour	
	T1	Clinically inapparent tumour not palpable or visible by imaging	
		T1a	Tumour incidental histological finding in $\leq 5\%$ of tissue resected
		T1b	Tumour incidental histological finding in $> 5\%$ of tissue resected
		T1c	Tumour identified by needle biopsy (because of elevated prostate specific antigen [PSA] level)
	T2	Tumour confined within prostate; tumours found in 1 or both lobes by needle biopsy but not palpable or reliably visible by imaging	
		T2a	Tumour involves one-half of 1 lobe or less
		T2b	Tumour involves more than one-half of 1 lobe but not both lobes
		T2c	Tumour involves both lobes
	T3	Tumour extends through the prostatic capsule; invasion into the prostatic apex, or the prostatic capsule is classified not as T3 but as T2	
		T3a	Extracapsular extension (unilateral or bilateral)
		T3b	Tumour invading seminal vesicle(s)
	T4	Tumour fixed or invades adjacent structures other than seminal vesicles (eg, bladder, levator muscles, and/or pelvic wall)	
N	NX	Regional lymph nodes were not assessed	
	N0	No regional lymph node metastasis	
	N1	Metastasis in regional lymph node(s)	
	M0	No distant metastasis	
	M1	Distant metastasis	
		M1a	Nonregional lymph nodes(s)
		M1b	Bone(s)
		M1c	Other site(s) with or without bone disease

stage of tumour progression using three measurable disease parameters: the status of primary tumour (T), the involvement of regional lymph nodes (N) and the situation of distant metastasis (M). The most important aspect is T, which is divided into 4 stages for the presenting tumour (T1-T4) and two additional stages - TX (which refers to the situation where the primary tumour is not accessible and therefore not assessable) and T0 (which refers to the case where there is no evidence of a primary tumour). The stages T1-T4 are further divided into different subcategories. Table 2.1.6 shows each of the stages defined by the TNM system [47, 48]. By combining the result of TNM staging with patient's Gleason score, the prostate cancer can be grouped into one of four overall stages, as showin in Table 2.2, where G refers to the total Gleason score [49]:

- **GX**: Gleason score is not accessible
- **G1**: Gleason score 2-4, Trifling anaplasia
- **G2**: Gleason score 5-6, Medium anaplasia
- **G3-4**: Gleason score 7-10, Conspicuous anaplasia

These four stage groups give an indication of the likely progression of the disease. Patients with Stage I cancers have the lowest 5, 10 and 15 year mortality rate, while patients with Stage IV cancers have the highest mortality rate. This has been quantitatively demonstrated via randomised trials of 1500 patients investigated by the Radiation Therapy Oncology Group [50].

Table 2.2: American Joint Committee on Cancer (AJCC) Stage grouping [49]

Stage	**T**	**N**	**M**	**G**
Stage I	T1a	N0	M0	G1
Stage II	T1a	N0	M0	G2-4
	T1b-c	N0	M0	Any G
	T2	N0	M0	Any G
Stage III	T3	N0	M0	Any G
Stage IV	T4	N0	M0	Any G
	Any T	N1	M0	Any G
	Any T	Any N	M1	Any G

2.2 Prostate Cancer Treatment

2.2.1 Surgical Treatment

Currently, the most common treatment option for localised prostate cancer is *radical prostatectomy*, which refers to the surgical resection of the entire prostate [51]. During the operation, one or more incisions will be made in order to visualise and access the prostate and its surrounding tissues, such as the pelvic lymph nodes, seminal vesicles and bladder. After the excision of the prostate and any other tissues adjacent to the prostate into which the cancer may have diffused, the urethra and bladder are reattached. Urination is usually performed using a catheter for about one week. In addition to the removal of the prostate, the access to the pelvic lymph nodes also provides important information for prostate cancer staging.

Depending on the size and nature of the incision(s) during the operation, radical prostatectomy can be classified either as *open radical prostatectomy* (ORP) or *laparoscopic radical prostatectomy* (LRP). In ORP, an incision from 8 to 10 cm is usually opened in the lower abdomen (*radical retropubic prostatectomy*) or in the perineum (*radical perineal prostatectomy*) for both removal of the prostate and direct visual inspection of the surrounding area [52]. LRP is a less invasive treatment, which is often performed with the assistance of a surgical robot [53]. In LRP, multiple trocars of

5 mm and 10 mm are inserted in the patient to provide visualisation using the laparoscope and to provide physical access to the prostate. The cumulative size of all of these incisions is approximately 5 cm [54, 55]. As the procedure is less invasive, LRP generally results in less blood loss compared to ORP, which reduces the need for blood transfusions and the potential complications that result [56]. Although other benefits might be expected, such as reduced hospitalisation time and reduced post-operative pain, these is currently little evidence showing significant improvement in either these aspects or overall efficacy of the procedure compared to ORP [57, 55].

2.2.2 Hormonal Therapy

Hormonal therapy for prostate cancer focuses on the influence of androgen on prostate cell growth and survival. One condition of the growth and survival of prostate cancer cells is the binding of dihydrotestosterone (DHT) and androgen receptors. In the prostate, DHT is converted from androgen under the presence of 5α-reductase. Thus, the key to eliminating prostate cancer cells is to reduce the level of androgen. The majority of male androgen production occurs in the testes, with smaller amounts produced in the adrenal glands. The process of androgen production starts at the hypothalamus, where the luteinising hormone-releasing hormone (LHRH) is produced. LHRH moves from the hypothalamus into the pituitary gland, where it binds with LHRH receptors to stimulate the release of luteinising hormone (LH). LH then travels to the testis and binds to the LH receptor, which finally causes the synthesisation of androgen (testosterone) from cholesterol in testis. In a negative feedback loop, the level of androgen limits the production of LHRH and hence LH, such that the level of testosterone in the blood remains stable. Therefore, the use of hormonal therapy to treat prostate cancer primarily aims to either reduce the androgen level (androgen ablation), inhibit the binding of the androgen receptor with its ligands in the prostate,

or to combine these approaches [6]. Although studies indicate that hormonal therapy is able to reduce the androgen-responsive growth of prostate cancer cells, it leads to a number of significant side effects depending on the specific hormone used; more importantly, it is not curative due to its inability to prevent the growth of androgen-independent prostate cancer cells, which exist not only in advanced prostate cancer but also in early stage prostate cancer [58, 59, 60, 6].

2.2.3 Radiation Therapy

2.2.3.1 Radiation Induced Cell Death

Radiotherapy aims to control cancer by using ionising radiation to induce cancer cell death through damage to cell DNA. The damage to the DNA molecule caused by ionising radiation results in the destruction of the double helix structure of DNA, either through *direct action* of the radiation on the DNA molecule itself, or *indirect action* on the surrounding medium (mostly water) which results in free radicals that cause chemical damage to the DNA. For particle radiation, the destruction of DNA occurs mainly as a result of direct action, while indirect action dominates in the case of electromagnetic radiation [61, 62].

It is obvious that the higher the energy deposited per unit mass by the applied radiation field (i.e., the higher the absorbed dose), the higher the rate of cancer cell mortality. However, although cancer cells are more susceptible to radiation damage than healthy cells (due to their rapid growth cycle and impaired self-repair mechanisms), healthy tissues are also damaged by exposure to radiation. Therefore, increasing the amount of radiation given to patients will also increase the rate of side effects and complications. These risks are more serious when the cancer occurs deep inside the body or in tissues adjacent to critical or highly radiation-sensitive organs. Therefore, the objective of radiotherapy is to deliver sufficient radiation to kill cancer cells while

limiting the dose received by healthy tissues as much as possible.

The effect of radiation on human tissues is also determined by the mode of delivery - that is, both the dose rate and the distribution of dose over time (temporal fractionation). One reason for this is the ability of cells to repair damage to their own DNA. DNA is composed of two strands of nucleotide molecules twisted together in the well-known double helix structure, and encodes an organism's genetic instructions. The nucleotides are of one of four types - adenine (A), thymine (T), guanine (G), or cytosine (C) - and are bonded across the helix in pairs (A/T or G/C). Damage to one strand of the helix can be repaired (e.g. if the thymine base is damaged, it can be replaced as only thymine can pair with the adenine base opposite). However, the DNA molecule will be completely disrupted and destroyed if both strands are broken, since that base pair is completely lost. Double-strand breaks become increasingly likely for a given radiation type as the dose rate increases.

Based on the origin of the radiation relative to the patient, radiotherapy can be classified into one of two types: external beam radiotherapy (EBRT) or brachytherapy. These will be discussed in detail in the following section.

2.2.3.2 External Beam Radiotherapy

EBRT is the most common and mature radiotherapy technique for cancer treatment. It achieves the desired dose distribution in the target volume by directing an external radiation source to the target. Depending on the type and location of the cancer, the most appropriate radiation source is applied. Electrons and keV photons (under 500 keV) are usually preferred for treatment of skin or superficial cancer [63], while hadron therapy and megavoltage treatment systems have better performance in treating cancer which is relatively deep inside the patients. Although hadron therapy has developed rapidly in the past few years due to its ability to easily select the depth of maximum energy deposition Bragg peak, it is still far less common than photon

therapy due to the very high costs of establishing hadron beam facilities.

Several types of EBRT are suitable for the treatment of prostate cancer, which are distinguished by their approaches to achieve the desired dose distribution. Two-dimensional conformal radiation therapy (2D-CRT) is the most established form of EBRT. It shapes the 2D dose distribution in the prostate by spatially modulating the beam geometry using a set of movable collimating plates (multi-leaf collimator). This results in a beam which conforms to the geometry of the target volume in two dimensions. Although 2D-CRT is a simple technique to plan an implement, it cannot achieve a large contrast between the dose delivered to the target volume and surrounding healthy tissue, since the only control over dose distribution in the depth dimension is the energy, intensity and radiation type of the beam (electrons or X-rays for a normal linear accelerator). This problem is more serious when critical and/or radiation-sensitive organs are adjacent to the target volume, which is the case for prostate cancer.

A more sophisticated approach is three-dimensional conformal radiation therapy (3D-CRT). With the use of modern imaging technology, it is possible to obtain detailed 3-D anatomical information for the target volume and its surroundings. As in 2D-CRT, a dose distribution is constructed which is accurately conformal to the 2-D outline of the target volume from one particular perspective. However, the multi-leaf collimator reshapes the beam as the beam applicator moves around the patient in order to apply radiation from a number of different directions. In this way, the incidental dose to healthy tissues is distributed over a larger volume, reducing the dose received by any one region of non-cancerous tissue, while the tumour volume receives are more uniform dose compared to 2D-CRT.

If the intensity and/or energy of the beam are also computed for each angle of application in 3D-CRT, the peak dose can be made to conform even more precisely

to the shape of the tumour. This is known as intensity modulated radiation therapy (IMRT). The desired dose distribution in the tumour is defined in a treatment planning system, which then optimises beam delivery to achieve this distribution while minimising exposure to sensitive organs and healthy tissues in general. The treatment plan created using this computer-assisted inverse method conforms more precisely to the target geometry compared to traditional 3D-CRT. However, IMRT assumes that the target geometry is time-invariant, while in practice organs are continuously in motion due to respiration and other involuntary movements; the patient may also not be precisely physically registered to exactly the same position as during the pre-irradiation imaging procedure. To reduce the impact of geometry changes between treatment plan and beam delivery, imaging can be performed concurrently with treatment, allowing the treatment plan to be adjusted in real time. This technique is known as image guided radiation therapy (IGRT). A further refinement is to use continuous rather than discrete adjustment of beam orientation, shape and intensity - this is known as volumetric modulated arc therapy (VMAT). IGRT and VMAT are the state of the art in external beam radiation therapy.

At least 70 Gy is required for the treatment of prostate cancer and higher doses at the target area will increase the rate of cancer control [64, 65, 66, 67, 68, 69]. Although the development of modern imaging technology, computer power and treatment planning algorithm significantly has improved the conformity of EBRT, the maximum dose at target region is still limited by the damage in the surrounding healthy tissue caused by the externally applied radiation. This is an intrinsic property of EBRT, since radiation has to pass through and will hence deposit energy in the healthy tissues between between the source of radiation and the target. Thus, the maximum dose that can be delivered to a tumour can be increased by directly placing the radiation source inside the tumour, This is the approach used in brachytherapy.

2.2.3.3 Brachytherapy

Since brachy has a meaning of 'short' in Greek language, brachytherapy treats cancer by either temporarily or permanently placing a radiative source in very close proximity to the tumour. The source may be placed either immediately adjacent to the tumour, as in ocular plaque brachytherapy, or directly inside the tumour volume itself, as in the case of prostate brachytherapy (PBT). The dose received by tissue drops rapidly with increasing distance from the source, such that the dose distribution can be made to closely conform to the tumour geometry. For localised cancer, brachytherapy is able to deliver a higher dose to the tumour with a lower risk of complications compared to EBRT [70, 71, 72, 73, 74, 75]. In addition, brachytherapy can be more cost effective than EBRT for the treatment of prostate cancer [76].

Two brachytherapy modalities, distinguished by the dose rate and duration of implantation, are commonly used for the treatment of prostate cancer: low dose rate (LDR) brachytherapy, in which the initial dose rate is less than 2 Gy/hr, and high dose rate (HDR) brachytherapy, where the dose rate exceeds 12 Gy/hr. In LDR brachytherapy, a short-lived radioisotope such as ^{125}I, ^{103}Pd or ^{131}Cs is encapsulated in a small inert cylinder (typically LDR PBT uses around 100 individual seeds, each about 4-5 mm long) and permanently implanted into the target. The desired dose distribution is programmed into the treatment planning system, and the arrangement of seeds is calculated. Stranded seeds spaced along a dissolvable polymer filament are loaded into in a thin needle, which is then withdrawn leaving the seeds permanently implanted.

More recently, the advantages of HDR PBT have led it to becoming a popular option for the treatment of prostate cancer. In HDR PBT, a single cylindrical radiation source, most commonly ^{192}Ir embedded in a palladium or gold capsule, is attached to the end of a flexible steel cable which is driven by a remote controlled source delivery

system known as an *afterloader*. A series of catheters are inserted into the prostate and attached to the afterloader, which sequentially inserts the HDR source into each catheter in turn and translates it through a series of pre-planned positions, with a dwell time of a few seconds in each position. The desired dose distribution is achieved via the choice of source positions and the dwell times in each position. At the end of the treatment, the HDR source is retracted into the shielded chamber of the afterloader. Efficacy of treatment of prostate cancer with HDR PBT has been compared to IMRT by Fatyga et al. in 2009; HDR PBT was shown to be offer significantly better outcomes in terms of minimising dose in the bladder and rectum, and its ability to control the tumour [72]. Hermesse et al. conducted a similar study, also in 2009, comparing the dose specificity which is achievable with HDR PBT with IMRT and helical tomotherapy for the treatment of prostate cancer [73]. Again, the conformity of the high dose region to the geometry of the prostate was shown to be the best for HDR PBT, which also offered the lowest incidental dose to other tissues.

In this Thesis, the focus is on instrumentation for HDR PBT quality assurance. An equivalent design optimised for LDR-PBT has also been developed as the subject of a separate project; therefore, LDR-PBT will not be discussed further in this Thesis.

The next section discusses the problem of the errors which may exist between the desired and actual position of the HDR brachytherapy source during HDR PBT treatment.

2.3 Errors in Source Placement in HDR Prostate Brachytherapy

Maximising the efficacy of cancer treatment and minimising the damage to healthy tissues both require that the actual positioning of the radioactive source relative to

the prostate conforms as closely as possible to the position specified by the treatment plan during the treatment process. Positioning uncertainty in HDR PBT has been investigated extensively in the literature. In 2014, Kirisits et al. performed a comprehensive review of the causes of positioning errors based on the HDR-PBT guidelines published by the American Association of Physicists in Medicine (AAPM) and GEC-ESTRO [77]. The sources of positioning uncertainty in HDR PBT were found to include uncertainty in source strength, intrinsic limitations of (and human error in) operating treatment planning systems, difficult-to-model heterogeneity effects, imaging limitations (signal-to-noise, contrast and resolution), source delivery uncertainty and patient-related uncertainties such as physiological changes which occur during the procedure or between pre-treatment imaging and the start of the procedure itself. The objective of the *HDR BrachyView* system presented in this Thesis is to monitor source misplacement resulting from either the error in source delivery within the catheter (due to the limits of mechanical precision of the afterloader) or the displacement of the catheter relative to the prostate and surrounding critical organs between planning and treatment.

According to published manufacturer specifications, commercially available afterloaders can achieve source positioning to within ± 1 mm of the desired position (with a confidence interval of 95%) [78, 79]. This positioning uncertainty has also been confirmed independently in measurements of source placement in straight catheters, performed at different institutions [80, 81]. In the case of curved applicators, the precision of source positioning is significantly worse - with an error as large as -5 mm depending on the curvature of the catheter [82, 83, 84, 85, 86, 87]. The negative-depth positioning error in source placement in a bending catheter occurs because the diameter of the catheter is usually larger than that of the source and its driving wire. When the source is driven into a curved catheter, the source is pushed toward the

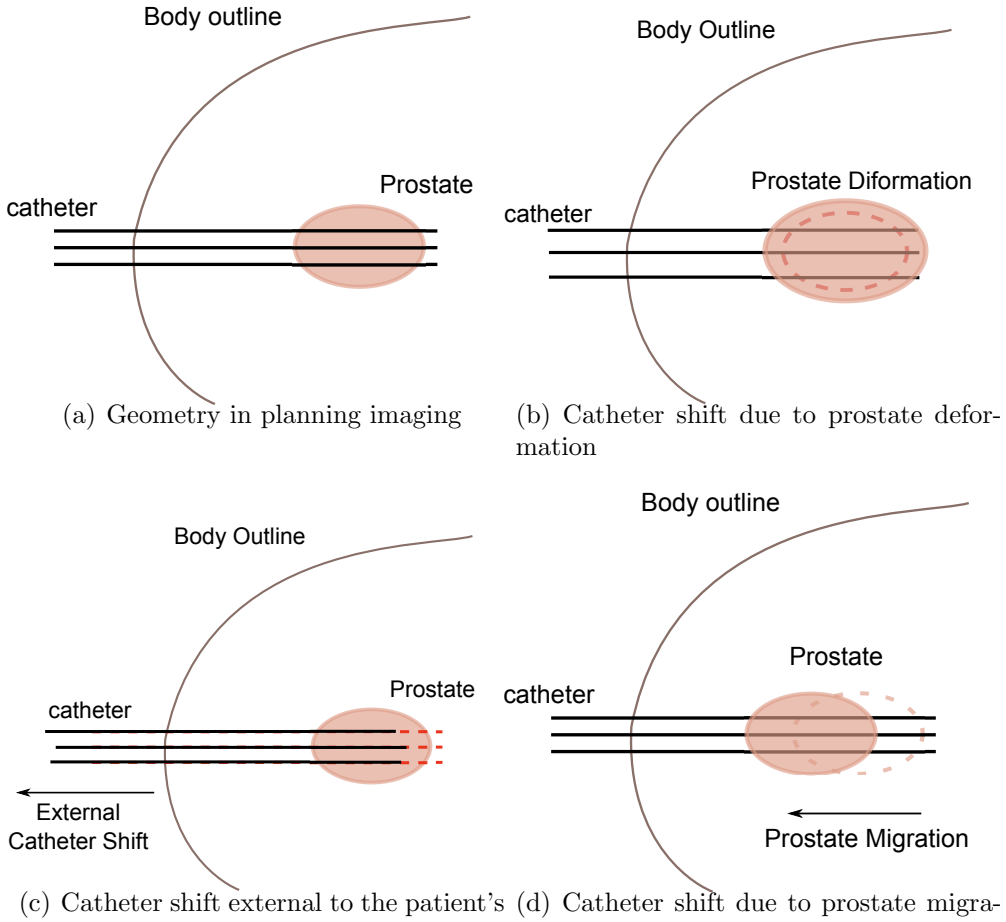

(a) Geometry in planning imaging

(b) Catheter shift due to prostate deformation

(c) Catheter shift external to the patient's body

(d) Catheter shift due to prostate migration in the patient's body

Figure 2.7: Causes of catheter position shift relative to the prostate.

catheter wall, which is away from the central axis of the catheter. In this case, the real source path is longer than the nominal path along the axis of the catheter, leads to an inadequate source depth inside the catheter compared to the depth required by the treatment planning system [88].

While the precision of the afterloader mainly depends on its mechanical design (gear backlash, stepper motor resolution and reduction ratios etc.), changes in the geometry of the catheter and prostate can be classified into three types: deformation of the prostate, the shift in catheter position external to the patient's body, and prostate migration relative to the body outline (Figure 2.7) in [89, 90].

Prostate deformation due to the oedema of the prostate and its surrounding tissue after a HDR brachytherapy fraction was studied in a number of publications [91, 92, 93, 94, 95, 96]. Maritinez et al. reported that significant prostate volume change (with mean volume increasing from 30.0 cc to 37.0 cc) only occurred between the first two fractions out of a total of four treatment fractions based on a study of 41 patients [91]. Kim et al. compared the prostate volume between two fractions in treatment delivered to 13 patients, which were separated by approximately 20 hours. In their study, prostate enlargements were observed with a range from 2% to 17% in 5 patients, while volume reductions were observed in 8 patients with a range from 2%-13% [93]. The prostate volume change was also evaluated by Cury et al. CT scans were performed for 31 patients 7 days after a single-fraction HDR brachytherapy, which were used to compare with the planning CT for these patients. 32% of the measurements shows a decrease of prostate volume up to 14.2%, while 68% demonstrated an increase in prostate volume of up to 23.8% [94]. Dinkla et al. investigated prostate volume changes during pulsed-dose rate brachytherapy by analysing catheter configurations in two CT scans conducted 24 and 48 hours after the planning CT scan. Prostate volume variations from -9.3% to +15.6% were observed after 24 hours, and a similar range (-7.5% to 16.3%) was observed at 48 hours [96]. As demonstrated above, significant variation, both positive and negative, in the prostate volume was observed following a HDR BT fraction. The observed patient-to-patient variations are likely due to a combination of the diversity of both patients and their cancers, although there is also some uncertainty in image-based volume estimates themselves. Despite these observed variations in prostate volume, it generally appears to be assumed in the literature that for most patients, the overall impact of the prostate deformation on dose distribution within the prostate volume is insignificant. However, the large variation in prostate volumes observed in some patients indicates that, at least in some cases, better dose

conformity to the desired treatment volume will be achieved if real-time feedback for source position and/or spatial dosimetry can be combined with real-time imaging of the prostate during treatment. This is an important requirement for quality assurance (QA) in HDR prostate brachytherapy.

Correct positioning of the external applicator with respect to the prostate is also a potential source of errors in source placement. Currently, the most common applicator fixation technology is based on an out-of-body template which is sutured to the skin of the perineum prior to implantation. During the implantation, the catheters are affixed to the template in order to prevent catheter displacement external to the body. Numerous studies on catheter movement occurring in the interval between catheter implantation and the administration of treatment fractions has been performed. Significant catheter displacement resulting from improper placement of the catheters relative to applicator template external to the body are quite rare due to the high reliability of fixation methods currently used [90]. However, significant catheter displacements relative to the interior of the body - measured as displacement either from bony markers or implanted gold markers have been reported. Inter-fraction catheter displacement of up to several centimetres have been reported by many authors [97, 91, 89, 98, 99, 90, 100, 95]. Mullokandov and Gejerman studied the shift between the catheter, the template and anatomical bony markers by analysing CT scans of 50 patients. No measurable displacement of the catheter relative to the template is observed; however, a shift between the catheter and ischial tuberosity (a bony marker on the lower pelvis) was observed in the range of 2 mm to 10 mm, depends on the interval between measurements [98]. A CT scan study on applicator displacement between two fractions of HDR BT performed by Hoskin et al. in 2003 reported a mean inter-fraction catheter shift of 11.5 mm in the direction away from the bladder [89]. The same group published a more comprehensive investigation on inter-fraction catheter shift through

a series of treatments comprising three fractions. A mean catheter displacement of 7.9 mm (with the full range from 0 mm to 21 mm) was observed between the first and second fraction, while a mean shift of 3.9 mm (with the full range from 0 mm to 25.5 mm) was observed between the first and third fraction. Among all the catheter displacements observed in this study, 70% of displacements were found to exceed 5 mm for the second fraction and 35% exceeded 5 mm for the third fraction [90]. Similarly, a median catheter shift of 7.5 mm between the planneding CT scan and treatment was observed by Whitaker et al. from study of 48 implants in 25 patients. 67% of such measured implants had offsets exceeding 5 mm [100]. In addition, the relationship between the applicator displacement and the interval after implantation was investigated in most of these studies. Although the time for the catheter displacement to reach its maximum varies from 10 hours to 20 hours, catheter displacement consistently ceased to increase beyond approximately 20 hours in all of these studies [90].

A possible reason for the catheter displacements observed in the previously-discussed studies is prostate migration, which could be caused either by the oedema of tissue between the prostate and the point of catheter insertion (peri-prostatic oedema), or sudden increases in intra-abdominal pressure caused by patient coughing and/or vomiting [89, 90]. In addition, the oedema of prostate itself can push the catheter away from the prostate base [90]. The easiest approach to correct the applicator displacement is replanning the source positions in each catheter with a shift corresponding to the displacement of such catheter. However, this correction is only feasible when the catheter still penetrates the whole prostate at the time of correction. If the catheter has shifted away from the base of the prostate, physical re-advancement of the catheter must be performed [89, 90]. Thus, Hoskin et al. recommended to implant the catheter further than necessary and perform a CT scan before each fraction to correct the catheter shift by simply redefining source to catheter tip distance [89]. This recommendation

assumes that the catheter has only been linearly displaced and is not deflected into a curved shape.

Even when inter-fraction catheter motion is compensated for by adjusting the catheter with imaging guidance prior to each fraction, the displacement of the catheter after adjustment remains significant. A mean catheter displacement of 3.5 mm (with a maximum of 13 mm) following adjustment was observed by Kovalchuk et al. through multi-fraction HDR PBT for 26 patients. The impact of such displacement on dosimetry is then investigated by comparing the results from applying the original treatment plan to the adjusted catheter positions. A prostate $V_{100\%} < 95\%$ was obtained in 46% of the cases, which represents a significant under-dosing of the target volume for many patients [95].

In addition to the factors of afterloader positioning uncertainty and applicator displacement, equipment malfunctions (e.g. undetected afterloader failure) and the inevitable human errors which occasionally occur during the treatment planning, patient transfer and the treatment could also lead to significant source movement errors, both in terms of positioning and dwell time. A series of accidents in HDR PBT were reported by the International Atomic Energy Agency (IAEA) in 2000. The factors contributing to these accidents were also analysed [101]; although the incidence of equipment failure was significantly reduced by the progressive improvements in afterloader systems and their associated QA, it remains non-zero with the possibility of equipment failures unlikely to ever be completely eliminated. In addition, current QA methods are insufficient to detect all errors *in real time* in source placement during the source delivery, especially those resulting from human error. Thus, real-time source tracking during each fraction is crucial to improve the quality of HDR PBT treatment.

2.4 Quality Assurance Methods in HDR Prostate Brachytherapy

As discussed in Section 2.2.3.3, the principal advantage of brachytherapy is the highly conformal dose distribution which it provides within the target volume. This is due to the steep dose gradients provided by the source (or sources, for LDR brachytherapy) inside the target. However, the steep gradients of the brachytherapy source is a double-edged sword, since if it is incorrectly positioned, the high activity can result in significant overdoses being delivered to surrounding critical organs; equally, it will reduce the effectiveness of treatment since cancerous regions may be underdosed. Therefore, reliable and accurate source monitoring is an essential aspect of HDR PBT quality assurance (QA), and can be performed either by measuring the 3D radiation field or by monitoring the source position in three dimensions. This potentially allows real-time adjustments to be made to the treatment plan during treatment.

In the following parts of this section, after a general introduction to existing methods used for QA in HDR PBT, the methods applied in for general quality assurance of the equipment (e.g. calibration procedures) are discussed, followed by various approaches which have been proposed for QA during a specific HDR PBT procedure. This section particularly examines methods used for intra-operation real-time source tracking due to the correlation with the objectives of the *HDR BrachyView* system presented in this Thesis.

A considerable body of work exists on the subject of QA methods for HDR PBT. These methods either provide dosimetric information or track the source in terms of its position and dwell time. Clinically, information regarding dose distribution can be obtained using dosimeters such as ionisation chambers, gel dosimeters, thermoluminescent detectors (TLDs), radiochromic films, semiconductor detectors/dosimeters

such as metal oxide semiconductor field effect transistor (MOSFET) based detectors, scintillation detectors and so on [102].

A number of methods can be applied to obtain an independent estimate of the source position in HDR BT. If the source tracking system is dosimetry-based, the 3D source position is usually estimated using trilateration. After careful calibrations, the radial source-to-detector distance (SDD) can be estimated based on its correspondence with dose measurements normalised to the strength of source. Each dosimeter provides an estimated distance from the source, inscribing a spherical shell of potential source positions around the dosimeter. With two dosimeters, the source can be localised to the circle of intersection between the two spheres, and with three or more dosimeters, the source position can be unambiguously resolved to a single point. Thus, 3D dimensional source position can be uniquely determined using dose measurements from at least three calibrated dosimeters [103, 104]. No collimator is required for this method, however the relationship between distance and dose rate depend on the attenuating medium between source and detector, limiting the achievable accuracy. External-beam computed tomography (CT) imaging could be used to image the source in three dimensions, but would result in a substantial additional radiation dose to the patient, with the resolution limited to a few millimetres. More problematically, imaging would need to be repeated at each source position, which is not feasible due to the short source dwell times used in HDR PBT.

Alternatively, by using a collimator, it is possible to limit the acceptance angle of the detector/dosimeter, and thereby obtain direction source information from the shape of the projections through the collimator. This could be performed tomographically - essentially a form of single photon emission computed tomography (SPECT). However, the exposure time required to obtain a high quality image outside of the body would exceed the source dwell time at any particular point. Reducing the dis-

tance between the source and imaging system by locating it in the patient's body will reduce this problem by several orders of magnitude; therefore, this is the approach which is adopted in this Thesis.

2.4.1 General QA Methods for HDR Prostate Brachytherapy

General QA processes required for HDR PBT aim to ensure that all elements of the system are operating within tolerance limits. The QA process follows a well-defined program, which detailed the commissioning measurements and the frequency with which they need to be repeated. Practical guidelines and recommendations for HDR PBT systems have been published by a number of different institutes [105, 106, 107, 108, 109]. According to these recommendations, besides the regular testing of basic functionality, the main tasks of routine QA procedures include source calibration and source delivery accuracy tests. The methods either proposed or applied to accomplish such tasks are reviewed in this section.

Although the source strength is calibrated by the vendor prior to delivery, the uncertainties corresponding to the source strength calibration values from vendors are significant. Therefore, methods of independent source strength measurement are required [110, 111]. The ionisation chamber is one of the most common dosimeters used for source calibration. It detects radiation by collecting charges created by the interaction of radiation with the gas contained in the chamber. Because of its stable response to a wide range of energies and excellent reproducibility, the ionisation chamber is considered the gold standard for accurate clinical dose measurement. Ionisation chambers have been used to calibrate ^{192}Ir HDR sources since 1980 [112]. Well-type ionisation chambers were further studied for source calibration by Goetsch et al. in the early 1990s [113, 114]. Reynaert et al. directly calibrate an ^{192}Ir source in water with an ionisation chamber. Their measurements demonstrate an uncertainty within

1% of the result from the reference air-kerma rate calibration method [115]. DeWerd et al. designed an insert based on the calibration well chamber introduced by Goetsch et al. to achieve QA for the afterloader in terms of source position and dwell time [114, 116]. In their system, the positional and temporal information for the source was obtained using a lead collimator insert with an acrylic spacer. The whole measurement takes approximately 5 minutes. Source position error of less than 0.4 mm within the catheter and timing uncertainty of less than 1.5% was reported by the authors [116]. The accuracy of source position determination was further improved to 0.2 mm by Li et al. who developed a technique for tracking the source using a trilateration method with a rotating double disk phantom, which is able to accurately control the position of catheter and ionisation chambers [103]. Although precise measurement of source position is achievable by some of above methods, the information observable is limited to a single dimension (depth, i.e. parallel to the axis of the catheter). In addition, the dependence of these methods on predefined catheter and detector positions makes these methods only feasible for the routine testing of afterloader delivery precision.

While source strength is usually calibrated using an ionisation chamber, another important task of QA for HDR PBT is evaluating the dose distribution of the source, which is usually described by the radial dose functions, dose rate constant and anisotropy functions. Although this task is also theoretically achievable using an ionisation chamber array or accurately shifting the chambers for scanning measurement, this approach would be prohibitively expensive, time consuming and will result in measurements with very poor spatial resolution. In addition, the large sensitive volume and physical size of ionisation chamber limit its application in dosimetry when the dose distribution has a steep gradient, especially for in-vivo measurements.

TLDs are physically smaller than ionisation chambers, and have no need for either a wire connection or high voltage power supply. These advantages make TLDs a

popular choice for in-vivo dosimetry for the QA of many forms of radiation therapy. However the requirement of the time-consuming post-irradiation annealing process means that TLDs cannot be used for real-time dosimetry; therefore, they are not a realistic choice of dosimeters for use during HDR PBT treatment to validate agreement between the actual and planned dose delivery during treatment. However, TLDs are still useful tools to measure the dose distribution surrounding the HDR source (that is, the anisotropy of the source). Kirov et al. measured the dose rate distribution in two dimensions (transverse-axis and polar) of a current generation ^{192}Ir source using TLDs, and the result of the measurement was used to validate calculations from a Monte-Carlo simulation [117]. An average deviation of 5% was observed between the readout from the TLD and the predictions of the simulation when the sampling position is more than 3 cm from the source. However, larger uncertainties of up to 10% were found in the measurement with distance less than 2 cm from the source, where smaller (and hence higher spatial resolution) TLD chips were used. Similarly, Karaiskos et al. used Monte Carlo simulations compared with experimental TLD measurements to investigate the radial dose function, dose rate constant and anisotropy function of an ^{192}Ir source [118]. Compared to previously published simulation results for an HDR brachytherapy source in an infinitely large water phantom [119], deviations of up to 25% were observed in their investigation of the radial dose function of an HDR brachytherapy source in finite-dimension phantoms (with phantom diameters from 10 to 50 cm). Meigooni et al. evaluated the sensitivity of TLDs at different distances from the source by comparing TLD measurements with an ionisation chamber located at the same distance [120]. The difference between the doses measured by the TLD and ionisation chamber was approximately 8.5%, measured at distances of 1 cm and 10 cm from the source. It is hypothesised that this was caused by the energy-dependence of TLDs, since the spectrum of photons was observed to shift toward lower energies

when the sampling position moved further away from the source.

An alternative method which can be used to obtain a two-dimensional dose distribution measurement at a certain distance from the source is radiochromic film. Radiochromic film is used to measure dose information by measuring changes in optical density before and after irradiation. By calibrating the film in a highly uniform radiation field, absolute dose information can be retrieved from the ratio of the film optical density before and after the irradiation [121, 122]. Duggan et al. used radiochromic films to measure dose distribution in planes parallel to the axis of the HDR source at radial distances from 2 to 6 mm [123]. A line profile of the dose rate was generated from each film exposure by averaging the dose rate measured across a 24.5 mm wide strip centred on the source axis. The results demonstrated a mean deviation of 7.5% from ionisation chamber measurements.

The accuracy of a radiochromic film dosimetry system with a He-Ne laser film scanner in HDR brachytherapy radiation fields was evaluated by Dempsey et al. in 2000 [124]. The uniformity of the optical density of radiochromic film irradiated under a uniform radiation field, as measured by calculating pixel-to-pixel standard deviation, was found to vary from 1% to 5% depending on the total dose. This variation could be further reduced by sampling a cluster of pixels (i.e. averaging out noise resulting from film granularity). Agreement of 1.5%-4% in absolute dose measurements compared to both Monte Carlo simulation predictions and ionisation chamber measurements were demonstrated in this study. Similarly, an uncertainty of 4.12% was observed in measurements of dose above 1 Gy performed using a radiochromic film dosimetry systems designed by Aldelaijan et al. in both a water phantom and the Solid Water™polymer [125]. To evaluate the anisotropy of a HDR PBT source caused by the self-absorption of the source core and asymmetric attenuation of the source capsule, Sharma et al. measured its anisotropy function using radiochromic films in a water

phantom [126]. Dosimetry results agree with previous measurements performed using an ionisation chamber to within 3%, with Monte Carlo simulation results to within 3% and within 5% of measurements performed using TLDs; however, radiochromic film offers superior spatial resolution compared to all of these methods. Beside dosimetry, radiochromic film can also be used as a QA tool to track the source position due to its high spatial resolution imaging capability. In a 1993 study, Evans et al. used radiochromic film to track the source position when it is driven to the most distal distance (the catheter end as determined by the afterloader) [127]. Positioning errors of up to several millimetres from the intended position at the end of the catheter were demonstrated, which is likely to be a combination of catheter flex and the afterloader's intrinsic linear positioning uncertainty. Rickey et al. proposed a rapid QA system to verify afterloader source delivery accuracy using a combination of radiochromic film with co-registered with photodiode detectors. The authors claimed this system is able to accomplish commissioning of an HDR PBT afterloader in about six minutes with a spatial uncertainty of 0.5 mm and a time resolution of 1 ms [128].

Several other dosimetery systems for source calibration or routine testing of afterloader source delivery accuracy have also been described in the literature. Kirov et al. used silicon diode radiation sensors to measure the dose rate along the transverse axis of both an ^{192}Ir and pulsed dose-rate source at distances between 2 and 40 mm from the source [117]. The results agree with the predictions of Monte Carlo simulation to within 0.5% with an uncertainty much smaller than the TLD measurement performed in a similar scenario. Jursinic used diodes to measure the source position in catheters fixed in a designed template to evaluate the source delivery accuracy of the afterloader [129]. Uncertainty of up to 0.3 mm (depending on the type of applicator) in determining source dwell position and 0.3% in determining source dwell time over a 20 s period was described by the author. Austerlitz et al. measured the strength

of an ^{192}Ir source by inserting the source at the end of a sleeve which is located at the centre of a balloon filled with Fricke solution [130]. Therefore, the dose can be estimated by measuring the change in the Fricke solution's optical density before and after irradiation. According to their study, 11.3 ml of Fricke solution is sufficient for the measurement of the radiation from a HDR source at a radial distance of 2.5 cm. It was noted that dose estimates were inaccurate when the thickness of the sleeve is too small; this is because of the very high dose rate immediately adjacent to the source exceeding the linear range of Fricke solution. Finally, a MOSFET detector was used by Zilio et al. to measure the depth dose of ^{192}Ir source [131]. The result show good agreement with Monte Carlo simulations, with a discrepancy less than 5% for most sample points .

2.4.2 Methods for QA during HDR Prostate Brachytherapy Treatment

QA procedures periodically conducted on HDR PBT equipment are not sufficient to guarantee dose distribution conformity with a treatment plan during treatment of a specific patient. The aim of intra-fraction QA for HDR prostate brachytherapy treatment is to address this requirement. The primary cause of discrepancies between planned and delivered dose distributions is the source misplacement, which is caused either by the displacement of the catheter relative to the prostate and its surrounding critical organs, or by malfunction of the afterloader. Since the risk of catheter displacement increases as the time between treatment planning and the delivery of the fraction increases, it is essential that intra-fraction QA methods can provide a result as quickly as possible - ideally, in real time. Therefore, the trend in QA methods has been toward systems which can provide real-time information regarding either dose distribution or source position. Clearly, passive dosimetry methods such as radiochromic

film and TLDs are not capable of provide such information. The obvious candidate technologies are solid-state semiconductor radiation detector systems.

Several alternatives methods for practical real-time QA in HDR PBT have been proposed, mostly based on comparing real time in-vivo dosimetry around critical organs such as the urethra and rectum with the planned dose. Comprehensive review of real time in-vivo dosimetry in HDR brachytherapy with latest development in a field was presented by Kertzscher [132]. However, it is also recognized that widespread implementations are hampered by the lack of available high-accuracy in-vivo dosimetry systems that are straightforward for the clinical staff to use. Metal oxide semiconductor field effect transistor (MOSFET) detectors have been investigated as a tool for real-time in vivo absolute dose measurements in HDR brachytherapy [133, 134]. The angular dependence an dosimetric response of an implantable MOSFET dosimeter to radiation from ^{192}Ir and ^{60}Co sources at a variety of dose rates was studied by Fagerstrom et al. with a Virtual Water™ phantom [133]. The study shows that their MOSFET dosimeter was more sensitive to the lower-energy radiation from ^{192}Ir compared to ^{60}Co, and angular dependence of the MOSFET was insignificant. Qi et al. reported on the key characteristics of a novel MOSFET dosimetry system developed by the Centre for Medical Radiation Physics at the University of Wollongong (MO*Skin* [135]), including energy dependence and angular dependence, when used to measure the radiation field produced by a HDR brachytherapy source [134]. The deviation between the planned dose and the dose values estimated using the MO*Skin* detector were found to be consistently less than 5%. It was recently demonstrated that the combination of MO*Skin* detectors placed on a surface of the rectal TRUS probe used for planing in HDR is reliable real time in-vivo dosimetry system. It allows accurate localization of the MO*Skin* on a rectal wall relative to prostate anatomy, which maintain a reliable comparison of measured dose with planned in real-time, avoiding error

with uncertainty in MO*Skin* position on a rectum wall [136].

Scintillation-based dosimetry/detector systems are an alternative to direct detection of γ-rays in silicon. There are a number of examples of scintillation-based dosimetry systems in the literature, typically consisting of a plastic scintillator coupled to an optical fibre placed in the urethra and rectal wall. A survey of several such devices shows that they can provide an accurate dose measurement, with an angular dependence of less than 2% and a variation in depth dose readings of less than 3% [137, 138, 139, 140]. Archambault et al. have presented and validated a readout system for in-vivo dosimetry based on a charge-coupled device (CCD) with multiple plastic scintillation detector (PSD) arrays that is compatible with clinical rectal balloons [141]. While these methods perform direct dose measurements, they only record the dose received at single or limited number of sample points, and are unable to track the source position in real time.

Cartwright et al. have proposed a dosimetry system in which an array of Brachy-FOD™ detectors are placed within a rectal probe to measure the dose delivered during treatment [139]. The device is capable of measuring dose delivered to different parts of the rectal wall and can track the progression of the source in one dimension (parallel to the needles) with an accuracy of 2 mm; this provides limited information about the absolute position of the source within the prostate. In addition, the assumption of perfect pre-treatment knowledge of catheter position make it unsuitable for intra-operation source tracking, since the catheter position may shift between catheter insertion and the delivery of the fraction [139]. A more complicated QA system which can track source position without requiring explicit knowledge of catheter location has been investigated by Espinoza et al. in 2013 [104]. A phantom combined with a silicon diode array, the *Magic Plate*, was used to determine source position in three dimensions based on the correlation between the measured dose and the distance between

the source and the corresponding diode elements. This method is capable of providing real time pre-treatment QA information, and can calculate the source position in 3D with sub-millimetre accuracy using the radial dose function for a source-to-detector distance (SDD) between 5 mm and 30 mm. It can also accurately provide independent measurements of source dwell and transit time. While this QA method was demonstrated in a phantom currently, its in-vivo application is possible by placing the *Magic Plate* on a patient couch and registering in TRUS data set used for HDR planning .

A small number of methods for intra-fraction tracking of the source position in real time have been proposed in the literature. Systems based on external imaging devices using pinhole or similar collimators have been proposed in these methods; as they take the most directly comparable approach to the methods proposed in this Thesis, they are specifically discussed in the remainder of this Section. It is noted that while several in-body *dosimetric* positioning methods have previously been proposed, none of the existing *imaging-based* source positioning systems are designed for internal use.

Duan et al. have proposed a monitoring system composed of a dual-pinhole collimator (with the pinholes being 0.5 and 1 mm in diameter, respectively) combined with a standard radiographic screen film and an X-ray fluoroscope [142]. During source delivery, real-time source images projected through the pinholes are captured by the fluoroscope to verify the source movement. The source projections at all dwell positions are recorded permanently by the film, which can be used for a post-treatment QA. The source position can be calculated using the two source projections obtained by pinholes separated by 3 cm. The method was validated in an experiment performed using a cubic polystyrene phantom. The source was placed at a depth of 10 cm inside the phantom and the pinhole collimator was located 15 cm away from the source while the distance between the film and the pinhole was fixed at 20 mm. The source was moved through a series of positions separated by 5 mm. An acquisition time of

at least two seconds is required by the system in order to acquire source projections with sufficient contrast for reliable position determination; however, optimal results were obtained for an acquisition time of 8 seconds. The authors claimed the source projections are distinguishable if separated by 1 mm laterally and 5 mm along the axis of the source. However, the peaks in these acquisitions were largely merged since their separation was smaller than the full width at half maximum (FWHM) of each peak, which leads to a shift of the position of the centre of mass of the projection, introducing a source of error to the calculated source position. In their experiment, the accuracy of 3D source tracking is only investigated in case of the film measurement. For the extended acquisition time of 8 seconds, an overall accuracy of better than one millimetre was observed in the reconstructed source position in three dimensions. However, this accuracy is only relevant to the post-treatment source position reconstruction. In addition, the spatial resolution of the pinhole/film system is insufficient to be able to unambiguously and accurately resolve an arbitrary source position. This is because the film is not replaced during a given HDR fraction, with the result that it is possible that projections of the source become merged with previous projections obtained at different depths but within the same pinhole field of view. In this case, as the images are overlaid, the source positions cannot be resolved. Replacing the film periodically during the treatment would be inconvenient and likely to result in additional positioning errors due to the need to move and disconnect/reconnect equipment. Beside the defect of pinhole/film system discussed above, there are several shortcomings which limit its usefulness as an intra-fraction real-time source tracking tool. The minimum acquisition time of this system is 8 s which is too long to accomplish real-time source tracking during the source delivery. The minimum resolvable spacing between source positions of 5 mm is also too large for effective quality assurance, since a minimum positioning step size of 2 mm is achievable by modern HDR brachytherapy afterloaders.

Finally, the proposed method has no intrinsic mechanism to register the calculated source position with internal anatomical markers or the prostate itself; therefore, the accuracy of the position measurements could be significantly affected by patient movement.

Batic et al. proposed a similar real-time source tracking method using source projections collimated by a two-pinhole collimator [143]. Pixelated silicon detectors were used as the image acquisition system in this design, which eliminates the projection overlapping problem observed in Duan's design. A field of view (FoV) of 20 cm diameter is achieved at 40 cm away from the collimator plane, while the silicon detectors were placed 4 cm below the pinholes. Because of the large object-to-pinhole distance, a large pinhole aperture (4 mm in diameter) was chose to improve the detector efficiency. The detector used in this system contains 256 pixels with a size of 1.4 mm$\times$1.4 mm. Experimental results are presented in which a source is moved through the FOV driven by the afterloader. Although the acquisition time is as low as one second, the discrepancy between true and reconstructed source position was an average of 4.9 mm with a maximum error of 12 mm. This could be caused by the oversized pinhole aperture, large source-to-pinhole distance and poor intrinsic spatial resolution of the detector.

A variation of pinhole method for source tracking was proposed by Song et al. [144]. Instead of using source projections through pinholes, they tracked the source position using shadows on a flat panel detector generated by spherical attenuators (4 mm in diameter) placed between the source and the detector. In their study, frame acquisition time of five seconds was used to obtain the shadow images from a 150 kVp Orthovoltage X-ray source. During the experiment, acquisition and storage of images was triggered manually. However, the authors suggested that a real-time source tracking system based on their design is feasible with an improved readout system for the flat panel detector. While there is no information describing the measured absolute

source position presented in the paper, a mean error of -0.7 mm was found in their measurement of relative distance between the two nearby source positions. However, this figure is an average of negative and positive difference. Although the sign of these error may depend on the position of source relative to the spherical attenuators, these informations are not discussed in the article. The mean of the absolute difference between the real source positions and measurements is actually 1.43 mm. Although this method may be feasible in HDR brachytherapy, no experimental results have yet been presented showing the performance of the proposed system with an HDR brachytherapy source, and no further development of the idea appears to have been undertaken since 2009.

2.5 Conclusion

This Chapter summarised the current status of treatment options for prostate cancer, with a particular focus on HDR brachytherapy, which is the subject of the quality assurance system (*HDR BrachyView*) developed in this Thesis. Studies of source misplacement in HDR prostate brachytherapy were discussed, demonstrating the need for a real-time position monitoring system for HDR prostate brachytherapy quality assurance (QA). Existing QA methods which either been applied clinically or proposed in the literature were comprehensively reviewed. Several QA methods comparable to *HDR BrachyView* were discussed in detail. The trade-off between source tracking accuracy and detection efficiency was discussed, demonstrating the difficulty in using external imaging systems for real-time source tracking. The need for an in-body imaging system is clearly identified; the design of such a system, *HDR BrachyView* , is presented in Chapter 3.

Chapter 3

Design of *HDR BrachyView* system

This Chapter describes the design of the *HDR BrachyView* imaging system. The proposed method of source monitoring and the global coordinate system used for co-registration of the calculated source position within the prostate volume is introduced. The overall arrangement of the components in *HDR BrachyView* probe is presented in Section 3.1, followed by a brief introduction of TimePix detector and its associated readout system (Section 3.2). The collimator design is presented in two sections: the choice of collimator material and thickness (Section 3.3), and the pinhole geometry (Section 3.4).

The *HDR BrachyView* system is a transrectal imaging system for intra-fraction real-time source monitoring in the prostate volume during HDR prostate brachytherapy. The probe consists of a multi-pinhole semi-cylindrical tungsten collimator mounted above an array of pixelated silicon detectors. The assembled probe is housed within a disposable, sterile, rigid, medical grade plastic shell.

Once the source enters the field of view (FoV), the radiation emitted from source is collimated via a double-conical pinhole and projected onto the detector array. For

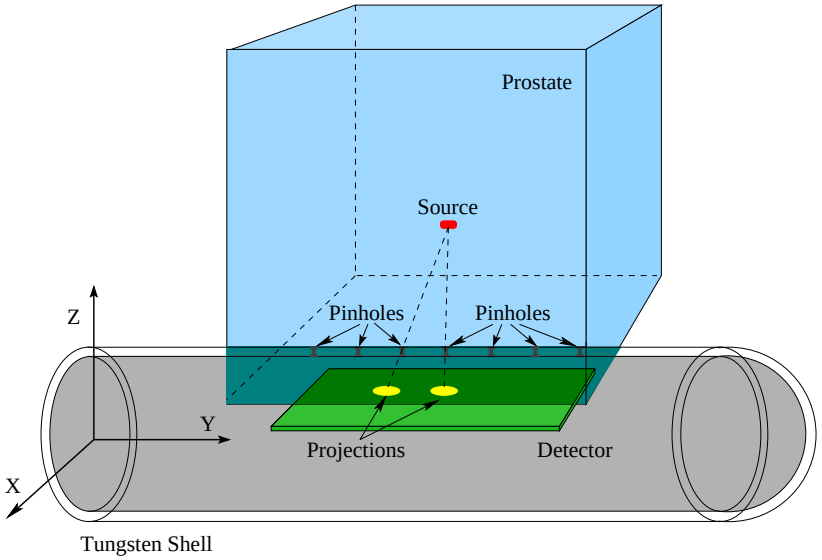

Figure 3.1: Schematic diagram showing the *HDR BrachyView* probe relative to prostate phantom; seven equidistant pinholes are utilised to extend the field of view to cover the whole treatment volume.

every source position, multiple source projections are obtained. The source position in the treatment volume relative to the probe is then calculated by a simple backprojection method that using the centres of mass (CoMs) of the source projections and the centres of their corresponding pinholes (Figure 3.1). Since these back-projected lines do not always perfectly intersect, the best estimate of the source position is defined as the point with the minimum mean squared distance to the set of all back-projected lines.

Since the *BrachyView* probe provides an estimated source position relative to its predefined coordinate system, a common or global coordinate system is needed to establish its relative location within the prostate gland. Therefore, fiducial markers are placed on the surface of the rigid plastic shell, which is inserted in the patient's rectum prior to acquiring the planning CT scan. Once the shell has been inserted, insertion or removal of the probe results in no further tissue displacement.

The acquired CT image is used to determine the relative positioning of the shell to the prostate and the catheters (In case of transrectal ultrasound based treatment

planning, the registration of prostate and the global coordinate system can also be achieved by transrectal ultrasound imaging performed in the rigid plastic shell of *HDR BrachyView* probe). Transrectal ultrasound (TRUS) imaging may be performed through the rigid plastic shell to monitor any anatomical change in the prostate or needle positions that may require intraoperative repositioning immediately prior to treatment and between each fraction. Finally, the TRUS probe is withdrawn and the *BrachyView* probe inserted into its shell to the correct depth by an electromechanical stepper unit prior to the commencement of treatment. TRUS imaging may be repeated between fractions to account for any further anatomical changes in the prostate which may occur during treatment. The ultrasound functionality will be added to the final design of the *BrachyView* probe.

3.1 Arrangement of Collimator and Detector

The schematic of the proposed probe and the coordinate system used throughout this Thesis are shown in Figure 3.1. A transrectal probe with an outer diameter in excess of 25 mm may lead to patient discomfort during and post treatment; therefore, this is set as the absolute maximum diameter of the rigid plastic shell surrounding *HDR BrachyView* , which serves as the ultimate constraint on the dimensions of the collimator and other components of the probe. In particular, the maximum outer diameter of the probe assembly limits the thickness of the collimator, the detector width (along the x axis) and its placement relative to the pinhole centre. The magnification factor of a pinhole camera is defined as the ratio of the object (source) to pinhole distance (h_{sp}) to the distance between the pinhole and the imaging plane (detector) (h_{pd}):

$$MF = \frac{h_{sp}}{h_p d} \tag{3.1}$$

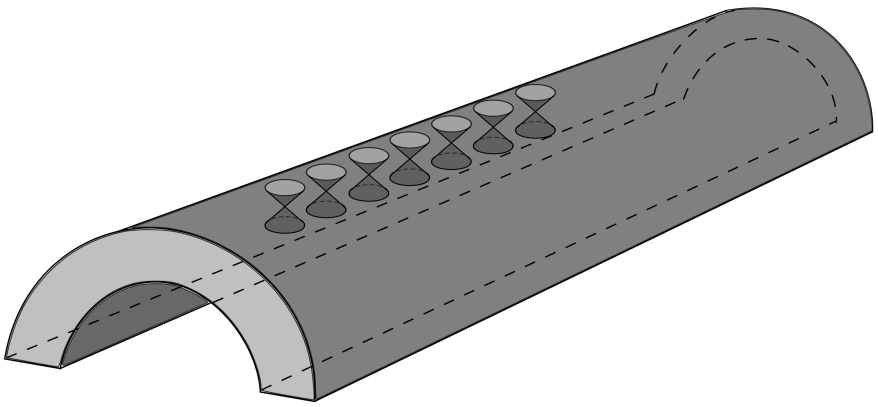

Figure 3.2: Illustration of the collimator

During the HDR treatment, the prostate is enlarged and the source may be placed between 5 mm to 45 mm away from the top surface of the collimator (5 mm $\leq$ $h_{sp} \leq$ 45 mm). The ability to image the source within the entire potential treatment volume is crucial to the success of the proposed QA system; therefore, while the detector array should be positioned as far below the collimator as possible in order to maximise the size of the projections, it must not be placed so far below the pinholes as to artificially limit the field of view to less than the full potential treatment volume.

A three-dimensional drawing of the semi-cylindrical tungsten collimator is shown in Figure 3.2. In order to ensure that at least two projections of the source are visible from all positions within the prostate volume, seven pinholes are uniformly spaced at intervals of 6.5 mm along a straight line parallel to the y axis of the probe. The detector plane is positioned close to the central axis of the probe's outer cylindrical shell, with the sensitive volume of the detector located 8.5 mm below the pinhole centre (i.e. $h_{pd} = 8.5$ mm)). The cross-section of the probe and the collimator are shown in Figure 3.3.

An imaging area of 14 mm$\times$56 mm (256 $\times$ 1024 pixels) is made by seamlessly tiling four Timepix detectors. When combined with the multi-pinhole collimator, the

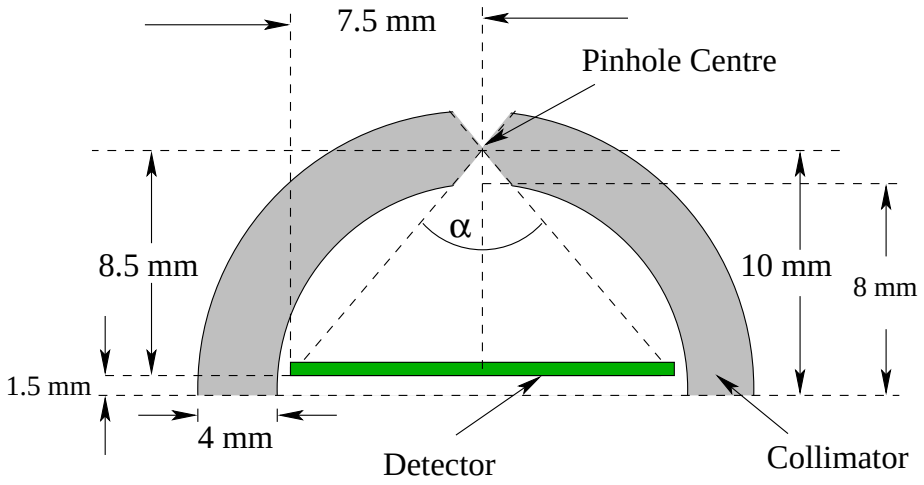

Figure 3.3: Cross section of the probe (top half)

FoV is extended to the full prostate volume in the yz plane. Furthermore, the probe can be rotated around its axis to track the source in the xz plane and ensure that the catheter remains within the FoV. The lower half of the probe houses a passive cooling system. The surrounding rigid shell ensures the probe is capable of rotating smoothly during the treatment and acts as a barrier between the tungsten shell and the rectal wall. The dose enhancement in the vicinity of tissue-tungsten interfaces in HDR brachytherapy will be discussed in detail in the Chapter 5.

3.2 Detector and Data Acquisition System

Two main requirements govern the choice of pixelated solid-state imaging device for *HDR BrachyView* . Firstly, the short source dwell time in HDR prostate brachytherapy requires a photon detection system with a sufficiently fast readout time. Secondly, high detector image resolution is essential, since as the source-to-probe distance (h_{sp}) is increased in the z direction, its projection is *minified* such that the physical movement of the source is scaled to a smaller change in the position of the projection. Therefore, a high-resolution device is needed in order to achieve sufficient accuracy when the

source is located near the extremities of the treatment volume.

The pixelated silicon ASIC *Timepix* is a derivative of the well-known *Medipix2* device. Timepix is a radiation-hardened 256×256 array of single-pixel analog/digital pulse processing cells with a common CMOS digital readout system. The chip is designed to be bump-bonded to a flip-chip pixelated array of 256×256 55 μm×55 μm semiconductor radiation sensors, each of which produces a charge pulse whose amplitude is proportional to the energy of the incident particle or photon. The Timepix chip satisfies both the high resolution and fast readout requirements, and its dimensions are compatible with the constraints of *HDR BrachyView* [145, 146].

The material and thickness of the sensor array is selected based on the application, with silicon wafer thickness of 300 μm available as the standard option. Since the majority of photons emitted from ^{192}Ir are above 100 keV, the signals generated by the detector with silicon sensor are mainly contributed by the incoherent scattering interactions of photons and silicon. Considering that *HDR BrachyView* tracks source positions only using the centre of the source image, its accuracy mainly depends on the symmetry of counts distribution to the projection centre rather than a well defined projection shape. In this case, the requirement of quantum efficiency is low. The standard 300 μm thick silicon sensor is sufficiently sensitive to the energy of photons emitted from HDR PBT sources such as ^{192}Ir (validated by both simulation and experiment results presented in Chapter 6 and 7). Thicker silicon substrates (500 μm or 1 mm) or higher Z semiconductors such as GaAs and CZT are also available to improve the sensitivity and detection efficiency of the device in future design[147, 148]. A schematic of the assembled detector is shown in Figure 3.4

Each analog signal processing cell within Timepix is radiation-hardened and includes a preamplifier, discriminator and counter [149]. Discriminators are used to suppress noise and select the energy range of interest; the discriminators can be adjusted

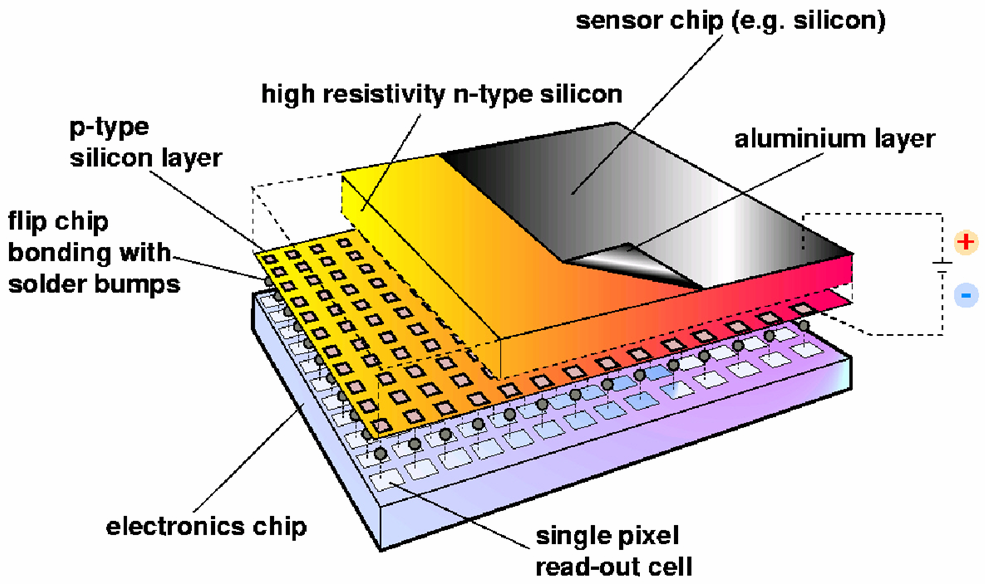

Figure 3.4: Schematic of the Timepix detector coupled electrically to a pixelated radiation sensor array[146].

globally and with a per-pixel fine adjustment to compensate for the non-uniformity of detector response. Each pixel of Timepix can be independently configured to operate in one of the following four modes [149, 146]:

- Masked mode, in which no counts are collected for that pixel (for example, if the pixel is permanently damaged);
- Medipix mode, which counts the number of detected particles but does not provide temporal information
- Time over Threshold (ToT) mode, which permits the measurement of particle energy; and
- Time of Arrival (ToA) mode, which permits the measurement of the time of interaction of each particle.

For this application, Timepix is used in count mode. The schematic of an individual Timepix pixel is shown in Figure 3.5. The block diagram is divided into the following

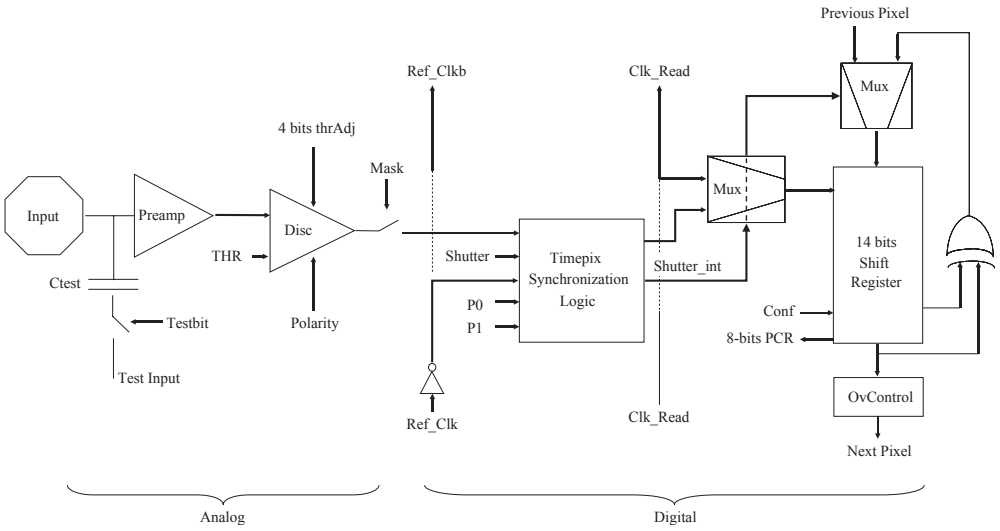

Figure 3.5: Schematic of a Timepix pixel [149]

two main functional blocks [145, 149]:

- The analog block, composed of a preamplifier which is DC coupled to a polarity-controlled discriminator with 4 bit threshold adjustment; and
- The digital block, which includes the Timepix Synchronisation Logic (TSL) and a Pixel Configuration Register (PCR).

An external reference clock signal is buffered and used to synchronise the internal counters. Each pixel is configured using its own 8 bit PCR. Four bits contain control the equaliser threashold, one bit is used as a pixel mask, and two bits are select the mode of operation (counting, ToT or ToA) [149].

The electron-hole pairs resulting from interactions between ionising radiation and the sensitive detector volume are collected by the detector anode (and common cathode) and integrated. The output is compared to a global threshold (fine-tuned by the 4 bit pixel specific threshold adjustment). When the pre-amplifier output exceeds the threshold, a pulse is generated with a duration proportional to the input pulse height (i.e. time spent above the threshold). The readout process for the entire chip

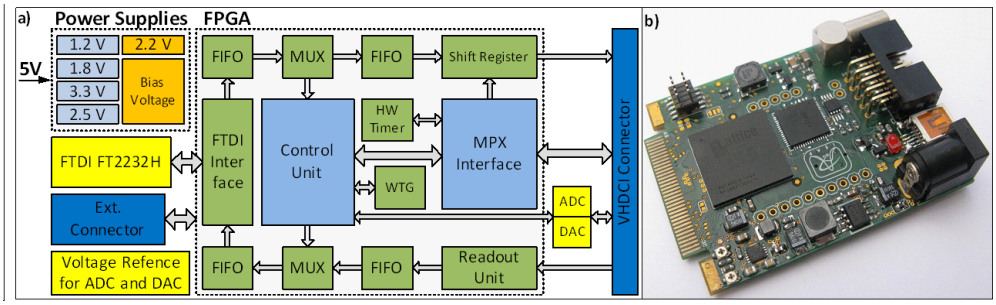

Figure 3.6: Schematic of the Fitpix interface [151]

is triggered when the `shutter` signal goes high; when the `shutter` is low, the counter for each pixel is incremented after each detected photon when the chip is operating in Medipix (counting) mode, while in ToT mode it increments with each clock pulse (at a rate of 10 MHz) while the pulse exceeds the threshold and in ToA mode the counter counts from the moment of detection until the moment of readout, giving a timestamp for the first event detected prior to readout [149].

An associated Field Programmable Gate Array (FPGA) controlled USB readout system (Fitpix) is used to communicate with the detector; its block diagram is shown in Figure 3.6. The Fitpix data acquisition system consists of a FPGA, and analog and digital interfaces to the chip. It also provides a bias voltage to the detector (powered from the USB interface) and supports all of the Timepix modes of operation. Through its associated user interface *Pixelman*, the mode of operation (counting, ToT or ToA), clock frequency and source (internal/external) and trigger mode (internal, external) are chosen [150]. A single Fitpix module can manage an array of up to sixteen Timpix chips, making it a suitable interface to the quad-Timepix array used in *HDR BrachyView* .

Therefore, the complete imaging system consists of a 4 $\times$ 1 array of Timepix detectors and their associated FPGA-controlled USB readout system (Fitpix). The total sensitive detector area is 15 $\times$ 60 mm^2 (with a thickness of 300 μm). The Timepix/-Fitpix system allows a frame rate of about 20 frames per second to be obtained with

very low electronic noise [152, 149].

3.3 Collimator Material and Thickness

The material and thickness of the semi-cylindrical shell collimator is selected to block as many of the photons which do not intersect with the apex of the pinholes as practically possible. The previously-discussed spatial constraints limit the outer diameter of the cylindrical shell to a maximum of 25 mm. Since the width of the Timepix detector (along the x-axis) is 14 mm, after allowing for the thickness of the outer rigid plastic shell, the maximum possible thickness of the collimator is 4 mm.

The remainder of this Section provides a brief introduction to the physics of photon interactions with matter and the mass attenuation coefficient, followed by discussion on the choice of the *HDR BrachyView* collimator material and its performance along with the impact of penetrated photons on the signal to noise ratio.

3.3.1 Photon Interaction with Matter and Photon Attenuation

When traversing a region containing matter, photons may interact with the medium through absorption or scattering, or penetrate the medium without interaction. Which of these outcomes applies to a given photon is random, however the probabilities of each case are well-defined and depend on the properties and thickness of the material. Assuming the probability a photon's absorption along its path through some material is μ per unit thickness, then the fraction of photons which penetrate through a thickness L of this material is expressed by the following equation [153, 154]:

$$\frac{N_L}{N_0} = e^{-\mu L} \tag{3.2}$$

where N_0 is the number of incident photons and N_L is the number of penetrating photons. This equation does not account for secondary photons (e.g. resulting from fluorescence). μ is a linear attenuation coefficient and determined by weighted composition of material, atomic number of ingredients and photon energy. It is often normalised by the density of the attenuating material as the ratio μ/ρ; in this form it is referred to as the "mass linear attenuation coefficient". Equation 3.2 can be rearranged to express the number of photons which penetrate a slab of material of thickness L:

$$N_L = N_0 \times e^{-\mu L} \tag{3.3}$$

This model applies to the situation where a collimated radiation beam is attenuated by an obstruction and detected by a small detector - that is, a photon can only reach the detector if it did not interact with material comprising the obstruction. A table of mass linear attenuation coefficient for elements (from $Z = 1$ to 92) and some common compounds (for energies between 1 keV and 20 MeV) can be found on the National Institute of Standards and Technology (NIST) website [155]. Generally, the mass linear attenuation coefficient is higher when the atomic number is higher.

In the case where multiple kinds of interactions must be considered during the attenuation, μ can be expressed as:

$$\mu = \sum_{i=1}^{n} \mu_i \tag{3.4}$$

where μ_i, the *partial linear attenuation coefficient*, refers to the probability of the ith process occurring when a photon travels through a unit depth of material.

Photons and matter can interact in five different ways, the three most important of which are the photoelectric effect, Compton scattering and pair production; the other two interactions, Rayleigh scattering and photonuclear interaction, would occur

extremely rarely in this application and are not discussed here. The probability with which an interaction occurs when a photon travels through some material is mainly determined by the energy of the photon and the atomic number of the material. For a given material, the dominant interaction at low photon energies (above the minimum ionisation energy for the element or compound) is the photoelectric effect; as energy increases, Compton scattering increasingly dominates (although photoelectric interactions are still possible); and for energies exceeding the rest mass of an electron-positron pair, pair production (particle-antiparticle pair generation) begins to become more probable, dominating at high energies. For example, for photons travelling through lead ($Z = 82$), the photoelectric effect dominates at photon energy above 7.41666 eV and below approximately 500 keV, pair production dominates at photon energy higher than approximately 4.5 MeV and Compton scattering dominates for the photon energy range in between. Let τ, σ and κ be the partial linear attenuation coefficients for the photoelectric effect, Compton scattering and pair production respectively. (3.4) can be written as:

$$\mu = \tau + \sigma + \kappa \tag{3.5}$$

By substituting (3.5) into (3.2), the fraction of photons which do not interact after passing through a depth of L of matter can be written as:

$$\frac{N_L}{N_0} = e^{-(\tau+\sigma+\kappa)L} \tag{3.6}$$

In HDR brachytherapy, the radiation from the source usually contains photons with a range of different energies. In this case, The total population of the photons after attenuation by matter can be calculated as the sum of the remaining photons calculated for each energy separately. Assuming that the radiation beam contains photons with n different energies, the total number of photons (N_0) before attenuation

can be expressed as:

$$N_0 = \sum_{i=1}^{n} N_0 \times p_i \tag{3.7}$$

where p_i is the emission probability of photons with energy in the ith energy bin. Let μ_i be the linear attenuation coefficient for the ith energy. Applying (3.3) to (3.7), the population of photons remaining in the beam after attenuation by a material of thickness of L for photons beam with multiple energies can be obtained as:

$$N_L = \sum_{i=1}^{n} N_0 \times p_i \times e^{-\mu_i L} \tag{3.8}$$

or in the form of fraction:

$$\frac{N_L}{N_0} = \sum_{i=1}^{n} p_i \times e^{-\mu_i L} \tag{3.9}$$

3.3.2 Comparison of the Attenuation of Photons from HDR Source for Different Collimator Materials

^{192}Ir is most commonly used radioactive source in HDR brachytherapy, and is a source of both β and γ radiation. The therapeutic action is primarily due to the γ-rays emitted from ^{192}Ir $\rightarrow$^{192}Os electron-capture decay, which results in a range of γ photon energies. The spectrum of photons emitted by ^{192}Ir is complicated, covering energies ranging from 10 keV to nearly 900 keV with an average energy of 380 keV. Although a rough calculation of photon attenuation can be performed using the mean energy, ignoring the true energy spectrum will result in an overestimate of the value of $\frac{N_L}{N_0}$ when the absorbing material is thin, and an underestimate when the material is thick. When a multi-energy photon beam enters an attenuating medium, photons with lower energy are more likely to be attenuated (i.e. μ is larger); conversely, higher-energy

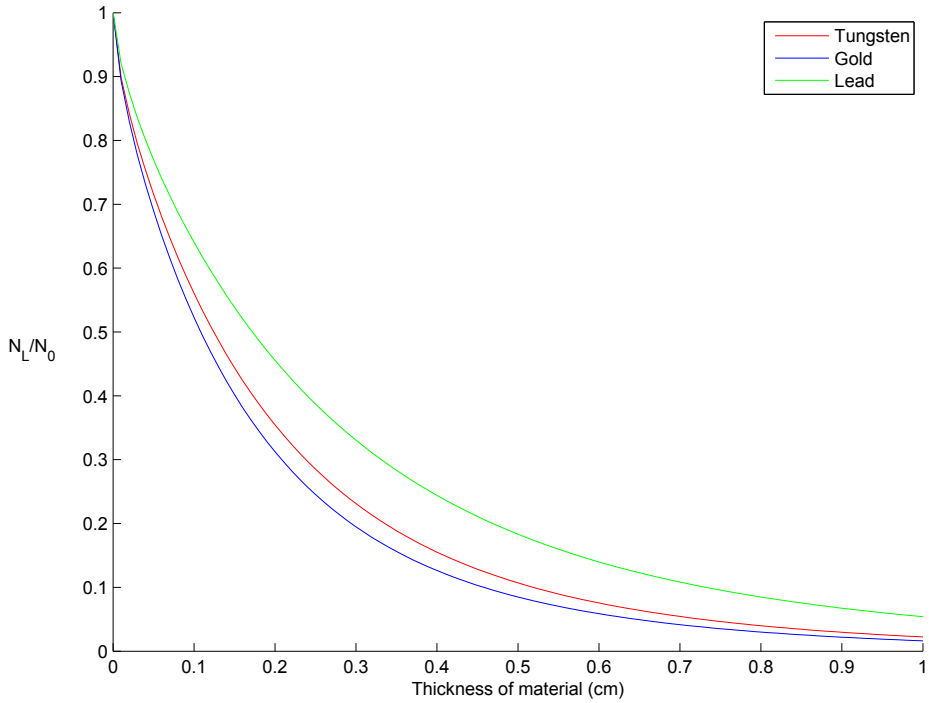

Figure 3.7: $\frac{N_L}{N_0}$ calculated with the linear attenuation coefficients of all energies included in ^{192}Ir emitting photon spectrum for different attenuating material.

photons are more likely to pass through (μ is lower). Thus as L increases, the lower-energy photons are more severely attenuated than the high energy photons leading to a shift in the average energy towards the high-energy end of the spectrum.

Table 3.1 listed the mass lineear attenuation coefficients and linear attenuation coefficients for tungsten, lead and gold at all the energies included in ^{192}Ir 's spectrum[156, 155]. These materials are potential candidates for *HDR BrachyView* 's collimator due to their high attenuation coefficients. Since most of the specific energies of interest are not specifically listed in NIST's data, the actual value of mass lineear attenuation coefficient for each energy listed in Table 3.1 is a linearly interpolation between the two closest energies listed in NIST's published. The linear attenuation coefficients are calculated by multiplying the mass lineear attenuation coefficients with the density of each material.

The ratio $\frac{N_L}{N_0}$ for each of the three proposed materials is calculated using the full

		Tungsten		**Lead**		**Gold**	
Primary Energy	Emission Probability (%)	μ/ρ (cm^2/g)	μ (cm^{-1})	μ/ρ (cm^2/g)	μ (cm^{-1})	μ/ρ (cm^2/g)	μ (cm^{-1})
10.5 keV	2.46	217.518	4187.228	120.125	1362.213	107.082	2066.685
64 keV	4.54	3.225	62.090	4.501	51.037	4.059	78.346
75 keV	1.22	9.442	181.767	3.070	34.808	2.771	53.475
136.5 keV	0.08	2.365	45.522	2.968	33.662	2.750	53.084
201.5 keV	0.20	0.777	14.967	0.990	11.222	0.913	17.625
205.5 keV	1.41	0.759	14.612	0.966	10.952	0.891	17.202
283.5 keV	0.11	0.400	7.696	0.501	5.685	0.465	8.968
295.5 keV	12.21	0.345	6.632	0.430	4.875	0.399	7.701
308.5 keV	12.7	0.313	6.018	0.389	4.407	0.361	6.969
316.5 keV	35.04	0.302	5.816	0.375	4.252	0.349	6.728
374.5 keV	0.30	0.226	4.350	0.276	3.128	0.258	4.977
416.5 keV	0.28	0.183	3.532	0.221	2.502	0.207	4.000
468.5 keV	20.23	0.155	2.984	0.184	2.084	0.173	3.348
484.5 keV	1.34	0.146	2.816	0.172	1.955	0.163	3.147
489.5 keV	0.18	0.144	2.763	0.169	1.915	0.160	3.085
588.5 keV	1.90	0.113	2.167	0.129	1.463	0.123	2.379
604.5 keV	3.45	0.109	2.092	0.124	1.406	0.119	2.290
612.5 keV	2.23	0.108	2.070	0.123	1.390	0.117	2.264
884.5 keV	0.12	0.075	1.435	0.081	0.921	0.079	1.526

Table 3.1: Primary ^{192}Ir photon energies with their respective emission probabilities, mass lineear attenuation coefficients and linear attenuation coefficients.

spectrum of ^{192}Ir and plotted in Figure 3.7. Among the three materials, gold offers the greatest photon attenuation, followed by tungsten and lead. Although lead has the highest atomic number and mass lineear attenuation coefficients among these three materials for photons with energy above 100 keV, its linear attenuation coefficient is the smallest because of its relatively low density compared to gold and tungsten. As shown in Figure 3.7, the curves level off (i.e. $\frac{N_L}{N_0}$ does not significantly change with respect to the thickness of material) beyond approximately 8 mm for tungsten and gold and 10 mm for lead. Furthermore, to attenuate 90% of the photons emitted by ^{192}Ir , requires a thickness of 4.7 mm for gold, 5.3 mm for tungsten and 7.4 mm for lead (calculated with the full spectrum of ^{192}Ir). Although gold would be the best choice of material for its ability to attenuate photons emitted by ^{192}Ir , tungsten is almost as effective while being a fraction of the cost and with greatly superior mechanical properties (hardness and strength). Therefore, tungsten is chosen as the optimal material for the *HDR BrachyView* probe.

As previously mentioned, it is impractical to make the wall of *HDR BrachyView* thicker than 4 mm. Thus, with a 4 mm thick tungsten collimator, a non-trivial fraction of the photons emitted by the ^{192}Ir source will still able to penetrate the collimator. The effect of these *penetrated photons* will be investigated in the following section (Section. 3.3.3).

3.3.3 Impact of Penetrated Photons on Source Imaging

In pinhole-collimated imaging system, the photons arriving at the detector can be classified into three categories: direct photons, penetrated photons and scattered photons (Figure 3.8). Direct photons are defined as photons reached the detector by travelling through pinhole aperture. Both penetrated and scattered photons are photons which have travelled through the collimator body before they reach the detector. The dif-

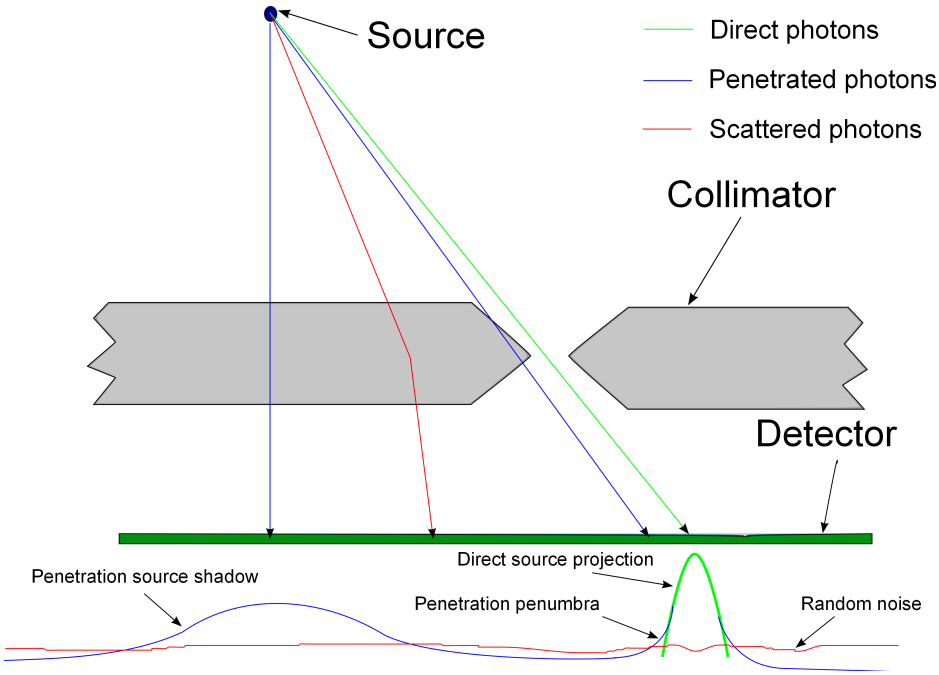

Figure 3.8: This figure shows three classes of photons detected by detector - direct, penetrated and scattered (+ secondary). An intensity profile of an acquired image is also plotted to illustrate the different components of the image.

ference is that penetrated photons have no interaction with the collimator material, while scattered photons have interacted with the collimator material, resulting in a change in momentum [157]. In these Thesis, secondary photons (those resulting from X-ray fluorescence in the collimator) are also included in the scattered photons.

For a pinhole gamma camera, these three classes of photons contribute to different components of a image. All of the direct photons, which contain most of the useful information of source position, contribute to the projection of an image of the source onto the detector plane. The scattered (and secondary) photons no longer provide much useful information regarding source position because their momentum is changed during the interaction with the collimator. Thus, the scattered photons manifest as two-dimensional random noise, with a maxiumum directly under the source and a very wide spread; this contributes to a continuum of background noise in the image. Penetrated photons retain some information regarding source position, although they

have passed through the body of the collimator. However, it is difficult to make use of the source position information carried by the penetrated photons during the back projection since they are not collimated by pinhole. The penetrated photons have two significant impacts on imaging in *HDR BrachyView* . The first is due to penetration through the edge of the pinhole, where the thickness of the collimator is less than in the main body of the collimator. This has the effect of enlarging the source projection. The second effect is a region of pixels in the area of the detector immediately under the source with excess counts compared to the background. This effect is more significant when the source is closer to the collimator, since as the source moves farther away, the radiation field resulting from penetrated photons becomes both less intense and more uniform across the detector. Importantly, for 4 mm thick tungsten, the photon counts seen in the penetrated component of the image are much lower than those in the direct projection component, while the scattered / secondary photon component is even less significant. Although *HDR BrachyView* uses the CoMs of the observed projections to track the position of source centre independently of the size of the source projections, the effect of photon penetration through the edge of the pinholes may still contribute a small error in determining the CoMs. This is because other than the case where the source is immediately above the pinhole, the attenuation of photons passing through different regions of pinhole edge will be different, which will result in a small asymmetric perturbation of the source projections. In addition, if the source projections are too large, the projections of the source from two neighbouring pinholes may overlap. This problem can be avoided by ensuring sufficient separation of pinholes and limiting the collimator-detector distance; the ability of *HDR BrachyView* to distinguish the projections from two adjacent pinholes is validated in Chapter. 6. The second effect of penetrated photons - the increased photon counts immediately under the source - will be treated specifically later in this subsection.

As illustrated in Figure 3.8, the high count region immediately under the source is denoted the *penetration source shadow* (PSS). The *Direct source projection* (DSP) is defined as the area of pixels with counts corresponding to the detection of direct photons. The extended region surrounding the DSP region caused by photons penetrating through the edge of pinhole is defined as *penetration penumbra* (PP). The combination of DSP and PP is denoted the *extended source projection* (ESP). However the exact region of ESP is difficult to define due the highly specific dependence on the geometry of the source position, pinhole geometry and pinhole location. For simplicity, any region of source projection including the DSP and all or part of the PP is referred to as ESP.

As previously discussed, the thickness of the *HDR BrachyView* collimator is 4 mm. From the calculation of $\frac{N_L}{N_0}$ (plotted in Figure 3.7), more than 16% of photons from an ^{192}Ir source are able to pass through a 4 mm thick tungsten collimator. These penetrated photons boost the level of background counts, resulting in the need to use a higher threshold to properly isolate the ESP or DSP. Thus, a critical capability for the *HDR BrachyView* probe is whether the source projections can be distinguished from the PSS. To validate the capability of source projection isolation in *HDR BrachyView* , the signal to background ratio (SBR), which is represented by the ratio of the counts in each pixel in region of PSS (C_{PSS}) and DSP (C_{DSP}) will be considered.

Considering a photon beam with a fixed spectrum. The photon count observed in each pixel (C) in a photon detector is proportional to the number of photons that impinge on the detector (N, which can be expressed as:

$$C = A \times N \tag{3.10}$$

where A is a coefficient determined by the spectrum of photon and the properties of the detector. Assuming the response of all pixels in the detector is uniform, and

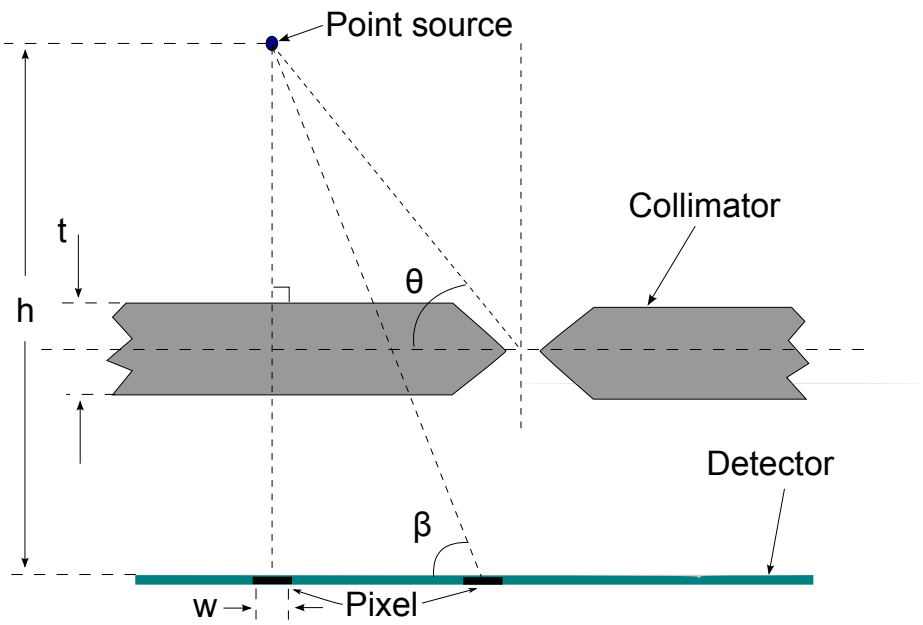

Figure 3.9: Figure demonstrating the calculation of $\frac{N_{PSS}}{N_{DSP}}$. h is the height between the source and the top surface of detector; t is the thickness of the collimator; θ is the incidence angle from the source to pinhole centre; β is the incidence angle from the source to an arbitrary pixel of the detector; W is the width of pixel.

neglecting the effect on A of changes in the spectrum resulting from attenuation due to the passing through the patient's body and the collimator, for a photon counting detector, C_{PSS} and C_{DSP} can be expressed as:

$$C_{PSS} = A \times N_{PSS} \tag{3.11}$$

$$C_{DSP} = A \times N_{DSP} \tag{3.12}$$

where N_{PSS} and N_{DSP} are the number of photons which arrive at each pixel in the PSS and DSP regions, respectively. Thus,

$$\frac{C_{PSS}}{C_{DSP}} = \frac{N_{PSS}}{N_{DSP}} \tag{3.13}$$

Let N_{total} be the total number of photons emitted from the ^{192}Ir source per unit

time, β be the angle of photon incidence to an arbitrary pixel, h be the height of source above the detector plane and S_{pixel} be the area of each pixel (Figure 3.9). The number of photons which can reach an arbitrary pixel per unit time can be expressed as:

$$N = \frac{S_{pixel} sin\beta}{4\pi(\frac{h}{sin\beta})^2} \times N_{total} \times \sum_{i=1}^{n} p_i \times e^{-\mu_i L} \tag{3.14}$$

Assuming the source is placed above the full thickness of the collimator (i.e., outside of the acceptance cone of the pinhole), the maximum value of N_{PSS} is obtained when $\beta = 90°$. This is denoted as M_{PSS}. Then, N_{PSS} and N_{DSP} can be derived from (3.14) as:

$$M_{PSS} = \frac{S_{pixel}}{4\pi h^2} \times N_{total} \times \sum_{i=1}^{n} p_i \times e^{-\mu_i t} \tag{3.15}$$

$$N_{DSP} = \frac{S_{pixel} sin\theta}{4\pi(\frac{h}{sin\theta})^2} \times N_{total} = \frac{S_{pixel} sin^3\theta}{4\pi h^2} \times N_{total} \tag{3.16}$$

Here, θ is the incidence angle of direct photon (Figure 3.9). The term $\sum_{i=1}^{n} p_i \times e^{-\mu_i t}$ in (3.15) is the fraction of photons that can pass through the body of the collimator, which has been derived previously in (3.9) and shown to equal approximately 16% for the case of the *HDR BrachyView* collimator. By dividing (3.15) with (3.16), the ratio of M_{PSS} and N_{DSP} is:

$$\frac{M_{PSS}}{N_{DSP}} = \frac{\sum_{i=1}^{n} p_i \times e^{-\mu_i t}}{sin^3\theta} \tag{3.17}$$

Then, substituting the value of 16% into $\sum_{i=1}^{n} p_i \times e^{-\mu_i t}$ into (3.17), a formula yielding $\frac{M_{PSS}}{N_{DSP}}$ for the *HDR BrachyView* design can be obtained as:

$$\frac{M_{PSS}}{N_{DSP}} = \frac{0.16}{sin^3\theta} \tag{3.18}$$

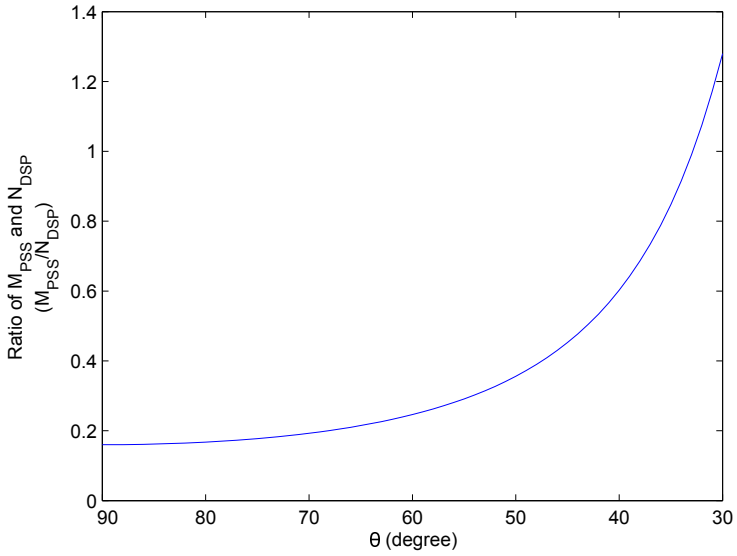

Figure 3.10: Ratio of M$_P SS$ and N$_D SP$ against θ

Figure 3.10 shows a plot of $\frac{M_{PSS}}{N_{DSP}}$ calculated using (3.18) with θ from 90° to 30°. Since $\frac{M_{PSS}}{N_{DSP}}$ is proportional to $sin^{-3}\theta$, it increases slowly with the decreasing of θ at the beginning, then rapidly increasing with decreased θ. M_{PSS} becomes larger than N_{DSP} when θ is smaller than 32°. In this case, the projection of the source cannot be distinguished from the background by simply applying a threshold. Although an edge detection method may be able to detect the edge of the projection, it is difficult to apply in reality, since unexpected structures or patterns may also be detected by the edge detection algorithm when the background is not successfully filtered out.

The algorithm for the segmentation of source projections will be discussed in Section 4.2.1.

3.4 Pinhole Geometry

Two different pinhole geometries were considered for the *HDR BrachyView* collimator: a single-cone and double-cone structure. The two alternative designs were evaluated via Monte Carlo simulations with a simulated ^{192}Ir point source. The results from

these simulations were compared in terms of sensitivity, signal to background ratio and resolution in order to choose the optimal pinhole geometry for this application. This section begins with the designs of both single-cone and double-cone pinholes, followed by an introduction to the Geant4 Monte Carlo simulation platform. The results from a set of Monte-Carlo simulations is presented to compare the performance of the two alternative pinhole designs, resulting in the adoption of the double-pinhole geometry. The optimal position of the pinholes along the central axis of the probe is then calculated such that the probe can unambiguously resolve the source position anywhere within the entire prostate volume.

The concept of *ideal centre of mass* ($\mathrm{CoM_i}$) for a projection is defined here for convenience. The $\mathrm{CoM_i}$ of a projection of an active source through a pinhole is defined as the projection of the centre of the source's active volume onto the detector plane through the centre of such pinhole. It is distinct from the CoM of the projection image, which is affected by many geometric and physical artefacts, including the penetrated and scattered photons and the path length differences travelled by photons emitted from different points along the axis of a cylindrical point source. The actual CoM obtained from these images is only an approximation of $\mathrm{CoM_i}$.

3.4.1 Design of pinholes

The detector is placed 1.5 mm above the central axis of the probe (Figure 3.3). To maximum the FOV, the optimal acceptance angle of the pinholes, denoted α, is determined as:

$$\alpha = 2 \times \tan^{-1}(\frac{W_d}{2 \times H_{pd}}) \tag{3.19}$$

where W_d is the width of the detector (14 mm) and H_{pd} is the height of pinhole centre above the detector plane. For the double-cone pinhole (Figure 3.11(a)), the

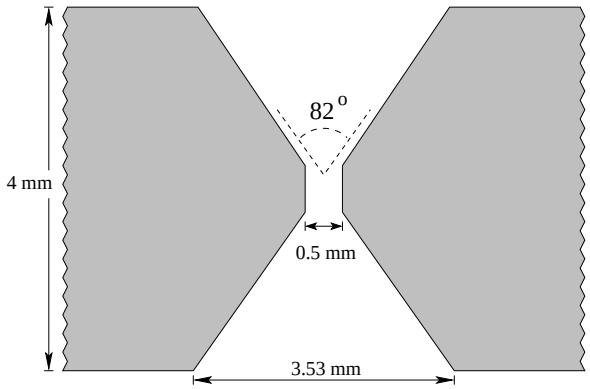

(a) Double-cone pinhole

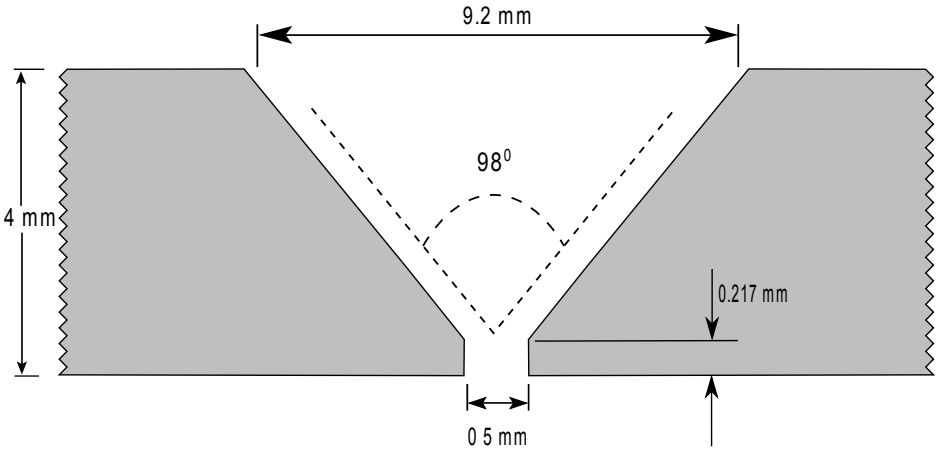

(b) Single-cone pinhole

Figure 3.11: Cross section of the probe showing different potential pinhole geometries.

centre of pinhole's aperture is located half-way through the thickness of the collimator body. In this case, $H_{pd} = 8.5$ mm, resulting in $\alpha = 82°$. For the single-cone pinhole, the centre of the pinhole's aperture is located on the inner surface of the collimator. This results in a H_{pd} being 2 mm less than for the double-cone geometry. Therefore, the opening angle $\alpha = 98°$, which is slightly larger than for the double-cone design (Figure 3.11(b)). Instead of using a knife-edge pinhole, a 0.5 mm diameter cylindrical channel is added at the aperture of pinhole to increase the fraction of direct photons and to simplify the alignment of the drilling of the two cones in the double-cone design (by the use of a pilot hole).

3.4.2 Monte Carlo Simulations with Geant4

Geant4 is a C++-based Monte Carlo simulation platform which is capable of accurately modelling the interactions of radiation and matter [158, 159]. Geant4 was originally developed for use in high energy physics, but is increasingly being used for other applications including space science and medical physics. A Geant4 simulation requires the following to be defined:

- The geometry of the simulation;
- The physics interactions;
- The generation of primary particles; and
- The acquisition of data through the simulation.

Accurate models of complex structures can be built with the help of the abstractions provided by Geant4. Geometries in Geant4 are defined through three layers: the *solid volume*, *logical volume* and *physical volume*. The geometry of the each component is defined in the solid volume. Geant4 provides functions to create a group of elementary shapes and a set of operations which may be performed between these shapes.

Irregular shapes can be achieved by the intersection or union of the basic geometries. The logical volume defines the physical properties of the component, such as the material properties and whether it is a *sensitive volume* (i.e. part of a detector). The material may defined in different ways, depending on whether it is a single element or a compound; a single element can be directly defined in terms of its atomic number, mass number and density, while compounds are defined by their density and the proportions of individual elements in the compound (which must already be defined). After the shape and physical properties of the geometry are determined, its spatial position and orientation in relation to the other defined components in the system is defined by the physical volume. In Geant4, all the components except the *world volume* have to be enclosed within another component, with which it has a 'mother-daughter' relation. The world volume is the whole volume of the simulation, which containing all other volumes. Each component may have multiple daughter volumes, but only one mother volume.

The physics interactions of interest in the simulation are defined in libraries associated with each respective particle, and in some cases a number of alternative models can be used for the same particle. The Geant4 Low Energy package, using the Livermore Evaluated Data Library, was employed to model the physics interactions in the simulations involved in this Thesis. The Livermore Library is able to accurately track and simulate the interaction of electrons and photons in the range from 250 eV to 1 GeV, including the thresholds below which secondary particles cease to be tracked. After a secondary particle is generated through an interaction, the energy and range of the particle is compared to these thresholds, and will only be stored for further analysis when its energy or range is larger than the threshold, otherwise all the energy of the secondary particle will be considered to be absorbed in the position where it was generated.

The primary particle is the initial particle that the simulation starts to track, and is defined in terms of the particle type, energy, position and momentum. After the simulation starts, the status of the tracked particles can be retrieved at different points in the tracking process. Geant4 provides functions to access the information of the tracked particle and its interaction with the geometric objects through which it is travelling either before or after each calculation (either interaction or transportation of the particles).

A comparison of different pinhole shapes using a point source is presented in the following part of this section, since it was conducted prior to the finalisation of the design of *HDR BrachyView* . The Monte Carlo evaluation of source tracking capabilities of the final pinhole design is presented in Chapter 6, while the Monte Carlo evaluation of dose enhancement in rectum due to the backscatter dose from the *HDR BrachyView* probe is presented in Chapter 5.

3.4.3 Monte Carlo Evaluation of Alternative Pinhole Geometries

To investigate the response of two alternative pinhole designs for *HDR BrachyView* to radiation from a point ^{192}Ir source, Monte Carlo simulations were performed using Geant4.9.4. In this subsection, the geometric models for a double-cone and single-cone pinhole design are described, and the results of the Monte Carlo simulations of each design will be evaluated in term of sensitivity, signal to background ratio and resolution.

3.4.3.1 Simulating Single-Cone vs. Double-Cone Pinhole Geometries

The models of single-cone and double-cone shape pinhole described in Section 3.4.1 were developed in Geant4. The point source images obtained with these models were

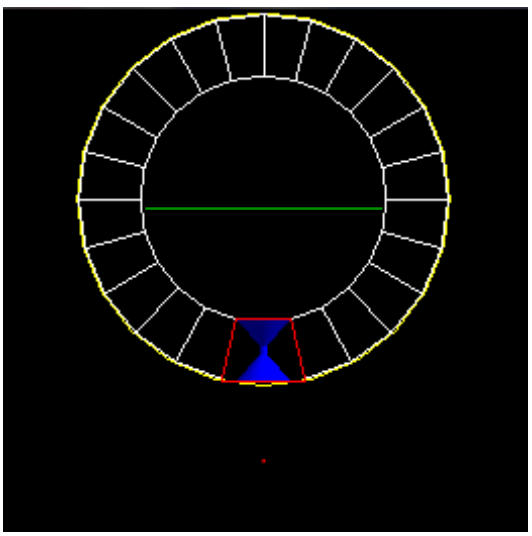

(a) Transversal cross-section of double-cone pinhole geometryl

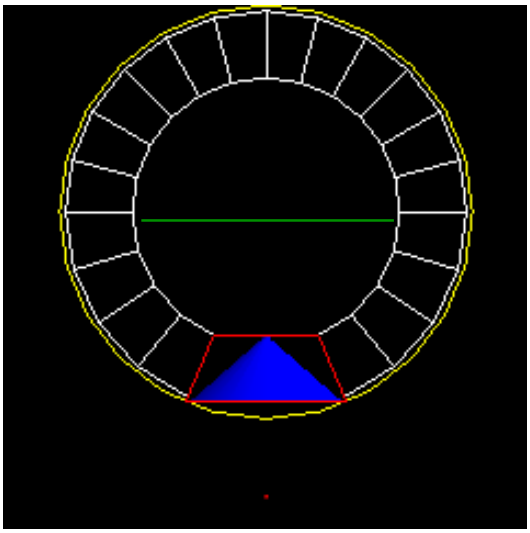

(b) Transversal cross-section of single-cone pinhole geometry

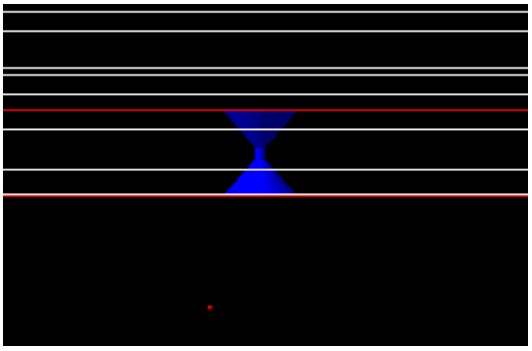

(c) Longitudinal cross-section of double-cone pinhole geometry

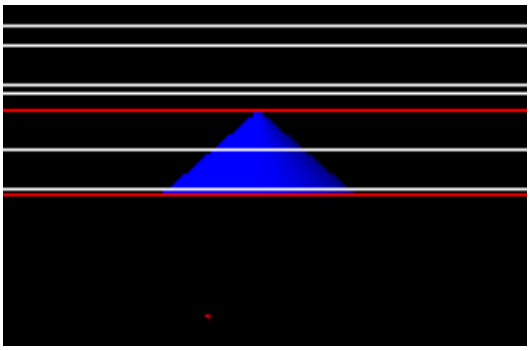

(d) Longitudinal cross-section of single-cone pinhole geometry

Figure 3.12: Visualization of Geant4 models with different pinhole design.

analysed to select the best pinhole geometry for *HDR BrachyView* . Figure 3.12 illustrates the simulations for evaluating the two proposed pinhole geometries. The collimator was modelled as a cylindrical tungsten tube with a wall thickness of 4 mm and is shown in Figure 3.12(a) and 3.12(b). The pinholes (shown in blue in Figure 3.12) with double-cone and single-cone pinhole geometries (as discussed in the previous description) were modelled in corresponding simulations. In this group of simulations, only one pinhole is simulated at a time, as this is sufficient to compare the sensitivity, signal-to-background ratio and spatial resolution achievable with each design. The pixelated silicon detector (shown in green in Figure 3.12) is placed 1.5 mm above the central axis of the tungsten collimator. To simplify the geometric description of the pinhole in Geant4, the area immediately surrounding the pinhole was approximated as a trapezoidal prism (shown as the red trapezoid in Figure 3.12). A 0.6 mm diameter sphere of ^{192}Ir, encapsulated in a 0.15 mm thick steel shell, was used as the model for the point source (shown as the red dot in Figure 3.12). The geometry of the steel shell is identical to the thickness of the model of the microSelection HDR source (^{192}Ir) used to simulate the attenuation of the source shell [156]. For both models, the centre of the point source was placed 5 mm above the collimator and 2.34 mm away from the centres of the of pinholes, which are spread parallel to of the axis of probe. The materials and their compositions are shown in Table 3.2.

Limited to the computing time, it is not feasible to generate the total number of photons emitted in 1 s by a HDR source. 20 billion photon events were generated in each simulation, which are sufficient to generate a solvable image. The photon energy distribution was generated according to the spectrum of ^{192}Ir (see Table 3.3) [156]. It is assumed that all beta radiation is absorbed by the steel shell and the surrounding phantom. To improve the simulation speed, different thresholds for the of production of secondary particles were applied by creating a virtual volume of interest.

Table 3.2: Table shows the materials used in the GEANT4 simulations

Compound	Element	Weight (%)	Atomic Number	Mass Number (g/mole)	Density (g/cm^3)
Water	H	66.67	1	1.01	1
	O	33.33	8	16	
Steel	Si	1	14	28	8.02
	Cr	19	24	52	
	Mn	2	25	54.9	
	Fe	68	26	55.8	
	Ni	10	28	58.7	
Air	N	75	7	14	1.2×10^{-3}
	O	25	8	16	
	Ir		77	192	22.39
	W		74	183.84	19.25

This virtual volume is a cylinder with a diameter slightly larger than the probe and concentric to the probe (shown as the yellow circle in Figure 3.12(a) and 3.12(b)). The cut-off range of secondary particles was set as 4 mm outside the virtual volume and 1 μm inside the virtual volume (secondary particles with range smaller than the threshold will release all their energy at the place it generated and will not be tracked). In each pixel, the energy deposited was recorded for each event and a count will be generated when the energy deposited by an event was exceeding a threshold (16 keV).

The simulated projection maps obtained from the simulations are then used to evaluate the SBR, FWHM and the efficiency of the two different pinhole geometries. The SBRs of the images were calculated as the ratio of the mean counts in two regions selected in the projection and on the image background. A one-dimensional profile in the direction along the axis of the probe was produced for each image by averaging 10 columns which intersect with the centre of the projection. The profile was fitted using a Gaussian function, and the FWHMs of the projections in each image was then calculated from the profile.

Usually, the efficiency of a photon counting detector can be evaluated using its sensitivity. The sensitivity can be defined as the percentage of photons emitted from

Table 3.3: Primary ^{192}Ir photon energies and their respective emission probabilities per decay used in GEANT4 simulations.

Primary Energy	Emission Probability(%)
10.5 keV	2.46
64 keV	4.54
75 keV	1.22
136.5 keV	0.08
201.5 keV	0.20
205.5 keV	1.41
283.5 keV	0.11
295.5 keV	12.21
308.5 keV	12.7
316.5 keV	35.04
374.5 keV	0.30
416.5 keV	0.28
468.5 keV	20.23
484.5 keV	1.34
489.5 keV	0.18
588.5 keV	1.90
604.5 keV	3.45
612.5 keV	2.23
884.5 keV	0.12

the source which are detected by the detector. Since the counts generated by the detector is proportional to the number of photon detected, the sensitivity of each design was calculated as the ratio of the total counts of the corresponding image to the number of photons generated in each simulation. However, since the approach of *HDR BrachyView* is to track the source centre using the CoMs of the source projections, the evaluation of detector efficiency should relate to the statistics of correctly locating the CoM. In addition to the sensitivity of the detector (represented by the total counts of the image), the uncertainty in calculating the CoM also depends on the dispersion of the projection from its CoM. The CoM is the sample mean of the coordinates of all the photons detected by the detector (all counts in all the pixels) within the projection of source. Thus, the uncertainty of using the calculated CoM to estimate $\mathrm{CoM_i}$ can be evaluated using the standard error of the sample mean (SEM). Statistically, the SEM represents the range of the interval within which a given sample mean (i.e. the mean of a sampled subset of the entire population) is expected to fall. A small SEM means that sufficient samples have been taken to give a good estimate of the true mean value of the population. For example, for a normally-distributed random variable, there is a 95% probability that the for a given sample size, the sample mean will fall within $\pm 1.96\times$ SEM.

After the source projection was selected by applying a threshold of a certain percentage of the maximum count observed in the image, the SEM can be calculated as:

$$SEM = \frac{\sigma}{\sqrt{n}} \tag{3.20}$$

where σ is the standard deviation of the distribution and n is the sample size. While the true value of σ is unknown, it can be estimated by the standard deviation

of the set of samples. Then (3.20) could be rewritten as:

$$SEM = \frac{S}{\sqrt{n}} \tag{3.21}$$

where S is the standard deviation of the sample set. It can be obtained by applying a 2D Gaussian fit to the projection region or directly calculated as,

$$S_i = \sqrt{\frac{\sum\limits_{Proj} C(i,j) \cdot (i - i_{CoM})^2}{\sum\limits_{Proj} C(i,j)}} \tag{3.22}$$

$$S_j = \sqrt{\frac{\sum\limits_{Proj} C(i,j) \cdot (j - j_{CoM})^2}{\sum\limits_{Proj} C(i,j)}} \tag{3.23}$$

where $(i_{CoM},\ j_{CoM})$ are the coordinates of the CoM, $(i,\ j)$ are the coordinate indices of each pixel within the projection and $C(i,\ j)$ is the photon count in pixel $(i,\ j)$.

3.4.3.2 Results

Figure 3.13 shows the projected images of the point source placed in the positions described in Section 3.4.3.1 through the double-cone and single-cone pinhole designs. From these images, it is clear that the boundary of the projection obtained from the double-cone pinhole model is better defined compared to that obtained from the single-cone pinhole, in which the projection is spread across the whole detector area. The regions selected to calculate the signal to background ratio are shown as the red squares in Figure 3.13. These two background sample regions are visually determined, which are uniform and outside the projection region. The position right under the source (2.34 mm from the pinhole centre) was not selected because such position is still covered by the opening of the pinhole, which results to much higher counts

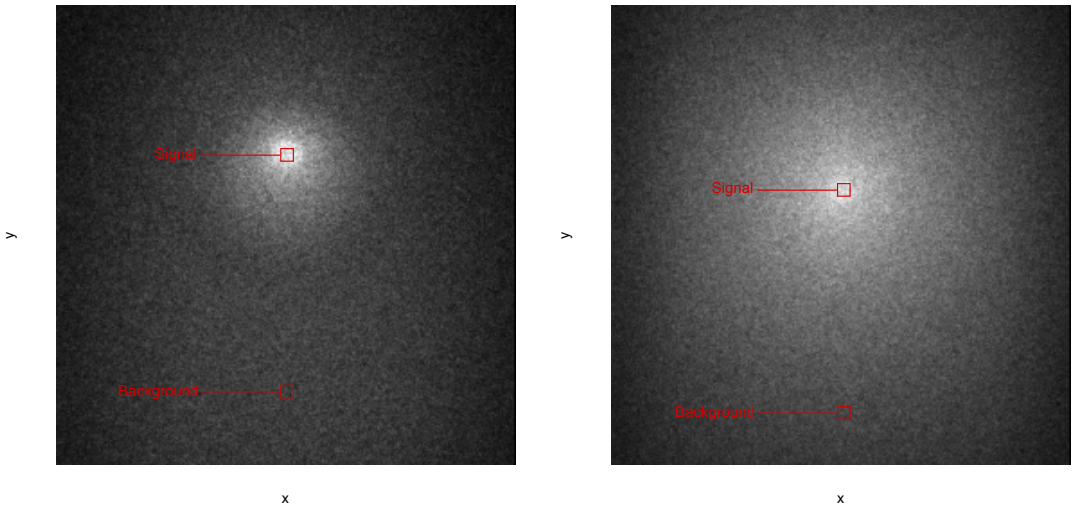

(a) Double-cone pinhole geometry (b) Single-cone pinhole geometry

Figure 3.13: Projection images of a point source obtained from both proposed pinhole geometries.

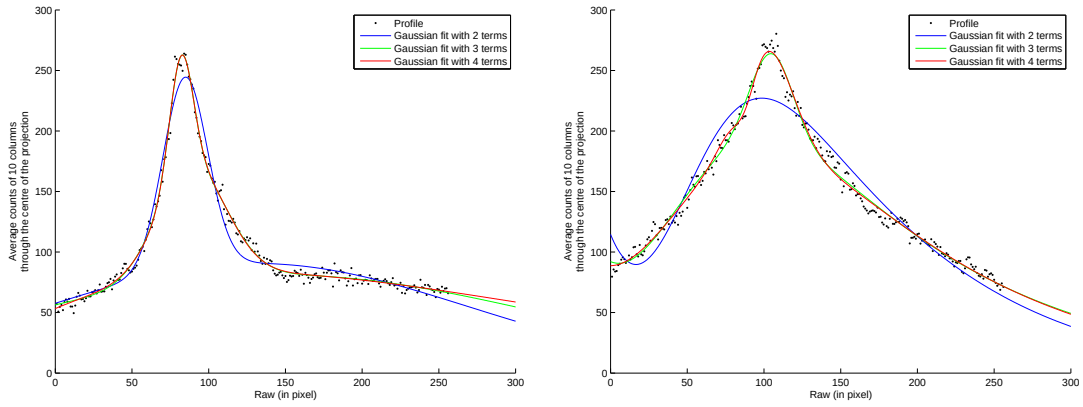

(a) Double-cone pinhole geometry (b) Single-cone pinhole geometry

Figure 3.14: Profiles through the centre of the source projection in images obtained from each pinhole design. The curves fitted using Gaussian functions with a varying number of terms are also plotted in each profile.

Table 3.4: Characteristics of the single-cone and double-cone pinhole designs

	Double Cone	Single Cone
Mean Counts in Projection	256.14	269.23
Mean Counts in Backgroud	71.96	88.58
SBR	3.56	3.04
FWHM	30.00	71.00
Sensitivity	0.21%	0.33%
SEM (x direction, th=50%)	0.0214	0.0206
SEM (y direction, th=50%)	0.0212	0.0211

compared to region shielded by full thickness of tungsten. The line profile through the centre of the projection in the image from each design is plotted in Figure 3.14. At least 3 terms are required in a Gaussian function to accurately fit the curve to the profile.

The SBR, FWHM, sensitivity and SEM of both pinhole designs are listed in Table 3.4. The SBR of the image from the double-cone pinhole is 3.56, which is approximately 20% higher than the SBR of the image from the single-cone design (3.04). The FWHM of the profile for the double-cone pinhole is less than half of the FWHM for the single-cone pinhole, which are 30 pixels and 71 pixels correspondingly. The sensitivity of the double-cone design is lower, at approximately 63% of the single-cone design. Considering the sensitivity calculated includes significant amount of photons refer to the leakage of the tungsten shielding, the efficiency of the detector can not be evaluated only by the sensitivity. Furthermore, the high sensitivity observed for single cone shape design also indicates its lower capability of background radiation shielding. In this case, the SEM is more relevant for the evaluation of detector efficiency. The SEM in the two designs are similar in both x and y directions when the source projections were isolated using a threshold set at 50% of the maximum.

The SEM of projections selected by different thresholds are shown in Figure 3.15. A smaller SEM in both x and y directions was observed from the projection obtained from the double-cone design. In particular, the SEM for the double-cone design is

significantly smaller than the SEM for the single-cone design when the threshold is high (approximately half for thresholds greater than 75% of the maximum). The SEMs for both designs decrease rapidly with the reduction of threshold until it reaches 75% of the maximum, after which the SEM of the double-cone shape design starts to rise slowly while the SEM of the single cone design continues to gradually decrease. The SEM of both designs converges to a similar level (approximately 0.02) when the threshold is less than 55% of the maximum.

3.4.4 Discussion

The results demonstrate the capability of *HDR BrachyView* to distinguish between the projection of a point source and the background due to the penetrated and scattered / secondary photons, while the boundary of the source projection is more clearly defined in the case of the double-cone designed compared to the single-cone geometry. Although the mean counts in the projection region of the image from the single-cone pinhole design are slightly higher, its SBR is lower than the double-cone design because of the high background level in the image from the single-cone design. Gaussian functions with at least 3 terms are needed to provide a good fit to the line profile. This is due to the complex relationship between the photon path length and the position of detector pixels along the profile. The count distributions corresponding to the photons travelled though the aperture of pinhole, cone shape opening and the full thickness of tungsten could be represented by the different terms of the Gaussian fit. The smaller FWHM observed in the image of the double-cone design is expected since its full opening angle (the sum of the opening angle at the top and bottom of the pinhole; the opening angle for the bottom of the single-cone design is considered to be 180°) is much smaller than for the single-cone design. Although the sensitivity of the double-cone pinhole is significantly lower, the resulting from using its source

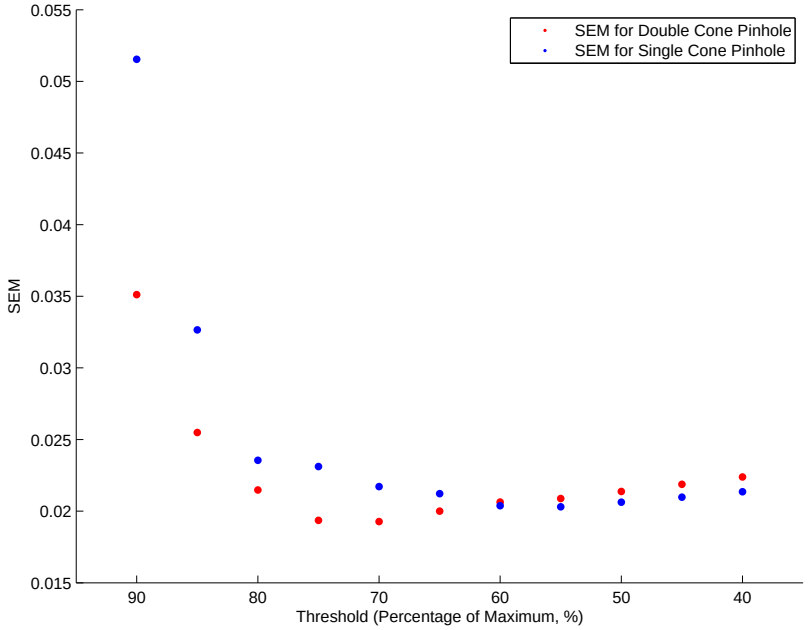

(a) x

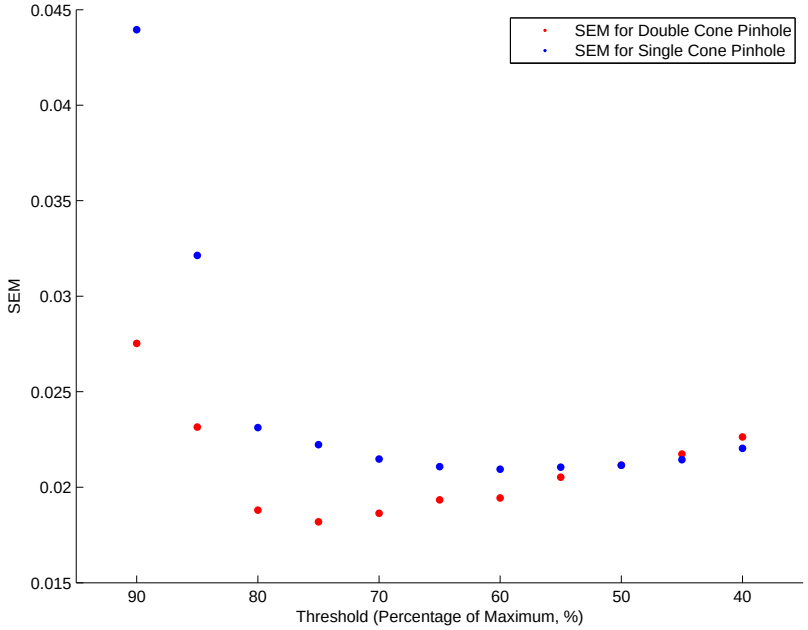

(b) y

Figure 3.15: SEM of source projection in x and y directions with varying thresholds

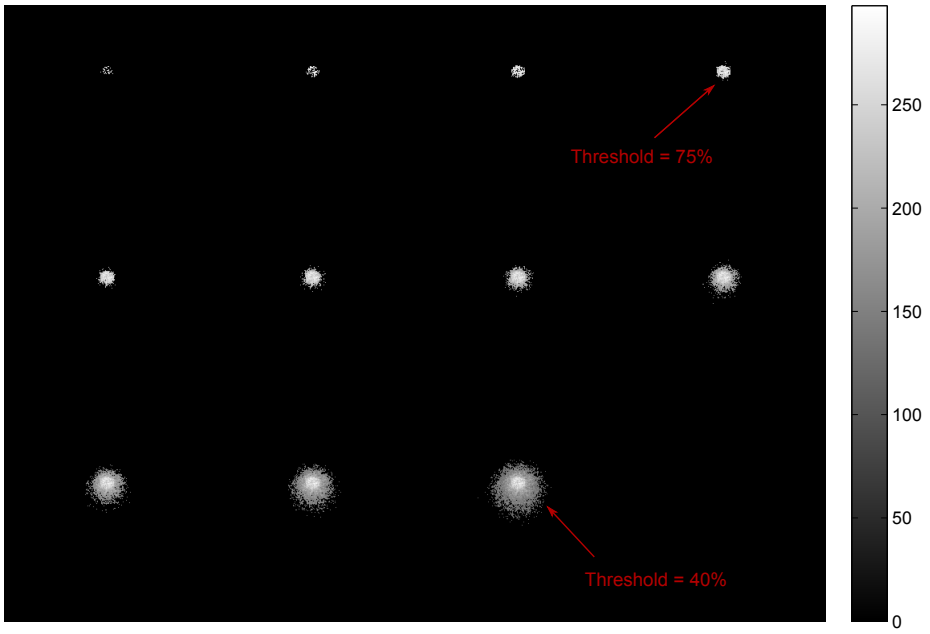

Figure 3.16: Projection subsets selected by applying different thresholds (as a percentage of the maximum count value observed). The thresholds are from 90% to 40% of the maximum with a step of 5%, corresponding to the projection from the top-left corner to the bottom-right corner.

projection to estimate the CoM is superior (i.e. it exhibits a lower SEM) compared to the single-cone design. The difference in SEM is significant when the threshold was higher than 75% of the maximum. In practice, thresholds higher than 65% were applied to the data from the simulations and experiments due to the high penetration of photons, which will be discussed in detail in subsequent chapters. For a threshold of 65%, the SEM of double-cone pinhole is still slightly lower than for the single-cone design.

The increase observed in the SEM when the threshold is below 75% of the maximum results from the pixels in the penetration penumbra region (defined in Section 3.3.3) starting to distort the shape of projection, by adding more additional brightness to one side of the projection than the other. This can be seen in Figure 3.16; after the threshold is reduced below 75%, more scattered outliers start to appear in the area sur-

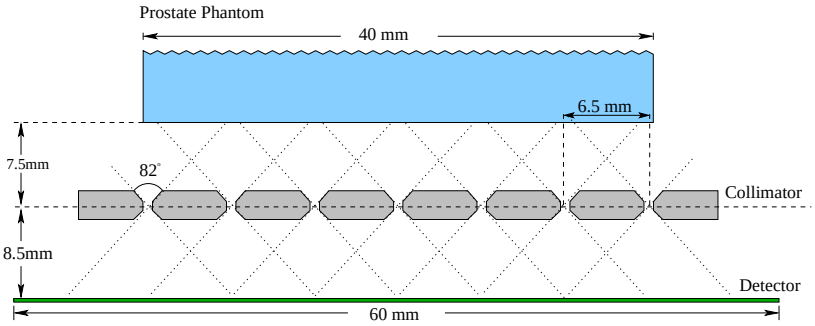

Figure 3.17: Pinhole array capable of covering the entire potential treatment volume prostate with at least two projections.

rounding the concentrated bright central region in the projection. The distinct regions of direct source projection and penetration penumbra can be clearly distinguished in the last projection in the set (with the lowest threshold of 40%).

Although the single-cone pinhole is able to provide a slightly wider FoV, it also leads to a larger ratio of h_{sp} to h_{pd}, which magnifies the systemic errors in source tracking with the pinhole imaging system. In addition, the disadvantage of a smaller FoV for the double-cone pinhole could be overcome by increasing the number of pinholes along the probe (to extend the FoV in the yz plane) and rotating the probe before the source delivery in each catheter (to extend the FoV in the xz plane). Thus, the double-cone pinhole is the best choice for the *HDR BrachyView* probe because of the superior resolution, SBR and efficiency that it offers.

Following the selection of the double-cone pinhole geometry, the number and spacing of pinholes can be determined in order to ensure that at least two projections of the source are visible from all positions within the prostate volume (the source can be tracked when two or more projections are visible on the detector). Seven pinholes, uniformly spaced at intervals of 6.5 mm along a straight line parallel to the y axis of the probe, will be sufficient to accomplish this. The resulting design is shown in Figure 3.17.

3.5 Conclusion

This Chapter presents the design of the *HDR BrachyView* probe in detail. Monte Carlo simulations were performed to compare the performance of two alternative pinhole designs, based on double-cone and single-cone geometries. The double-cone pinhole geometry was chosen for *HDR BrachyView* over the single-cone design due to the superior spatial resolution that it can achieve, and its ability to obtain lower uncertainty for determining the CoM of the source projection within a given acquisition time. However, the acceptance angle of one double-cone pinhole located within the rectum is insufficient to cover the entire prostate. Therefore, to achieve a field of view (FoV) which is sufficient to cover the entire target volume, a total of seven uniformly spaced collinear pinholes were required.

In the following Chapter, the process of source tracking in three dimensions will be discussed in detail.

Chapter 4

Image Processing and Source Tracking

This Chapter describes the source tracking techniques used in *HDR BrachyView* . Each step in the sequence is described, from image acquisition to 3D position estimation. The calculation of the source position within the treatment volume is based on an analysis of the projections of the source through the pinholes. Since the source projections on the imaging plane are obtained by detecting the photons emitted from each point of the source, the *geometric* centre of mass (CoM) of each projection represents the projection of the source centre through the corresponding pinhole (however, as discussed in the previous chapter, a number of additional factors bias the estimated position of the CoM). Therefore, the centre of mass of the source can be estimated by computing the intersection of the lines projected from the CoMs of each projection through the centres of their corresponding pinholes. In practice, due to the intrinsic noise in the projections, the projected lines are unlikely to ever intersect at a single mathematical point; therefore, the best solution is the point with the minimum total perpendicular distance to the set of projection lines (i.e. the least-squares solution).

The software which implements the source position tracking algorithm is writ-

ten in Matlab. It is highly modular, with the full three dimensional source position calculation calculation process split into a series of independent functions, for convenient debugging and future modification. Since a dedicated user interface for *HDR BrachyView* will eventually be developed using C++, some of Matlab's native functions are replaced with low-level implementations to simplify porting to C++ or other high-level languages in the future.

A general flowchart illustrating the process by which the source location is calculated is shown in Figure 4.1.

The process of image acquisition is briefly described in Section 4.1. The localisation of the CoMs is discussed in Section 4.2 and the calculation of source position within the treatment volume is discussed in Section 4.3. The Matlab software developed to implement each part are also introduced, the source code of which is included in Appendix A.

4.1 Image Acquisition

Images acquired by the detector array are recorded on a host PC, which interfaces with Timepix through a FPGA-controlled USB readout system (Fitpix) [151]. The process of configuring and equalising the detector and acquiring image frames is controlled by a user interface, *Pixelman*, which was developed by the Medipix collaboration for use with the Medipix2/Timepix ASICs [150]. In the final design of *HDR BrachyView* , a plug-in for Pixelman will be designed for the image processing and three dimensional source position calculation. However, at this stage, the source projection images obtained from simulations or experiments were analysed by proof-of-concept software developed in Matlab. Therefore, frames downloaded from the Timepix array via Fitpix and Pixelman are recorded to ASCII output files for convenient importation into Matlab.

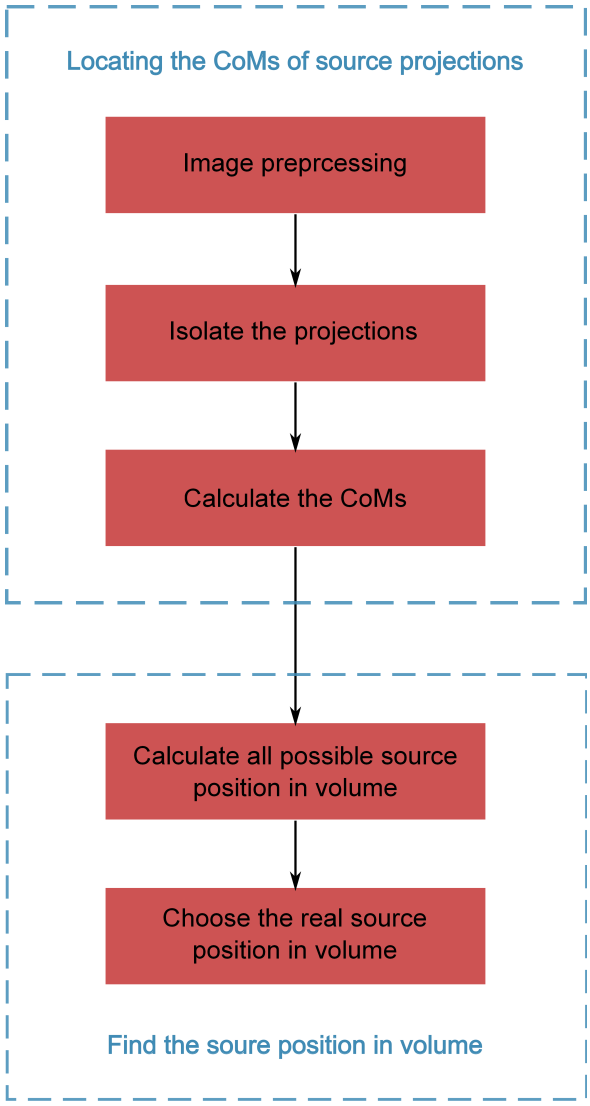

Figure 4.1: Flow chart showing the process of the calculation of the source position within the treatment volume

4.2 Locating the CoM

The process of locating CoMs can be generalised as isolating the source projections and averaging the coordinates of pixels in each projection weighted by the pixels' counts. Prior to source projection isolation, the image from *HDR BrachyView* probe is preprocessed for the noise reduction. Threshold equalisation and gap correction/interpolation may also be performed in this stage if required, depending on the condition of detectors array (for example, if there are any regions of dead or noisy pixels). Threshold equalisation requires calibration of the Timepix detector array in a dark environment and in a flat radiation field; calibration coefficients are then saved by Pixelman and can be used during subsequent acquisitions. If regions of the detectors are defective, they can also be masked out and the missing pixel values estimated through bilinear interpolation from either side of the damaged region. This will be discussed in greater depth in Chapter 7, where it needs to be applied to deal with a gap caused by defective pixels at the border of two chips in the array.

Noise reduction is performed using a 2D median filter, implemented with the Matlab function `medfilt2()`. Since accurate localisation of the CoM is highly dependent on the symmetry of the projection, median filtering has only a minor impact on the accuracy of finding the CoM.

4.2.1 Projection Isolation

As discussed previously, due to significant penetration of the high energy components in the spectrum of ^{192}Ir through the 4 mm tungsten collimator, the background counts are high and there is no sharply-defined boundary for the projections obtained by *HDR BrachyView* system. In this case, gradient based image segmentation methods such as the well-known Canny edge detection algorithm are not effective at isolating the projections (Figure 4.2(b)) [160]. Instead, in *HDR BrachyView* , source projections are

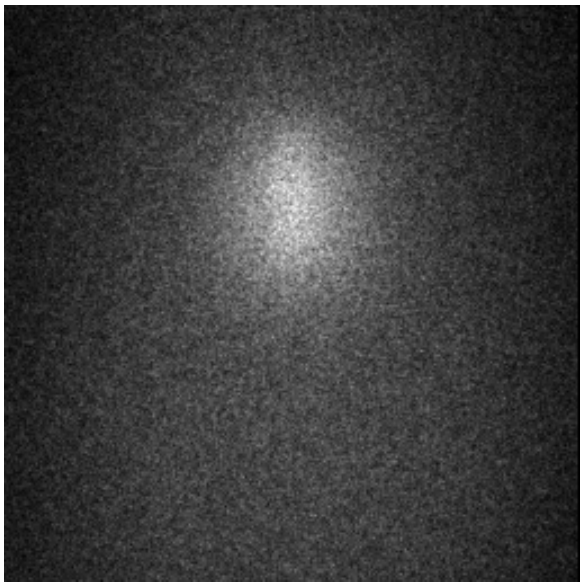

(a) Sample image showing a single projection

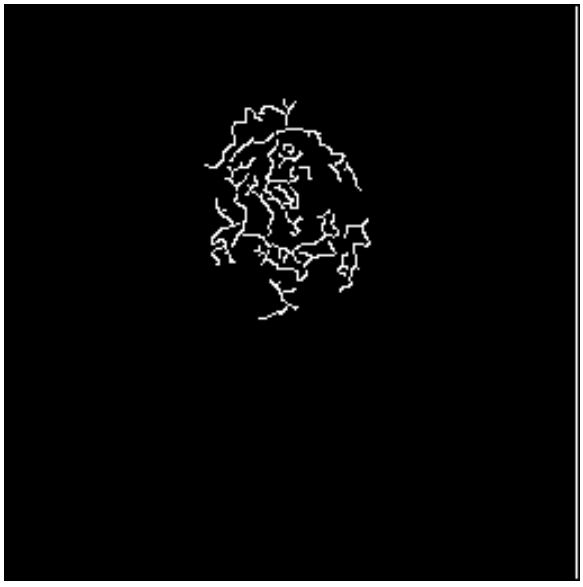

(b) Canny edge detection algorithm applied to the sample image

Figure 4.2: Canny's edge detection algorithm applied to a simulated source projection. Edge detection is performed with a threshold of 0.6, which is the lowest threshold that can remove all the background. Due to the high level of speckle in the image, the Canny algorithm is unable to identify the boundary of the projection.

isolated by simple thresholding. Unlike traditional thresholding which returns a binary image, the pixel values above the threshold are retained, while pixels with counts below the threshold are considered as background and are eliminated by setting their value to 0. Thus, if matrix $Im(i,\ j)$ represents the original image, the thresholded image can be expressed mathematically as:

$$Im_{th}(i,j) = \begin{cases} Im(i,j), & Im(i,j) \geq T \\ 0, & Im(i,j) < T \end{cases} \tag{4.1}$$

where T is the threshold. The pixels value in the region of the projection are preserved as the weight when averaging the coordinates in each projection for the calculation of CoM.

The optimal choice of threshold can be defined as that which results in the best possible estimate of the CoM location. Because of the high background count from the penetrated photons, the threshold value usually needs to be at least 65% of the maximum, based on observations of both simulations and experiments. In addition, the locally optimal threshold value may change according to the source position. Therefore, a dynamically-adjusted threshold method is necessary. Gonzalez and Woods introduced an iterative method to automatically determine a suitable image segmentation threshold, which is widely used in digital image processing [161]. It starts with an initial estimation of the threshold T_0, which is used to segment the image into two subsets G_h and G_l:

$$\begin{aligned} G_h &= \{\ Im(i,j) \mid Im(i,j) \geq T_i\ \} \\ G_l &= \{\ Im(i,j) \mid Im(i,j) < T_i\ \} \end{aligned} \tag{4.2}$$

Then a new threshold value can be calculated:

$$T_{i+1} = \frac{1}{2} \times (\overline{G_h} + \overline{G_l}) \tag{4.3}$$

If the difference between T_{i+1} and T_i is smaller than a predefined limit, the algorithm is terminated; otherwise, it repeats until T converges. (4.3) implies that the result of the iterative algorithm is the median value of the average of the pixel values in the two groups delineated by the threshold. However, as previously mentioned, the optimal threshold for CoM determination is usually larger, especially when the source is close to the edge. Figure 4.3(b) shows the result of thresholding with the above iterative method. Considerable background counts remain in the thresholded image. Although this problem could be improved by weighting more to the average of G_h in (4.3), the outcome is ambiguous and hard to precisely control. Matlab also provides an inbuilt function (`graythresh.m`) which can automatically determine a threshold using Otsu's method, but the projections are still unable to be isolated in the threshold image (Figure 4.3(a)) [162].

Since the statistical information in each projection depends on the its size, an optimal method to automatically determine the optimal threshold is to use the number of remaining pixel clusters (source projections) as the threshold condition. Assuming only one projection is contained in the image, the size of the isolated source projection is determine by the number total number of the pixels remaining after thresholding, which can be assessed from the histogram of the image. Thus, a threshold method based on the image histogram can be used to achieve a successful dynamic threshold. In this method, the whole range of pixel counts is equally divided into B_{counts} bins. A histogram of these bins is generated as $H_{(i)} = N_i$, where N_i is the number of pixels with a count within the range of the ith bin, $i = 1.2, \ldots B_{counts}$. Then the cumulative

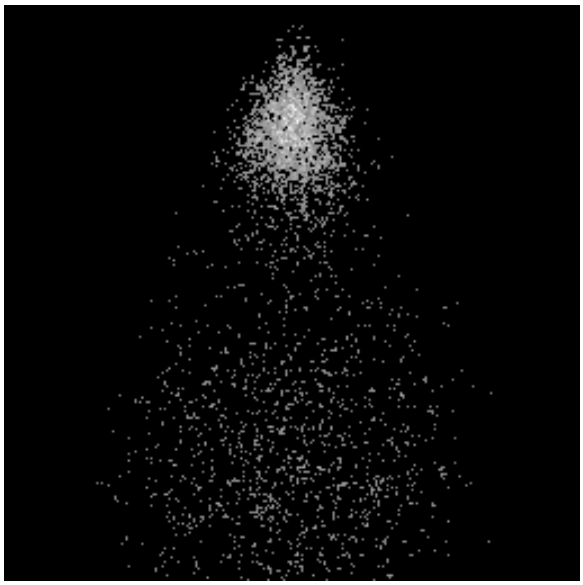

(a) Otsu's method

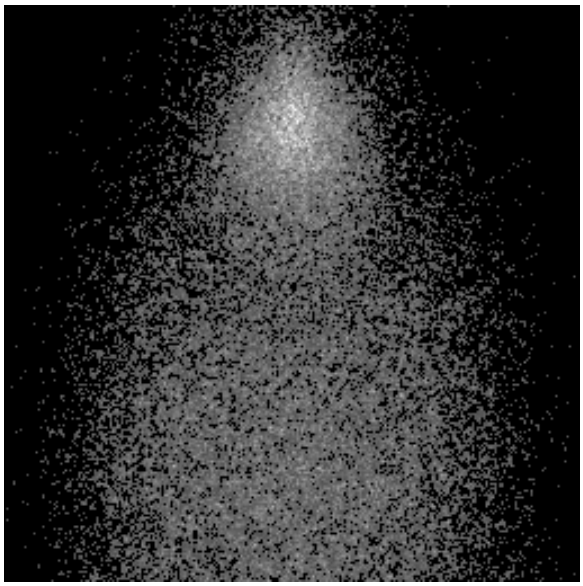

(b) Iterative method (Gonzales and Woods, 2004)

Figure 4.3: Images segmented by different automatic thresholding algorithms

sum of the histogram is calculated:

$$CH_{(i)} = \sum_{j=0}^{i} H_{(j)} \tag{4.4}$$

Subsequently, the threshold (T) can be determined by comparing the cumulative sum to the expected value of the total number of remaining pixels, which is denoted the *pixel number threshold* (T_{PN}).

$$T = \frac{M_{counts}}{B_{counts}} \times max\{\ i \mid CH_i \leq CH_{B_{counts}} - T_{PN}\ \} \tag{4.5}$$

where M_{counts} is the maximum pixel count value in the image. Pixels with values less than T are considered as background and are eliminated by setting their value to zero.

Thus, if only one source projection is obtained, this threshold method, based on image histogram, can solve the projection segmentation problem caused by the variance of source position. However, the image obtained by *HDR BrachyView* usually contains multiple source projections, with the number of projections depending on the source position relative to the pinhole array. In this case, T_{PN} has to be the total number of the pixels in all of the extracted projections. In addition, due to the difference of the distances between the source and each pinhole, the overall counts seen in source projections corresponding to different pinholes are each unique to that projection, which further leads to the disparity of the sizes of isolated projections. Problems occur when the difference in projection sizes is too large, in which case the smallest projection may not contained sufficient statistics to accurately calculate its CoM while the largest projection contained too many penetrated or scattered photons. Therefore, blindly applying this algorithm to a multi-projection image will result in unacceptably high uncertainty in CoM determination and cause a significant systematic shift from

the ideal centre of mass when attempting to locate the CoM (Figure 4.4(b)). This problem can be addressed by segmenting the image into regions, each of which only contains a single projection, and performing pixel number thresholding independently within each region.

During the regional thresholding process, the image is coarsely segmented into regions, each containing a single source projection, and different thresholds are applied on each of these regions (the threshold could be same if the threshold method is based on the sub-region histogram). This is achieved by using a simple weak global threshold to isolate the approximate position of the projection CoMs, and then performing image segmentation centred on these approximate locations to separate these projections from each other. The global threshold can be based on either a percentage of the maximum count or the histogram of the image. The width of the coarsely segmented regions is selected so that the largest expected projection size can be fully captured in a single region. Generally, applying a single global threshold is sufficient to segment all the source projections. However, thresholding and segmentation may need to be repeated multiple times on some sub-regions when more than 4 projections are detected, which may occur when the source is located far away from the collimator. In this case, after the application of the global threshold and the CoMs of recognised projections are calculated, the size of the detector area in which no source projection was detected (the *idle region*), normally located at one side of all detected projections, is compared with the average distance between each pair of detected projections. If the width of the idle region is larger than twice the average distance, the idle region will be thresholded again to obtain more potential projections. If the global threshold is based on a histogram, the T_{PN} used on the idle area (T_{PNidle}) is calculated according to its ratio to the whole-detector threshold and the number of recognized projections

(a) Before thresholding

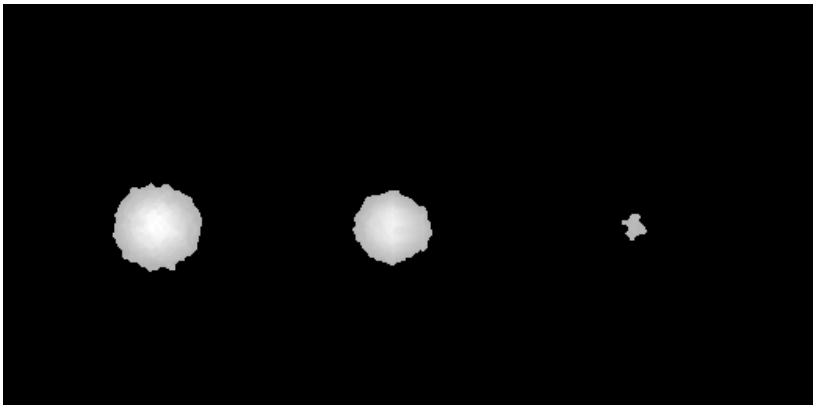

(b) After global thresholding

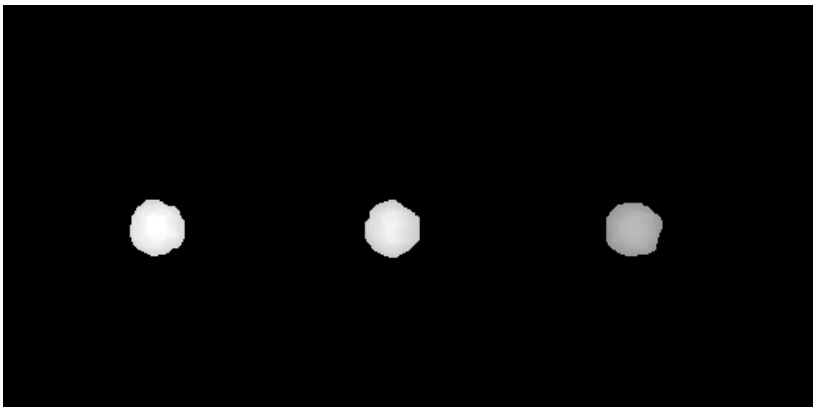

(c) After regional thresholding

Figure 4.4: Source projections isolated both by global and regional thresholds. The high count region (two vertical white strips) in the centre of Figure 4.4(a) was masked and interpolated, and will be explicitly discussed in Section 7.3.1

(N_{proj0}), which is:

$$T_{PNidle} = \frac{T_{PN0}}{N_{proj0}} \times \lfloor N_{proj0} \times \frac{A_{idle}}{A_{whole} - A_{idle}} \rfloor \tag{4.6}$$

where T_{PN0} is the T_{PN} just applied, A_{idle} is the area of the idle region and A_{whole} is the area of the whole detector.

After the coarse segmentation isolates the approximate regions containing the projections, all pixels which are not included in any regions are eliminated while the pixels within each region are left untouched. Then a T_{PN} corresponding to the expected size of single source projection is applied to each selected region. Figure 4.4(c) demonstrated the source projections isolated using a regional threshold method.

In addition to the pixels belong to the source projections, some individual pixels with high counts, which are caused by noise or detector artefacts, may also remain in the image after thresholding. These pixels are denoted 'poison pixels' here, as if they are not removed, they can have a significant detrimental effect on the accuracy of the CoM calculation. Such poison pixels can either be scattered throughout the image, or occur in one particular row or column of the detector (typically at the edge, due to stresses induced by physically cutting the detectors from the wafer) (Figure 4.5(a)). Although some of the poison pixels may be gathered together as a cluster, the size of such clusters are usually much smaller than the size of the clusters representing the source projections. Thus, it is feasible to remove these poison pixels or clusters by using the mathematical morphology opening operator. The opening operator is a combination of erosion and dilation. During the opening operation, a image is firstly eroded by a predefined pattern matrix (the *structuring element*), then dilated by the same pattern. Since the erosion operation will eliminate any shape in the target image which is too small to contain the whole structuring element, the poison pixels can be eliminated while the cluster corresponding to the projections remain

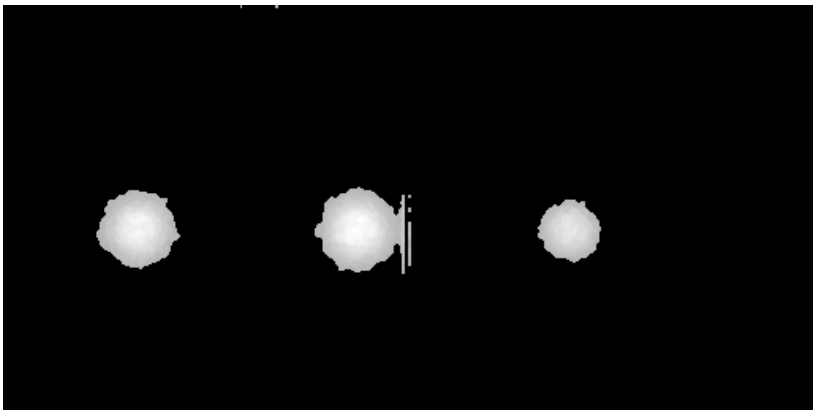

(a) Before applying the opening operator

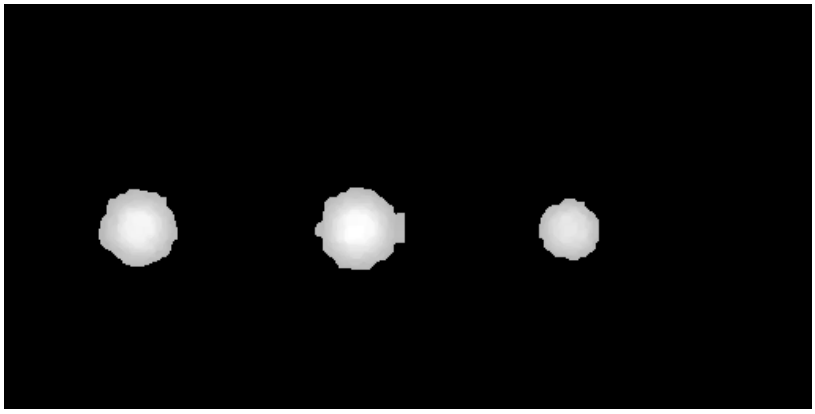

(b) After the opening operator

Figure 4.5: Images demonstrating the removing of 'poison pixels' using the mathematical morphology opening operator

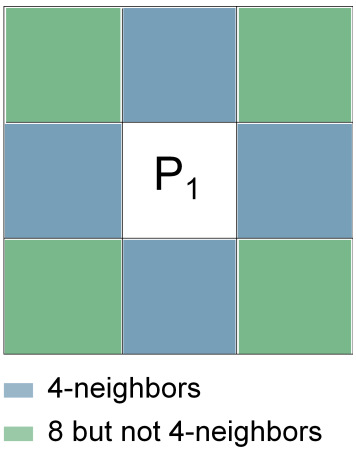

Figure 4.6: Illustration of a pixel and its 4-connected and 8-connected neighbours. The coloured pixels are the 8-neighbours of P_1, the blue pixels indicate the 4-connected neighbours of P_1, and the green pixels indicate the pixels which are 8-connected but not 4-connected neighbours of P_1

undamaged, by using a carefully-designed structure element with the proper size and shape. Subsequently, the dilation operation is applied to restore the shape of the source projections. Figure 4.5 shows the source projections before and after applying the opening operator.

4.2.2 Projection Grouping

After the image is coarsely segmented, the remaining pixels (hereafter simply referred to as 'pixels') are grouped into different clusters, which represent the source projections. Two kinds of grouping methods are employed in *HDR BrachyView* , each of which has its own advantages and disadvantages.

The first method groups pixels on the basis of the type of spatial relationship between neighbouring pixels. The definition of the relationship types starts from a simple classification of the pixels in the immediate neighbourhood of a particular pixel. The types of adjacency between two pixels (P_1, P_2) include 4-connected, 8-connected and not-connected [161]. As shown in Figure 4.6, P_2 is 4-connected to P_1 only if it shares a common edge with P_1. The connection of pixels is transmissible, which means

two pixels are also 4-connected, if they are both 4-connected to the same pixel, thus building up large contiguous areas of pixel connectivity. Thus, a 4-connected pixel cluster is defined as a cluster where all pixels contained are 4-connected. 8-connected pixel clusters is similarly defined as having at least one common vertex or common edge (i.e. all 4-connected pixels are also 8-connected) [161]. In *HDR BrachyView* , contiguous 8-connected pixels clusters in the thresholded image are selected as the source projections. The selection of 8-connected pixels clusters can be accomplished using the inbuilt Matlab function `bwlabel()`. An completely independent Matlab function for image segmentation for *HDR BrachyView* has also been built in Matlab for the convenience to more easily allow the code to be ported later to C++. This code scans all the pixels in the image and examines their 8-connected pixels. One of three operations will be performed on each image pixel, based on the relationships with its 8-neighbours:

- A pixel will be subsumed into a cluster, if all its 8-neighbours belong to only one existing cluster;
- If the 8-neighbours belong to multiple existing clusters, these clusters are merged and the scanned pixel is included in the merged cluster; and
- If the 8-neighbours of this pixel don't belong to any existing cluster, a new cluster will be created which contains the scanned pixel as an element, .

After all pixels have been processed, the index of grouped clusters and the sets of coordinates of all the clusters are outputted. The process of grouping pixels based on their neighbours is illustrated in Figure 4.7

The grouping method described above relies on an assumption that the pixels in the cluster corresponding to each projection are continually connected (8-connected). This assumption is valid in practice because of the high activity of the HDR source,

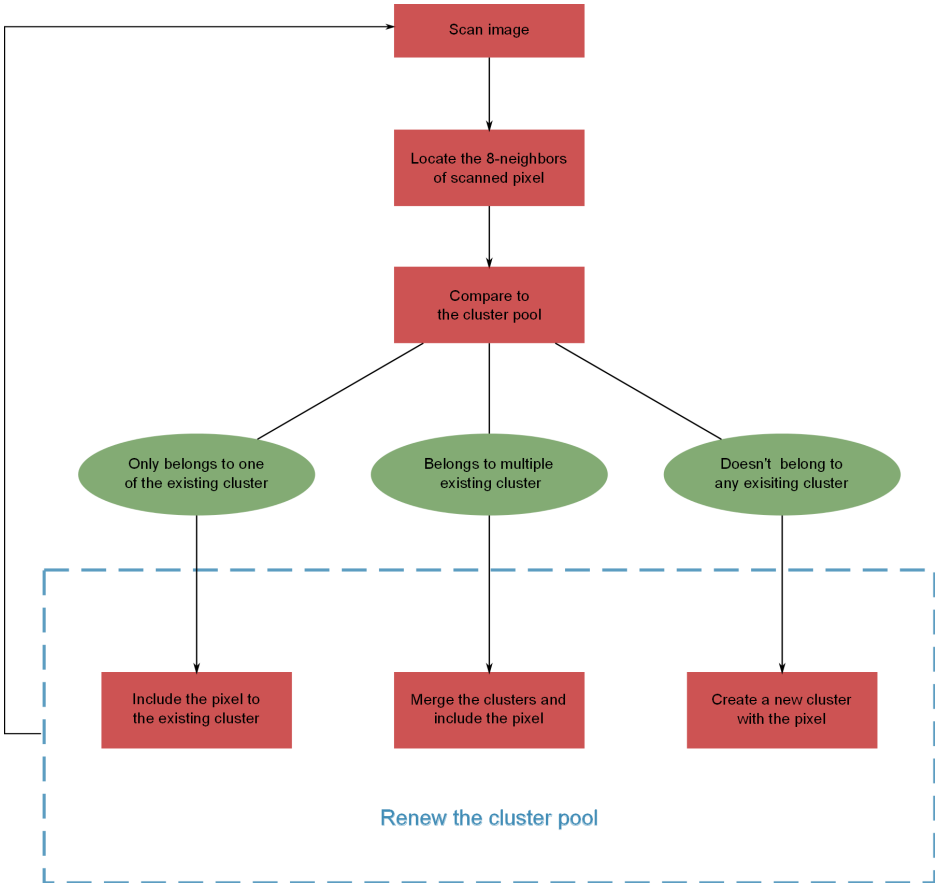

Figure 4.7: Flow chart showing the process of grouping thresholded pixels based on the connections of each pixel to its neighbours

and has been validated experimentally in Section 7.3.3. However, as will be discussed in Section 6.3, island-clusters corresponding to a single source projection might be obtained in the threshold image, if the total number of photons counted in the image is too low. Although this situation has only been observed in simulations, a grouping method independent of the continuity of the cluster representing source projections is desirable so that this case can be safely handled.

A method for grouping pixels by comparing the distance between the pixel and the CoM of the existing cluster was developed in Matlab, which is especially well-suited to images with insufficiently high photon count to achieve a contiguous cluster corresponding to a single source projection. The proposed method is described in Figure 4.8. Pixels are grouped in a cluster if the distance from a pixel to the CoM of existing clusters is smaller than a predefined length (l_D), which corresponds to the maximum possible radius of the projection. The number and size of the clusters increasing as each pixel in the image is scanned. The CoMs are recalculated after every new pixel is evaluated, and the next evaluated pixel will be compared to the renewed CoMs. Although this pixels grouping method based on their distance to the existing CoMs can successfully select source projections even when the projection is discrete, its application is limited by the size of the projection and the spacing between the projections; specificlly:

- l_D must to be greater than the maximum possible radius of the largest possible projection. Failure to maintain this limitation will lead to multiple clusters grouped in the region of a single source projection; and
- The minimum distance between the pixels in different clusters must be larger than l_D. Failure to maintain this limitation will lead to overlapping clusters containing pixels from different source projections.

It is obvious from above limitations that this method is only effective when $\forall d_{CoMs} >$

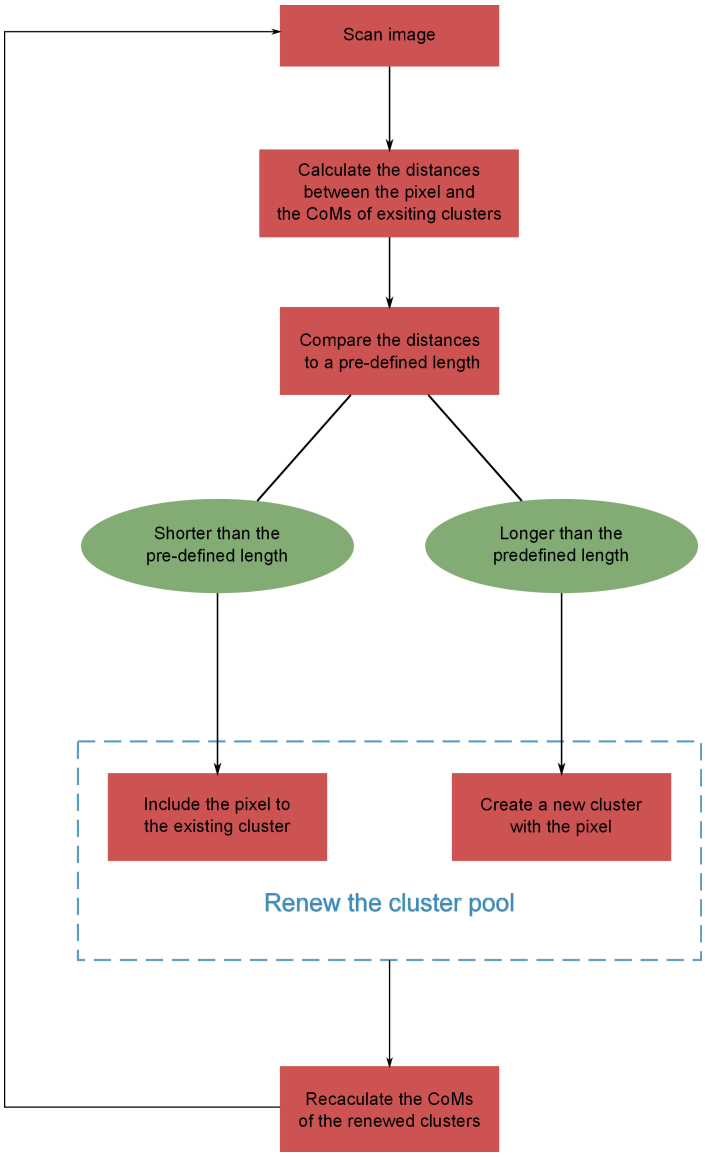

Figure 4.8: Flow chart showing the process by which thresholded pixels are grouped based on the their distance to the CoM of an existing cluster

$3 \times r_{max}$, where d_{CoMs} is the distance between the CoMs and r_{max} is the maximum radius of the projections. As discussed in Section 4.2.1, the size of each cluster can be controlled by adjusting the threshold. The distance between the CoMs depends on the distance between pinhole centres (d_{pinh}), the height of source from the pinhole centres (h_{sp}) and the distance between the pinhole centres and the detector (h_{pd}), which can be expressed as:

$$d_{CoMs} = d_{pinh} \times (\frac{h_{pd} + h_{sp}}{h_{sp}}) \tag{4.7}$$

d_{CoMs} reduces with the increasing source height and approaches d_{pinh} when d_{sp} is much bigger than d_{pd}. Since the distance between two nearby pinholes is 6.5 mm, a source projection radius smaller than 2.17 mm (corresponding to approximately 40 pixels) is appropriate for the application of above grouping method.

4.2.3 Calculating the Centre of the Projection

After constructing the clusters of the pixels corresponding to each projection, the position of the CoM of each projection (P_{CoM}) is calculated by averaging the coordinates of the pixels in each projection weighted by their pixel value ($C_{(i,j)}$):

$$P_{CoM} = \sum_{Proj} (i, j) \cdot C_{(i,j)} \tag{4.8}$$

By removing the weighting term $C_{(i,j)}$, the position of the *geometric centre of the projection* (P_{CoG}) can also be calculated. P_{CoG} can predict the centre of the projection more accurately (compared to P_{CoM} with CoM_i as a reference) in some case, e.g. when pixels or regions within the selected projection were masked and interpolated. However, using P_{CoG} will discard a great deal of useful information, since the actual counts in the pixels are ignored. The full process, including grouping

and the calculation of CoM, is accomplished by a function (`BV_MultiCentroid()`) developed in Matlab, which also outputs P_{CoG}, d_{CoMs} and an estimate of the number of projections.

4.3 Localisation of the Source Position in the Treatment Volume

Having determined the CoMs of the projections, each CoM is associated with a pinhole to determine the LCPs. Without pre-knowledge of source position, the combination of CoMs and pinholes could be ambiguous, since for many source positions there will be less than seven visible projections. Thus, a method to choose the correct assignment of projections to pinholes is required in order to determine the real source position. In this section, the mapping of projection CoMs to pinholes is introduced in subsection 4.3.1 and the final calculation of the source position within the treatment volume is described in subsection 4.3.2.

4.3.1 Selection of Projection Pinhole Combination

The CoMs of the projections will be approximately collinear and lie on a line on the detector plane which is parallel to the row of pinholes. Since the lines drawn from the CoMs to their (true) corresponding pinholes should never intersect between the collimator and the detector, the order of projection CoMs in y will be the same as the order of the pinholes through which the lines to the source must be projected. Therefore, for the case where the number of identified projections (N_{proj}) is identical to the number of pinholes (N_{pinh}) (i.e., seven, for the current design of *HDR BrachyView*), then there is only one possible combination of CoMs and pinholes. This is normally the case when the source is far away from the collimator and located in the FoV of all

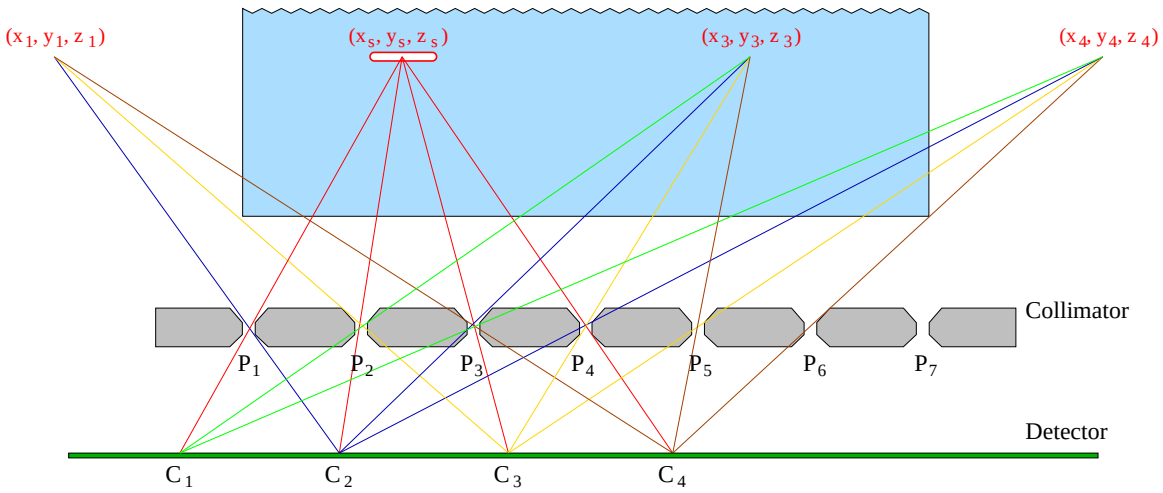

Figure 4.9: Example source location with four projections visible, illustrating the ambiguity of the estimated source location; the ambiguity is resolved by considering the relative intensity of the projections.

the pinholes. However, when the catheter is placed close to the collimator, the target area is not covered by the FOV of all the pinholes. In this case, N_{proj} is likely to be less than N_{pinh}. The collimator placement has been deliberately chosen such that all potential source locations within the treatment volume are covered by the FoVs of at least two pinholes, and will therefore result in at least two projections of the source on the detector (i.e. $2 \leq N_{proj} \leq N_{pinh}$). Thus, there will be $N_{pinh} - N_{proj} + 1$ possible sets of consecutive pinholes through which the source may have been projected onto the detector. Each of these sets results in a different potential source position. An example where $N_{proj} = 4$ is illustrated in Figure 4.9.

This ambiguity can be resolved by considering the relative intensity of each source projections. The intensity of the source projections will not be the same, due to the inverse square law; the brightest projections will be those at the minimum distance from the source. Therefore, either the brightest projection may be associated with its nearest pinhole, or the centre of mass of the overall image field can be used to determine which of the $N_{pinh} - N_{proj} + 1$ possible sets of consecutive pinholes the projections have actually passed through. This will uniquely identify the location of

the source. Therefore, for the case where $N_{proj} < N_{pinh}$, potential source positions are calculated with all the possible combination of CoMs and pinholes. Then, the real source position is selected by comparing the potential positions to the CoM of the whole image.

4.3.2 Final Calculation of the Source Position Within the Treatment Volume

As discussed in the beginning of this chapter, the source centre is defined as the point of intersection (or the best least-squares fit if the lines do not precisely intersect) of all the 3D lines joining visible projections to pinholes. Let the simultaneous equations of the ith line be:

$$\begin{cases} A_{i1} \cdot P + B_{i1} = 0 \\ A_{i2} \cdot P + B_{i2} = 0 \end{cases} \tag{4.9}$$

where A_{i1} and A_{i2} are the normal vectors of the two planes defined by the $i1$th and $i2$th line, and P represents any point on the line. Thus, for a set of N_{proj} projected lines, the coordinates of the source centre P_s are the solution of the following simultaneous equations:

$$\begin{cases} A_{11} \cdot P_s + B_{11} = 0 \\ A_{12} \cdot P_s + B_{12} = 0 \\ \qquad\qquad \cdots\cdots \\ A_{N_{proj}1} \cdot P_s + B_{N_{proj}1} = 0 \\ A_{N_{proj}2} \cdot P_s + B_{N_{proj}2} = 0 \end{cases} \tag{4.10}$$

Usually, the number of equations in this system is larger than the dimensions of P_s (i.e. $N_{proj}2 \geq 2$). In this case, P_s can be calculated as the least-squares solution

of the simultaneous equations, either using a Penrose-Moore pseudoinverse matrix or via an iterative gradient-descent method such as the Nelder-Mead simplex algorithm implemented via the Matlab function `fminsearch()` [163, 164]. In either case, the result is the point P_s which is the minimum total distance to all of the projected lines; the gradient-descent method is currently used in the Matlab software developed for *HDR BrachyView* , but the pseudoinverse method can easily be substituted.

4.4 Conclusion

In this Chapter, the source tracking process used by *HDR BrachyView* was discussed. The source position is determined by finding the centres of mass (CoMs) of source projections on an imaging plane and then back-projecting these points through the corresponding pinholes to obtain an estimate of the three dimensional source position. Several alternative methods for image segmentation for automatic CoM identification were discussed, and a simple adaptive two-step thresholding method adopted. A novel post-reconstruction projection selection method was developed to solve the problem of multiple projection-pinhole combinations to obtain a unique solution for the source position.

Chapter 5

Effect of Dose Backscatter from *HDR BrachyView* Probe on Rectum Dose Distribution

5.1 Introduction

In the previous chapters, the design of *HDR BrachyView* probe and the principle of source tracking were explained in detail. In summary the *HDR BrachyView* probe consists of an imaging plane (a 14 mm $\times$ 60 mm pixelated silicon detector) encased within a half-cylindrical multi-pinhole tungsten collimator. Tungsten was selected as the collimator material due to its high density and high atomic mass, which result in good collimation despite the volumetric constraints of the probe. However, photons emitted by the source incident on the collimator surface generate backscattered secondary electrons, resulting in an enhancement in the dose delivered immediately adjacent to the collimator surface [165, 166, 167]. Thus, a potental concern with the *HDR BrachyView* project is that increased tissue damage to the anterior wall of the rectum may result due to its proximity to the collimator, depending on the range of

these secondary electrons. To date, little work has been done to evaluate the dose enhancement due to backscatter specifically from *tungsten* inserts, particularly for the range of photon energies used in HDR PBT, as tungsten and tungsten alloys are rarely used for permanent medical implants.

Substantial work exists on backscatter radiation in specific medical applications, primarily related to the consequences of the irradiation of permanent metallic implants used in dental prostheses and bone repairs. Radiation mucositis has been observed in tissue immediately adjacent to regions with high electron density (such as gold crowns, amalgam fillings and mandibular reconstructions) in patients treated with therapeutic radiation in the head and neck region [165, 168]. Regulla et al. have exposed single layers of mouse embryonic fibroblasts in contact with a thin metallic gold foil and enclosed within a tissue equivalent polymethylmethacrylate (PMMA) phantom to heavily filtered X-ray beams with mean effective energies of 40 to 100 keV [165]. Radiation dose and cell survival curves were compared to those obtained from irradiation of cells held between two PMMA control plates. An increase of 55% to 114% in dose was measured within the $\approx$100 μm airgap formed between the gold surface and the detector (a 0.1 μm thick Beryllium oxide (BeO) layer deposited on a thermally stimulated exoelectron emission (TSSE) substrate). The biological effect of this dose increase was different due to the higher LET of the backscattered low energy electrons; survival curves of the irradiated cells which were in contact with gold lack the pronounced shoulder observed at lower doses and resemble those of cells irradiated with high LET radiation.

Castillo et al. have reported a 17% increase in dose on the entrance side of a stainless steel mandibular implant for a 6 MeV photon beam [168]. Farahani et al. have measured the absorbed dose in a tissue equivalent polymer phantom adjacent to various dental restoration materials including 18 carat gold alloy, a silver-mercury

dental amalgam, nickel-chromium dental casting alloy and a human tooth tissue, using GafChromic films [169]. Results demonstrate an increase in the absorbed dose of up to a 100% in tissue on the backscatter side of the gold insert and up to 20% adjacent to tooth tissue when irradiated by a collimated ^{60}Co beam. Niroomand-Rad et al. have reported an increase in dose of 22.5% and 20% for 6 and 18 MeV photon beams at tissue-titanium dental interface in head and neck cancer patients [170]. Ravikumar et al. have measured the change in the backscattered dose as a function of the photon energy and the width and thickness of the inhomogeneity by placing aluminium, steel, cadmium and lead implants of varying thickness within a tissue equivalent phantom, irradiated by ^{60}Co gamma rays and 6 MV and 18 MV photon beams [171]. The measured backscattered dose was greater with lower energy photons (1.17 MeV and 1.33 MeV photons emitted by ^{60}Co) for all metallic implants. Chin et al. have conducted Monte Carlo simulations studying backscatter effects of various configurations of dental work, demonstrating an increase of up to 33% in the absorbed dose in patients with metallic dentures undergoing radiotherapy [172]. Their results indicate that the backscatter dose is completely absorbed within the first 3 to 5 mm of water-equivalent material.

In this Chapter, the results of experimental and simulation work to study the additional dose deposited by backscatter from the *HDR BrachyView* transrectal tungsten probe in response to radiation from an ^{192}Ir HDR source are presented. Backscatter dose enhancement is quantified using the *backscatter dose correction factor* (BSDF), first introduced by Das et al., which measures the dose enhancement effect of backscatter resulting from radiation incident on the interface between a low-Z region (such as human tissue) and high-Z region (such as a metallic surface) [173, 174].

An initial simulation of a planar tungsten collimator inside a water-equivalent phantom was conducted, and the BSDF calculated for two source positions as a func-

tion of distance x from the interface. The simulation was validated using an identical experimental configuration for several different values of x. Finally, a second simulation was performed using identical methodology with an accurate model of the actual cylindrical probe used in the *HDR BrachyView* design; BSDF was again calculated at a variety of locations around the collimator.

This chapter is divided into four main sections. Design of the simulation and experimental models are discussed in Section 5.2; specific simulation configurations for two collimators (planar and cylindrical) are presented in Section 5.2.1 and 5.2.2 respectively, while experimental validation of the planar simulation results are presented in Section 5.2.1.1. Results of the simulations and experimental work are presented in 5.3; the implications of these are discussed in detail in Section 5.4. An evaluation of the change in the dose distribution by the *HDR BrachyView* probe is given in Section 5.5.

5.2 Materials and Methods

All simulations and experiments described in this section use the backscatter dose correction factor (BSDF) to quantify dose enhancement. BSDF is defined as the ratio of the dose measured within a homogeneous tissue equivalent volume with and without the presence of a high electron density region (D_i and D_h respectively):

$$BSDF(E, A, w, d, t, x, Z, \Theta) = \frac{D_i}{D_h} \tag{5.1}$$

where E is the energy of the photon beam, A is cross-sectional area of the field at the point of measurement, t and w are the thickness and the width of the high-Z region, d is the distance between the top surface of the high-Z region and the top surface of the low-Z region, x is the distance between the point of measurement and

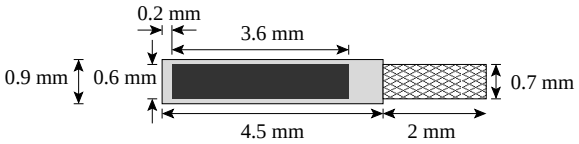

Figure 5.1: The simulated ^{192}Ir HDR brachytherapy source. The core consists of pure iridium with a uniform distribution of ^{192}Ir, surrounded by a steel shell [175].

the top surface of the high-Z region and Θ is the photon beam angle of incidence [173, 174].

Two probe geometries (planar and cylindrical) and an ^{192}Ir HDR brachytherapy source were simulated using the Geant4 tool-kit. The source model used throughout the simulations was based on a Nucletron microSelectron HDR ^{192}Ir source, as shown in Figure 5.1 [175, 156]. The core consists of a pure iridium metal cylinder (3.6 mm long and 0.6 mm in diameter) with ^{192}Ir uniformly distributed through its core volume, surrounded by a steel shell (4.5 mm in length with an outer diameter of 0.9 mm), connected to a short steel wire (2 mm long and and 0.7 mm in diameter). Primary particles were generated using Geant4 Radioactive Decay Module (G4RadioactiveDecay). The Geant4 Low Energy package (G4LowEnergy package), using the Livermore Evaluated Data Libraries was employed to model low energy interactions.

5.2.1 Planar Tungsten Collimator

5.2.1.1 Experimental Configuration

The experiments were conducted at the HDR brachytherapy facilities at the St. George Hospital Cancer Care Centre, Kogorah. The experimental configuration is illustrated in Figure 5.2. A series of 90 mm×90 mm Computerized Imaging Reference Systems (CIRS) Plastic Water sheets, each with a thickness of either 3 mm, 5 mm or 10 mm, were stacked to construct a 90 mm×90 mm×100 mm tissue equivalent phantom. A 120 mm×50 mm×4 mm collimator, fabricated from a tungsten alloy (95% W, 3.5% Ni

and 1.5% Cu) was placed immediately below the phantom; in turn, it was supported by a further 90 mm×90 mm×20 mm slab of Plastic Water. For dose measurements performed in the absence of the tungsten collimator, the tissue-equivalent phantom block was simply placed directly on top of the final Plastic Water slab. One of the 10 mm sheets in the phantom assembly included a hole for the insertion of a catheter into which the HDR brachytherapy source is inserted by an afterloader mechanism; re-arrangement of the Plastic Water sheets allow the source to be placed either 20 mm or 43 mm from the top surface of the collimator.

For each source position, a Nucletron microSelectron HDR afterloader remotely inserted a microSelectron ^{192}Ir source into the tip of the catheter. Source dwell times were calculated to be equivalent to a 370 GBq (10 Ci) source being positioned for 10 s and 50 s at distances of 20 mm and 43 mm from the top surface of the tungsten collimator respectively. Dose was measured at $x = 0$ mm, 5 mm and 10 mm from the top surface of the tungsten collimator, using a pre-calibrated MO*Skin*™ detector. This detector is a MOSFET based detector designed at CMRP with a sensitive volume thickness of ≤ 1 μm, with high reproducibility between devices from the same batch (coefficient of dispersion of 2.5%, measured using an ^{192}Ir HDR brachytherapy source) and a linear response up to a maximum threshold voltage of 24 V (corresponding to an accumulated dose of approximately 70 Gy) [134, 176, 135]. For each dose measurement, the detector was placed within a shallow groove, etched on the central axis of the surface of a 90 mm×90 mm×5 mm Plastic Water sheet and spanning half its length. This allowed the MO*Skin* detector to be positioned directly beneath the ^{192}Ir source at a precise distance from the top surface of the tungsten collimator. The source was remotely moved into position for the desired dwell time by the afterloader, after which it was retracted and safely stowed. The MO*Skin* threshold voltage was recorded thirty seconds after each irradiation by the CMRP digital MOSFET readout system.

It is anticipated that there will be a very high rate of change in the backscatter dose near the surface of the collimator. Therefore, the actual point inside the MO*Skin* detector at which the dose is measured needs to be considered. The geometry and composition of the MO*Skin* detector employed in measuring the dose is such that its effective water-equivalent depth (WED) is approximately 70 μm from its front face [176]. Therefore, when placed in direct contact with the collimator's surface, the dose measurement will actually be performed at a distance of 70 μm rather than zero. Similarly, 70 μm must be added to x for each additional measurement.

For each source position, the dose measurement procedure was repeated three times at each collimator-sensor distance, with and without the tungsten collimator in place. The change in the threshold voltage was calculated and converted to dose values for each source position. The BSDF was then calculated as the ratio of the calculated dose delivered with and without the tungsten collimator present.

5.2.1.2 Monte Carlo Simulations

Models of a 90 mm×90 mm×200 mm water phantom representing soft tissue with and without a 90 mm×50 mm×4 mm rectangular tungsten plate (representing the *HDR BrachyView* collimator) placed at the geometric centre were developed in Geant4. A 1 mm×1 mm×10 mm column of water directly above the centre of the top face of the collimator was quantised into one hundred 1 mm×1 mm×0.1 mm rectangular scoring voxels. One billion primary particles of ^{192}Ir were generated with the source model placed 20 mm above the centre of the top face of the collimator. A second source position, 43 mm above the centre of the top face of the collimator, was also simulated with four billion primary particles. The simulation was performed for each source position, firstly with the tungsten collimator inside the water phantom and secondly with the collimator replaced by the same volume of water. The ratio of dose recorded in each scoring voxel with and without the collimator present was calculated

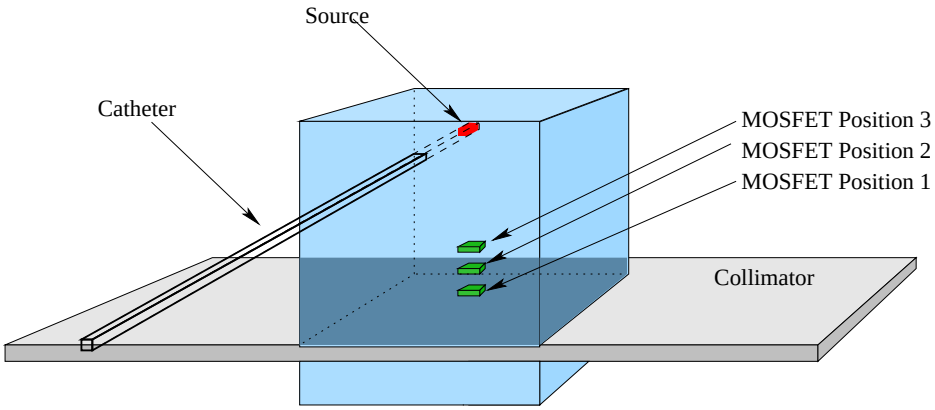

(a) With planar tungsten collimator

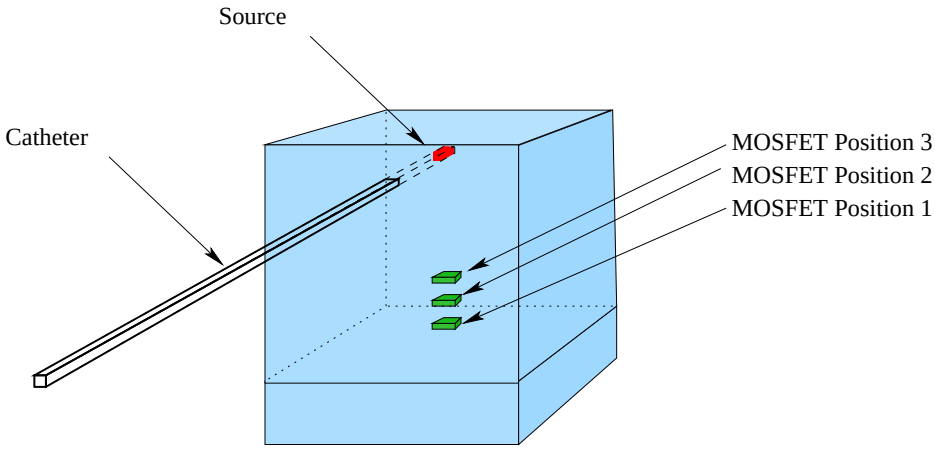

(b) Without planar tungsten collimator

Figure 5.2: The experimental configuration; measurements were made at three different points (front face of MO*Skin* detector placed 0, 5 and 10 mm above the surface of the tungsten collimator) for two different source positions (20 mm and 43 mm above the surface of the collimator). The measurements were then repeated after the removal of the collimator.

to determine the BSDF for the two source positions as a function of distance x from the centre of the front face of the collimator.

Considering the Mo*Skin* detector used in experiment has a sensitive volume thickness of $\leq$ 1 μm and a WED of approximately 70 μm, additional simulations with sensitive volume thickness of 1 μm measuring the dose change within 1 mm above the collimator is ideal to compare with the measurement from the Mo*Skin* flush to the collimator. However this is not feasible. The cut range of the simulation is 1 μm and the thickness of sensitive volume should be at least 10 times of the cut range for accurate measurement. Also a simulation with such a small sensitive volume is unacceptably time consuming. To get a closer comparison with the Mo*Skin* flush to the collimator, additional simulations with sensitive volumes thickness of 10 μm (a hundred voxels covering 1 mm above the collimator) were built to compare with the measurement from the Mo*Skin* flush to the collimator.

5.2.2 Cylindrical Tungsten Collimator

The dose enhancement effect of the cylindrical tungsten collimator on the surrounding tissue was evaluated by performing Geant4 simulations with and without the probe in a water phantom. The collimator was modelled as a 100 mm long half-cylindrical tungsten shell with an inner radius of 8 mm and an outer radius of 12 mm. This was placed at the centre of a 300 mm $\times$ 300 mm $\times$ 300 mm cubic water phantom. The simulation model is illustrated in Figure 5.3. The sensitive volume used to evaluate the dose was constructed by quantising the volume of water surrounding the probe into scoring voxels with a cylindrical coordinate system. The sensitive volume extends 41 mm along the axis of the collimator ($y \in \{-20, -19, \ldots, 19, 20\}$ mm), divided into 41 1 mm slices; from 12 mm to 22 mm radially (along the r axis), divided into 101 concentric annular rings ($r \in \{12.05, 12.15, \ldots, 21.95, 22.05\}$ mm), and spans 170° in the

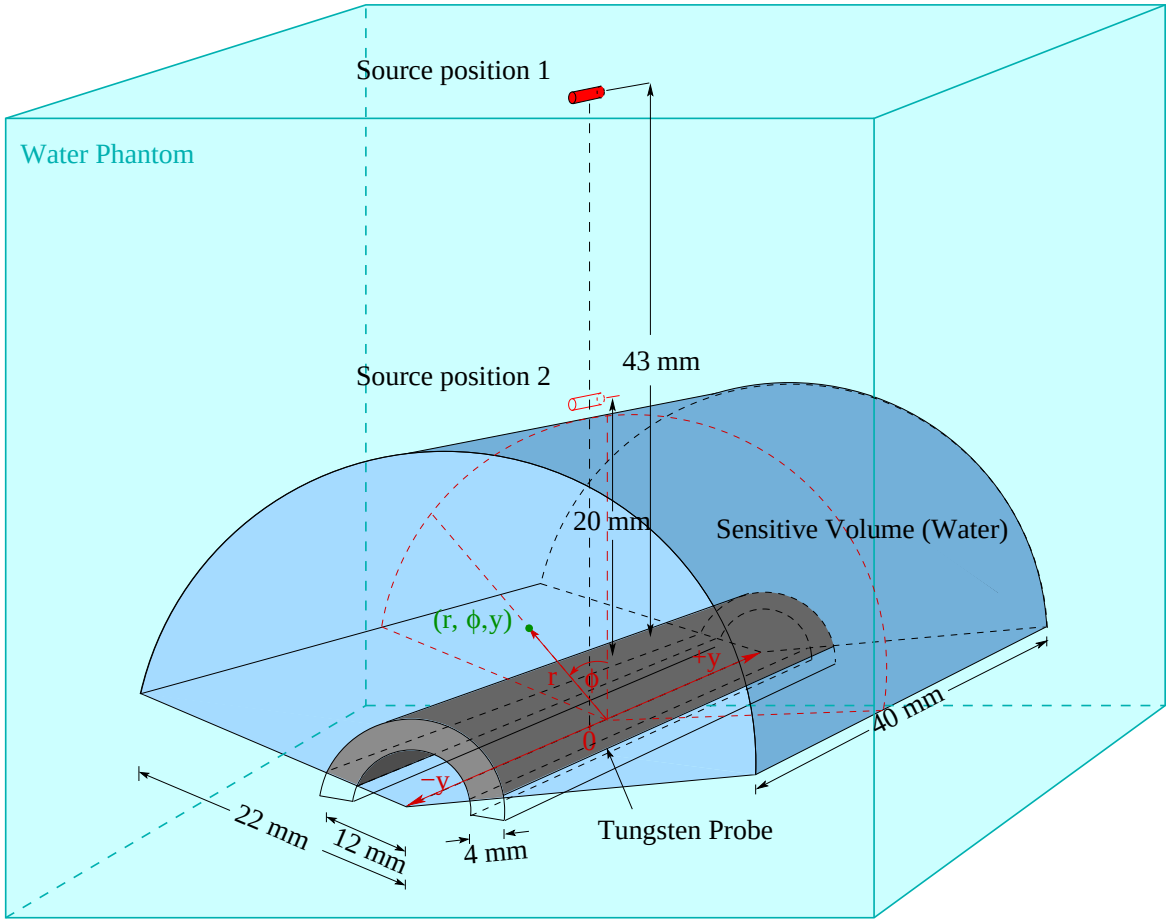

Figure 5.3: The simulated cylindrical probe, surrounded by the tissue equivalent sensitive volume, which is divided into scoring voxels in a cylindrical coordinate system.

azimuth divided into 17 10° sectors ($\phi \in \{-80°, -70°, \ldots, +70°, +80°\}$). Therefore, the dose is calculated for $41 \times 17 \times 101 = 70397$ voxels, where each voxel is addressed by its displacement along the collimator's axis (y), the azimuth of its sector (ϕ) and its radial distance from the probe axis (r). Again, BSDF is calculated as the ratio of the dose measured in each scoring voxel with and without the collimator present.

5.3 Results

The following sections detail the simulation results for both types of collimator, together with experimental validation of the results for the planar collimator. All errors

quoted or illustrated on graphs correspond to three standard deviations (99% confidence intervals). d_{SC} denotes the distance between the source and the centre of the top surface of the planar collimator or the highest point of the cylindrical collimator; x denotes the distance from the top surface of the collimator to the point at which dose is measured.

5.3.1 Planar Tungsten Collimator

5.3.1.1 Monte Carlo Simulations

The BSDF values calculated for the two simulated source positions with and without the planar tungsten collimator (described in Section 5.2.1.2) are plotted as a function of distance x from the top surface of the collimator in Figure 5.4. For both source positions, the BSDF approaches unity beyond a distance of 0.5 mm from the collimator. The largest BSDF occurs near the surface of the tungsten collimator. As shown in Figure 5.4(a) and Figure 5.4(b) the average BSDFs within 0.1 mm are 2.55±0.22 and 2.68±0.27 recorded for the source placed at 20 mm and 43 mm above the top surface of the tungsten collimator respectively. Figure 5.4(c) and Figure 5.4(d) show a steep BSDF gradient within 500 μm with a step of 10 μm. According to the plots, a larger maximum BSDF and steeper BSDF gradient is obtained when the source placed at 43 mm above the top surface of the collimator. The BSDFs in sensitive volume 70 μm above the collimator are 1.81±0.40 and 1.91±0.31 recorded for the source placed at 20 mm and 43 mm above the collimator respectively.

5.3.1.2 Experimental Validation

The BSDFs experimentally measured using the MO*Skin* detector are shown in Table 5.1.

The results are essentially identical for both source positions. The increase of dose

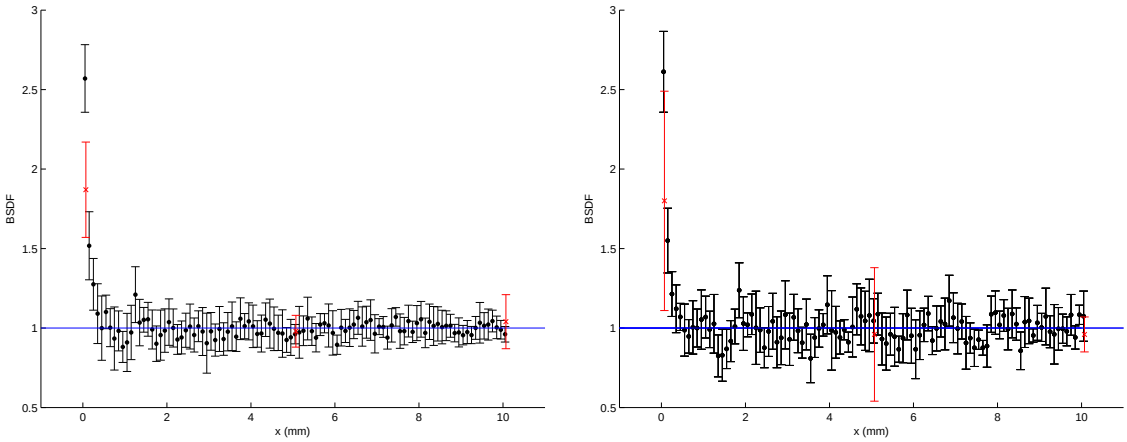

(a) $\phi = 0°$, $y = 0$ mm, $d_{SC} = 20$ mm

(b) $\phi = 0°$, y=0 mm, $d_{SC} = 43$ mm

(c) $\phi = 0°$, y=0 mm, $d_{SC} = 20$ mm

(d) $\phi = 0°$, y=0 mm, $d_{SC} = 43$ mm

Figure 5.4: The backscatter dose fraction (BSDF) calculated for two source positions simulated above a 4 mm thick planar tungsten collimator. The calculated BSDFs approach a value of 1 beyond a distance of 0.5 mm from the top surface of the tungsten collimator.The MOSkin measurement is demonstrated as the red marker

			BSDF	
	Detector face depth (mm)	Sensitive depth (mm)	d_{SC} = 20 mm	d_{SC} = 43 mm
x	0	0.07	1.87 ± 0.30	1.80 ± 0.69
	5	5.07	0.98 ± 0.10	0.96 ± 0.42
	10	10.07	1.04 ± 0.17	0.96 ± 0.11

Table 5.1: BSDF measured using MO*Skin* detector.

due to the presence of the tungsten plate is only observed in the measurement where the MO*Skin* is flush to the top surface of tungsten collimator.

5.3.2 Cylindrical Tungsten Collimator

Figure 5.5 shows the BSDF as a function of distance from the top of the cylindrical collimator ($\phi = 0°$, $y = 0$ mm). As distance from the cylindrical collimator increases, the behaviour of the BSDF is similar to that exhibited in the simulation of the planar tungsten collimator. Figure 5.6(c) and 5.6(d) show that BSDF around the tungsten collimator is essentially independent of axial displacement for all values of r.

Figure 5.6(a) indicates that when the source is 20 mm from the collimator, the BSDF is almost independent of $|\phi|$ when $|\phi| \leq 60°$ with a peak value of 2.4, falling sharply to unity when $60° < |\phi| < 80°$ for radial distance of 12.05 mm. For larger values of r, the falls in BSDF still occur at a similar angular threshold but are less pronounced: while the maximum BSDF is 2.4 for $r = 12.05$ mm, the BSDF remains essentially constant with respect to ϕ for all values of r and is close to unity for $r = 12.45$ mm. There are two factors which are responsible for the BSDF being less than one for $|\phi| = 80°$: firstly, at high angles of photon incidence, the backscattered electrons will also be emitted at a very high angle (i.e. almost tangentially to the collimator surface), leading to a very small backscatter dose immediately above the surface; and secondly, incident photons are partially attenuated by passing through the

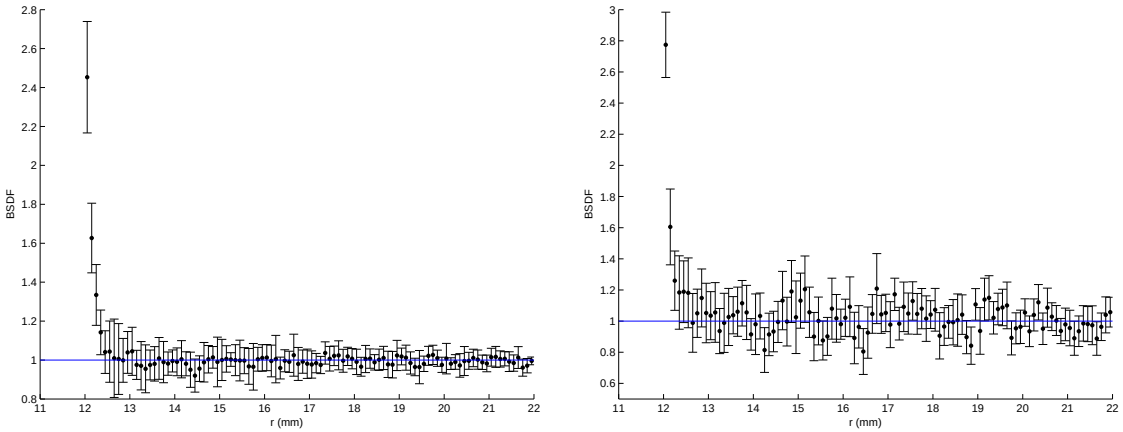

(a) $\phi = 0°$, $y = 0$ mm, $d_{SC} = 20$ mm (b) $\phi = 0°$, $y = 0$ mm, $d_{SC} = 43$ mm

Figure 5.5: BSDF directly above the centre of the simulated cylindrical tungsten collimator as a function of r ($y = 0$ mm and $\phi = 0°$) for two source positions.

wall of the collimator, reducing the direct dose in comparison to the water phantom.

A similar trend is observed in the plotted BSDF values in Figure 5.6(b), where the source is placed 43 mm above the cylindrical collimator, demonstrating a sharp reduction in with increasing the radial distance. Larger BSDF values are observed in comparison to the previous case for tangential incidence of radiation ($|\phi| = 80°$) which is mostly due to the reduced angle of incidence for secondary electrons and hence their effective back scattering in contrast to the 20 mm source-surface distance.

Heatmap surfaces illustrating BSDF as a function of y and ϕ for $r = 12.05, 12.55$ and 13.05 mm are shown in Figure 5.7. For each value of r, the BSDF remains nearly constant with respect to the y axis, and its minimum value occurs when $|\phi| > 80°$.

5.4 Discussion

The simulations indicate that although there is significant dose enhancement in the vicinity of the tungsten-phantom interface, BSDF rapidly declines to unity (that is, no measurable backscatter dose enhancement) within a distance of less than 1 mm from the collimator surface, both for planar and cylindrical tungsten collimator. For

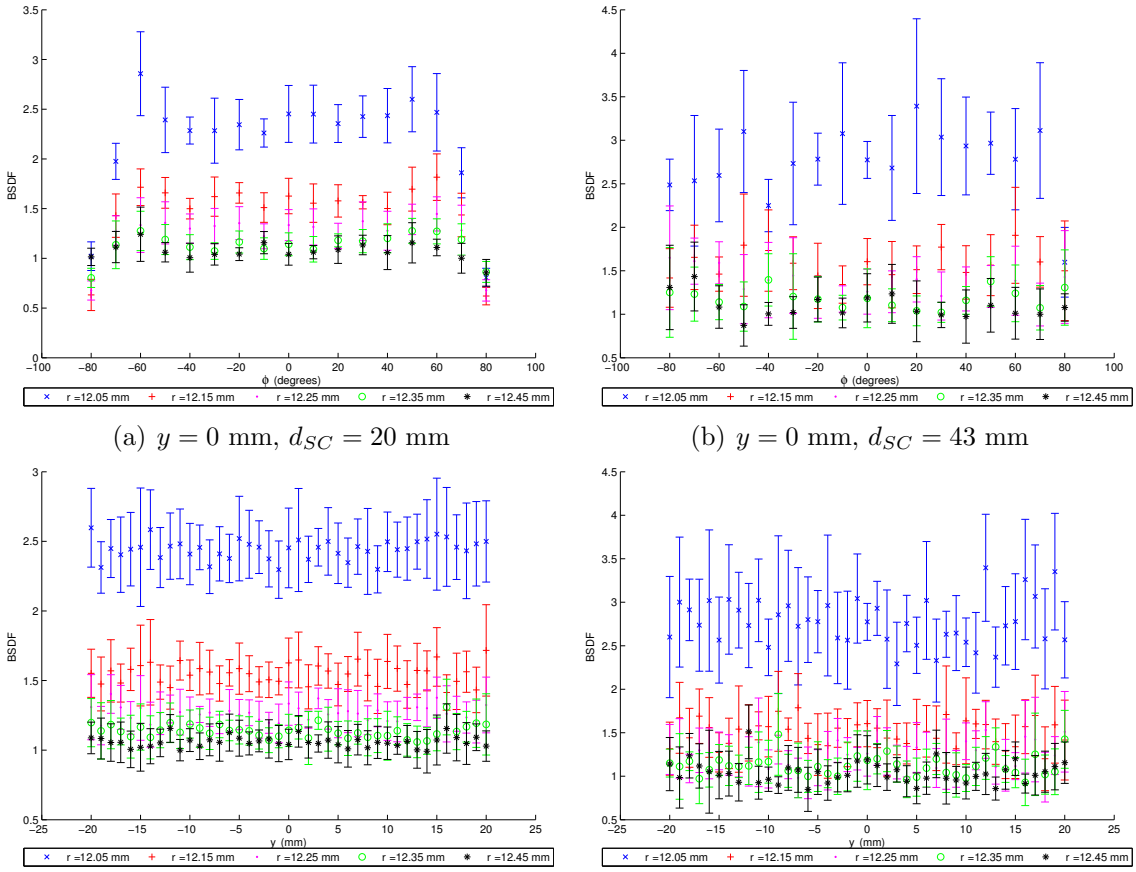

(a) $y = 0$ mm, $d_{SC} = 20$ mm

(b) $y = 0$ mm, $d_{SC} = 43$ mm

(c) $\phi = 0°$, $d_{SC} = 20$ mm

(d) $\phi = 0°$, $d_{SC} = 43$ mm

Figure 5.6: BSDF from the simulated cylindrical tungsten collimator as a function of ϕ and y, calculated for four different values of r and two source positions ($d_{SC} = 43$ mm and $d_{SC} = 20$ mm).

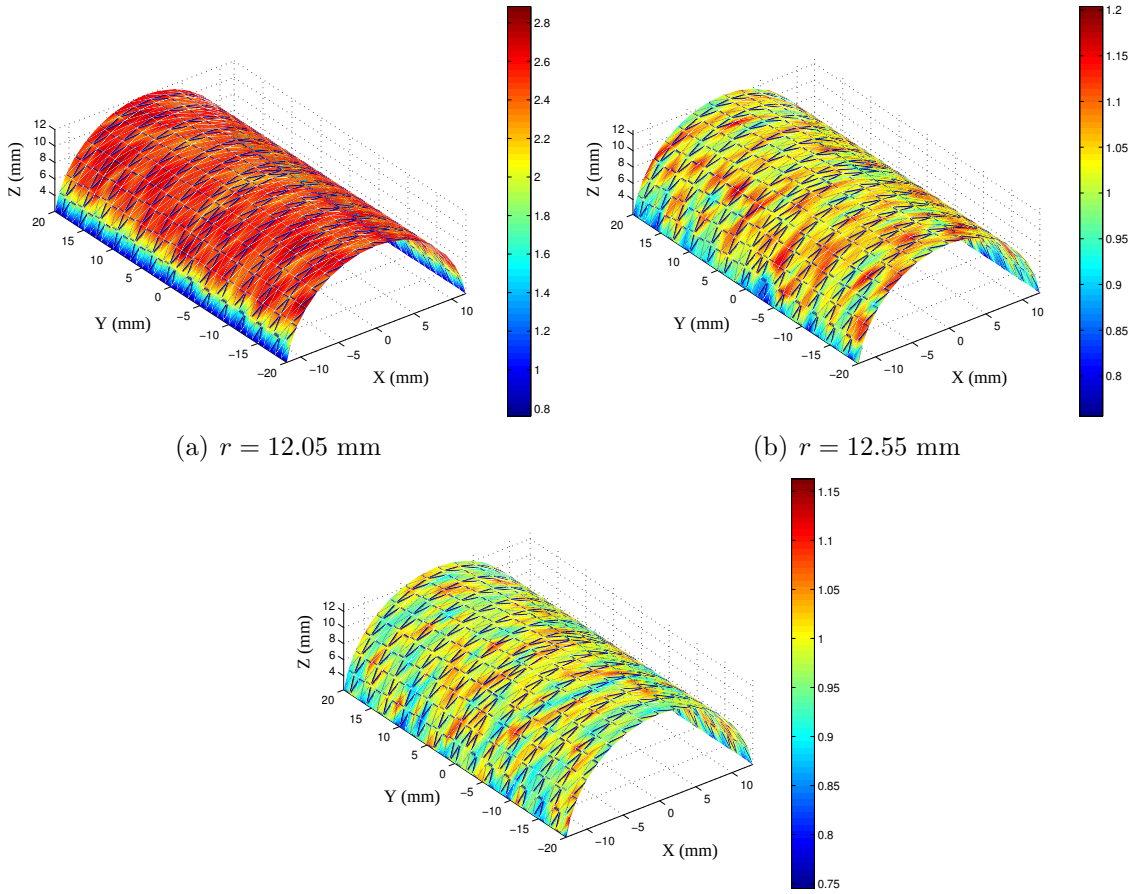

(a) $r = 12.05$ mm

(b) $r = 12.55$ mm

(c) $r = 13.05$ mm

Figure 5.7: BSDF values from the simulated cylindrical tungsten as a function of y and ϕ were computed for three values of r and are shown as heatmap surface plots in three dimensions, for the source placed at 20 mm above the collimator ($d_{SC} = 20$ mm).

the planar collimator, this result has been experimentally confirmed; at the closest practical point of measurement (equivalent to approximately 70 μm from the collimator surface) the BSDF was measured to be 1.87±0.10 and 1.80±0.23 for a source-collimator distance of 20 mm and 43 mm respectively, while the dose measurements acquired at distances of 5 mm and 10 mm from the surface of the collimator show no measurable dose enhancement at all (BSDF is very close to unity). Therefore, based on the MO*Skin* measurements it is safe to conclude that dose enhancement is insignificant 5 mm from the collimator surface in a tissue-equivalent medium, and according to the Monte Carlo simulations, is expected to be negligible beyond 1 mm from the collimator surface. In the complete *HDR BrachyView* probe design, collimator is encased in a protective 1 mm thick medical-grade sterilisable tissue-equivalent plastic shell - therefore the vast majority of the backscatter dose will be absorbed in this shell.

The result of experiment agreed well with the simulation with sensitive volume thickness of 10 μm. Since MO*Skin* detector has WED of 70 μm, the measurements of MO*Skin* flushed to the collimator are actually performed at 70 μm above the tungsten plate within a voxel thickness less than 1 μm. The result of these measurements is in good agreement with the value obtained in simulations when the sensitive volume is 70 μm away the collimator. The results obtained demonstrate the ability of the MO*Skin* dosimeter to characterise a very steep sub-millimetre dose gradient.

Although dose measured at tungsten interface is more than double the dose measured in the absence of the tungsten plate, this dose increase is limited to a very short distance (approximately 1 mm) from the interface between the tungsten collimator and the water-equivalent phantom. This is because the backscatter dose is mostly contributed by low energy secondary electrons. This result agrees with the behaviour described in studies published in 2004 and 2006 by Ravikumar et al. and Sathiyan et al. respectively[171, 177], which showed that lower incident photon energy will lead

to a shorter backscatter electron range. The lowest energy included in these studies is 1.17 MeV (^{60}Co) and a backscatter dose enhancement range of a few millimetres was obtained. Since the average energy of ^{192}Ir is around 340 keV and its spectrum contains many low energy photons which contribute to the dose, it is reasonable to expect a much shorter range of backscatter electrons, which is in agreement with the results obtained both in Monte Carlo simulations and physical experiments. Although different source-to-tungsten-interface distances will lead to variations in photon flux density, it does not have a significant effect on BSDF, since BSDF is calculated as ratio of dose in a volume with the same position relative to the source with and without the presence of the tungsten inhomogeneity. Therefore, no significant difference in BSDF was obtained when the source placed at different distances from the tungsten interface.

The result of simulation with the cylindrical tungsten collimator shows that BSDF is approximately constant with respect to displacement along the axis of the collimator (for $\phi = 0°$ and constant r), which is similar to the results seen in Ravikumar's previous study [171]. The drop in BSDF at large values of ϕ (when $y = 0$ mm and r is very small (12.05 mm and 12.15 mm)), for $d_{SC} = 20$ mm is because at these angles, the interface does not have direct line-of-sight with the source, so the photon flux reaching the surface has already been attenuated additionally to reduction of electron back-scattering explained earlier. The BSDF near the surface of tungsten is slightly greater when the source is placed 43 mm above the collimator than when 20 mm; this is due to changing angular condition of incident secondary electrons, i.e. partial reduction of the electrons travelling tangentially to the cylindrical collimator surface.

5.5 Conclusion

Experimental and simulation studies have been performed to investigate the backscatter dose introduced by the tungsten collimator in the *HDR BrachyView* project. Both Monte Carlo simulations and experiments were performed in the case of a planar tungsten collimator, while a cylindrical collimator was investigated through simulation only. Good agreement has been obtained between experiment and simulations, confirming that the patient's anterior rectal wall will not be exposed to a measurable dose increase in the vicinity of the collimator when used in the final *HDR BrachyView* design. This is because even though the dose is significantly enhanced at the surface of the collimator, the short range of the backscattered recoil electrons is such that all backscatter dose is deposited within 1 mm of the collimator surface. Since this region is occupied by a tissue-equivalent plastic shell, the patient will not receive any additional dose in the rectal wall or other tissues, confirming that the use of *HDR BrachyView* will not cause additional radiation injury to the patient, while providing real-time in vivo QA of treatment delivery.

Chapter 6

Monte Carlo Simulation Evaluation of *HDR BrachyView* Design

6.1 Introduction

The design of the *HDR BrachyView* probe has been presented in detail in Chapter 3, while Chapter 5 established that backscatter radiation from *HDR BrachyView* presents no additional hazard to the patient. In this Chapter, the position-determination capabilities of the design are evaluated through Monte-Carlo simulations. Models of tungsten collimator with single pinhole and double pinholes are established in dedicated Geant4 simulation applications. The single-pinhole model is used to perform an evaluation of detector sensitivity, estimate the contrast between the projection and the background of penetrated and scattered photons, and the evaluate accuracy of the methods proposed for localising the CoM of source projection (as discussed in Chapter 4. The models of the double pinhole are used to examine the feasibility of distinguishing between two adjacent projections and to estimate the accuracy of tracking the source position within the treatment volume.

In the following parts of this Chapter, the geometry of single and double pinhole

collimator simulations are detailed in Section 6.2.1 and 6.2.2. The results from the simulations is presented in Section 6.3 followed by a detailed discussion in Section 6.4 and a conclusive summery of the result in Section 6.5.

6.2 Simulation Methodology

The overall environment of the simulations is same as the simulation described in Section 3.4.3, including the setting of the cut value of secondary particle range, the definition of material and physics interactions (Geant4 Low Energy package, using the Livermore Evaluated Data Libraries was employed), etc. The model of HDR source used in the simulations included in this chapter is the same model described in Section 5.2. A model of 150 mm×150 mm×150 mm water phantom was established to simulate patient body. The reason of using a relative small phantom compare to the real human body is to accelerate the simulations, while the scatter of photons in the full size of human body has little effect on the pinhole imaging of *HDR BrachyView* . All simulations included in this chapter were developed in this water phantom. 10^{10} photon events were generated for each simulation (an added 10×10^9 photon events was generated for the source placed at maximum distance from the collimator to improve the statistic).

6.2.1 Single-Hole Collimator, Multiple Source Positions

The effect of source position on projection image contrast and count rate was studied by simulating a single pinhole collimator and a 14×14 mm^2 pixellated detector (equivalent to a single Timepix device) with the source positioned in different locations. The simulation configuration is illustrated in Figure 6.1, where the source is placed above the collimator; h is the distance between the source and the pinhole centre and θ is the incidence angle measured from the pinhole plane ($\theta = 90$ is normal incidence).

Eight simulations were conducted with three values of h (7 mm, 23 mm and 47 mm) and three values of θ (90°, 72°, 57°).

6.2.2 Simulation of two adjacent pinholes

A series of simulations were performed to evaluate the ability of the proposed collimator geometry to resolve the source position at its minimum distance from the face of the probe, where the ratio of *penetrated* to *direct* photons is at its maximum. A collimator with two pinholes using the same geometry as described in Section 6.2.1 with a separation of 6.5 mm (centre to centre) was simulated. The configuration is shown in Figure 6.2. The source was placed at a distance of 5 mm from the upper surface of the collimator at the midpoint of the two pinholes and parallel to the Y axis on which the pinholes lie. Ten billion photon events were simulated, and the location of the CoMs of the resulting projections through adjacent pinholes were evaluated. These were then used to estimate the source position.

To estimate the error in calculating the source position within the prostate volume (i.e. simulating an error in source position in the X-Z and Y-Z planes), a second pinhole was simulated, with the source occupying the same positions as shown in Figure 6.1. The projection images through the second pinhole were used in conjunction with those acquired in the single pinhole studies to estimate the source position within the prostate volume. The error between the estimated and actual (simulated) source position was then calculated.

6.3 Simulation Result

The projected images of the source placed in the positions described in Section 6.2.1 through the single pinhole are shown in Figure 6.3. The image intensity corresponds to the number of counts recorded in each pixel. The range of counts is shown in the

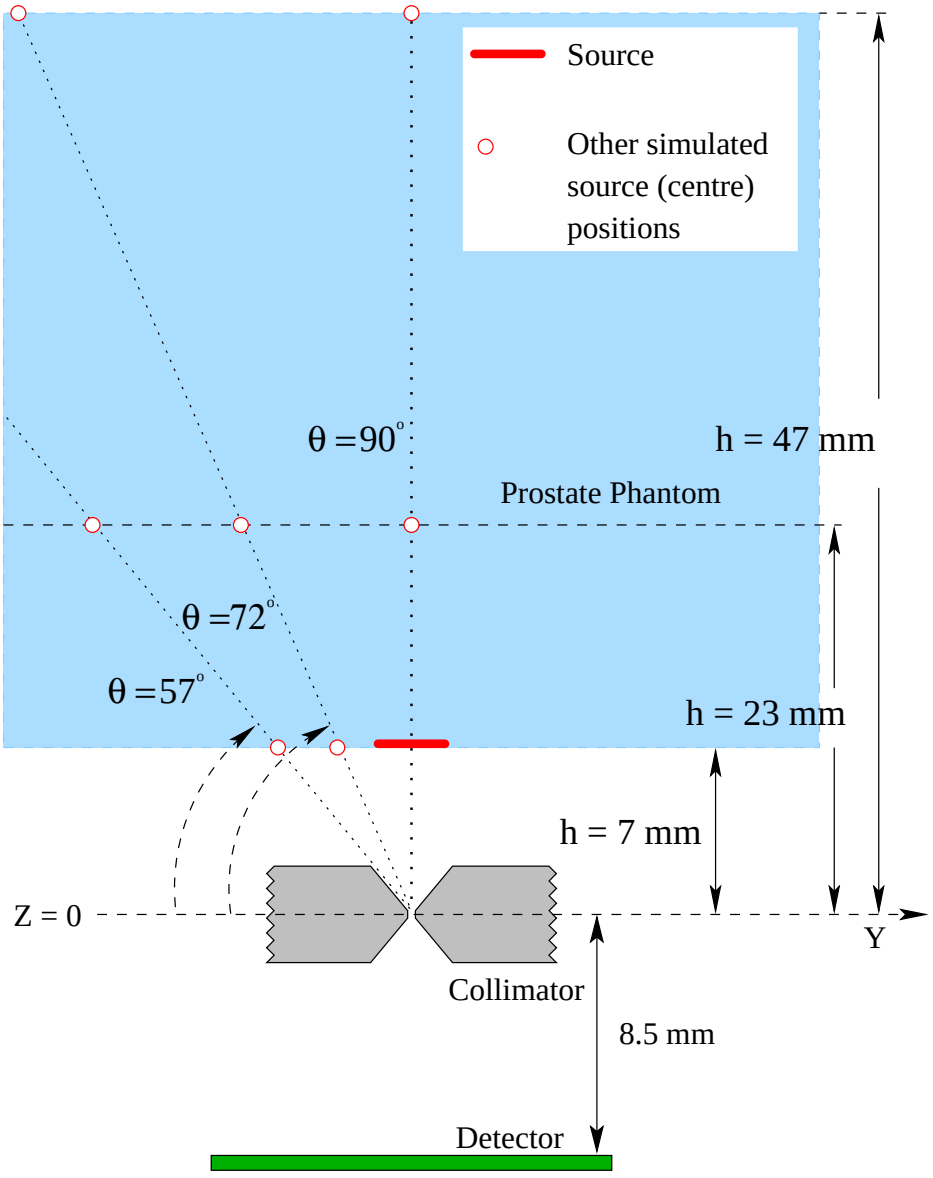

Figure 6.1: Source positions for the first group of simulations. Only one source position is occupied at any given time. The source remains parallel to the plane of the collimator throughout the procedure.

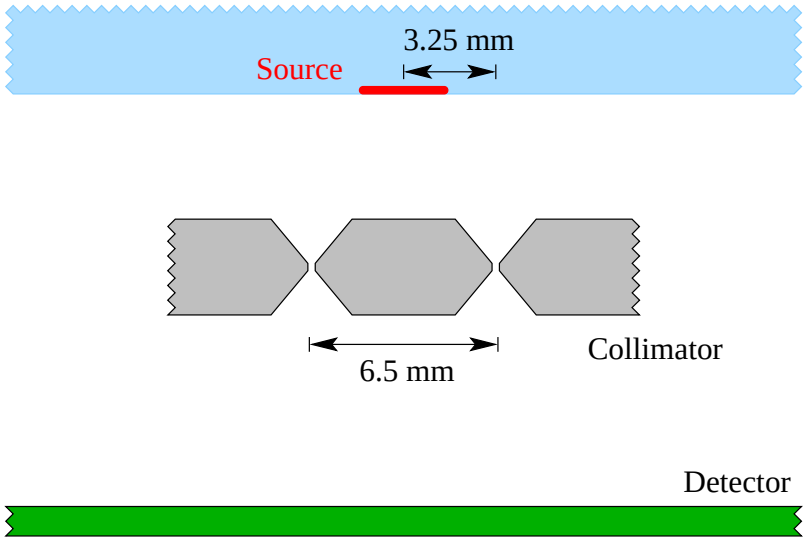

Figure 6.2: Monte Carlo simulation set up for the double pinhole study.

colour-bar adjacent to each image.

The lowest count rates occur when the source is placed at the maximum distance from the detector (Figure 6.3(h)), with a maximum of 17 counts per pixel recorded for the 20 billion photons generated by the source. While the source can be resolved in each of the simulated positions, a high background count occurs due to large number of *penetrated photons*, which contributes to a degradation in signal to background ratio (SBR). The SBR is at its minimum when the source is placed closest to the edge of FoV ($\theta = 57°$). This is as expected, since the ratio of penetrated photons to direct photons is at its maximum. The projection image corresponding to the source at this position is shown in Figure 6.3(c); although the SBR is clearly at its lowest compared to other simulated positions, the CoM of the projected image can still be accurately determined. The theoretically calculated CoM_i (corresponding to projection of the source through an infinitely attenuating collimator) and the measured positions of the CoM of source projections are marked with a `x` and a `+` respectively.

The error in estimating the location of the calculated CoM of the projected source (`+`) compared to its theoretical position (`x`) is shown in Table 6.1. The X and Y axes

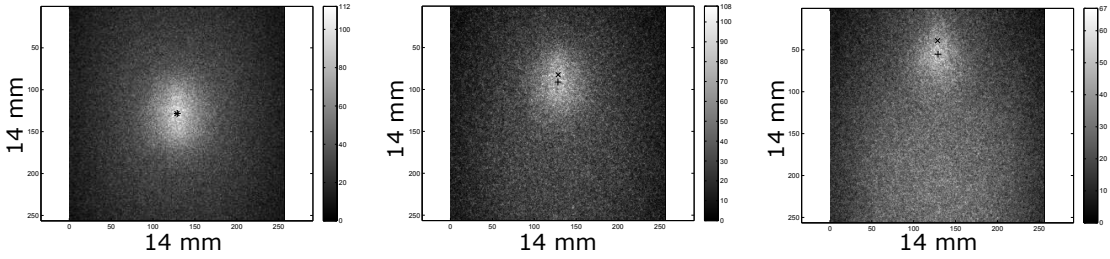

(a) $h = 7$mm, $\theta = 90°$ (b) $h = 7$mm, $\theta = 72°$ (c) $h = 7$mm, $\theta = 57°$

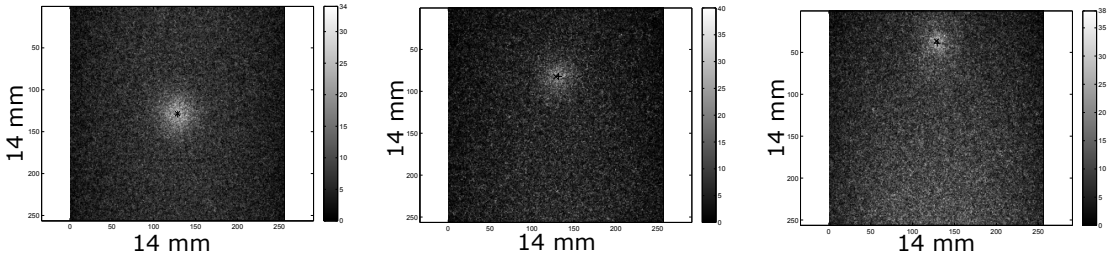

(d) $h = 23$mm, $\theta = 90°$ (e) $h = 23$mm, $\theta = 72°$ (f) $h = 23$mm, $\theta = 57°$

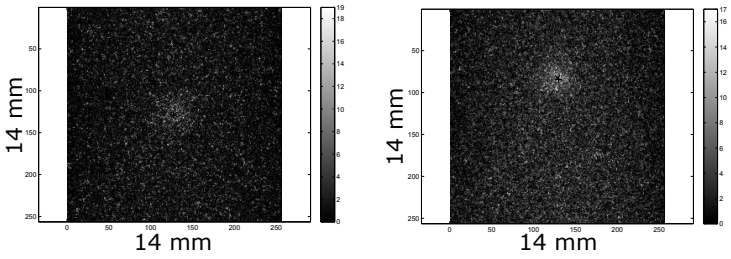

(g) $h = 47$mm, $\theta = 90°$ (h) $h = 47$mm, $\theta = 72°$

Figure 6.3: Simulated projection images of a single pinhole collimator and source in 8 different positions within the FoV. h is the perpendicular distance between source and the pinhole centre and θ is the incidence angle measured from the pinhole plane (Figure 6.1). The positions of the CoM of source projections calculate from geometry and simulation image are marked with a red `x` and a blue `+` respectively.

Table 6.1: Error of estimated CoM on detector plane for the source in different positions.

Source position	dx in detector plane (mm)	dy in detector plane (mm)
$h = 7.21$ mm, $\theta = 90°$	0.026	-0.012
$h = 7.21$ mm, $\theta = 72°$	-0.014	0.509
$h = 7.21$ mm, $\theta = 57°$	0.028	0.945
$h = 23.14$ mm, $\theta = 90°$	0.009	0.027
$h = 23.14$ mm, $\theta = 72°$	0.191	-0.013
$h = 23.14$ mm, $\theta = 57°$	0.055	0.155
$h = 47.21$ mm, $\theta = 90°$	-0.062	0.034
$h = 47.21$ mm, $\theta = 72°$	0.075	0.107

are identical to those shown in Figure 3.1. The maximum error (in the detector plane) in the X direction (dx) is less than 0.2 mm, while the most of these errors are around 0.05, which is within the intrinsic resolution of detector. The maximum error in the Y direction (dy) occurs when the source is closest to the pinhole ($h = 7$ mm) and at the edge of its FoV, and is approximately 0.945 mm.

Figure 6.4 shows the source projection image through two adjacent pinholes as discussed in Section 6.2.2. As there is a clear separation of the two projections, it is possible to correctly estimate the respective CoMs of each projection without contamination from nearby projections.

The calculated error in resolving the centre of the reconstructed source placed at different positions within the prostate volume is listed in Table 6.2.

6.4 Discussion

The projections observed in the single pinhole simulation (shown in Figure 6.3) demonstrates that the SBR deteriorates at the edge of the FoV, with a minimum peak value of 17 counts detected for the projected image of the source for 20 billion simulated photons. However, given that the typical activity of the ^{192}Ir sources used in HDR

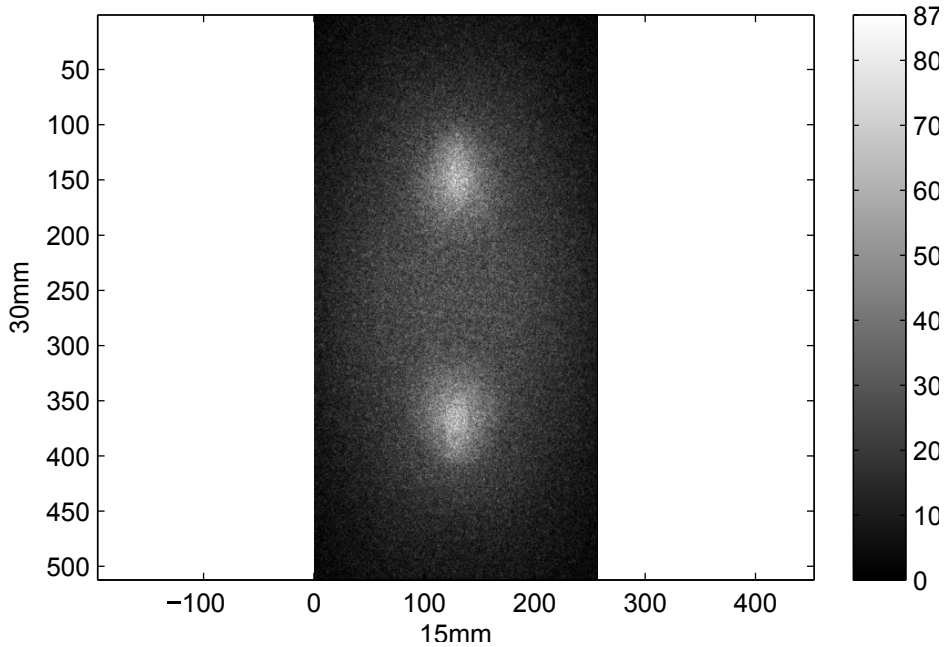

Figure 6.4: Simulation of double pinhole collimator; the distance between the pinholes is 6.5 mm (centre to centre) and the source is placed 5 mm above the collimator and aligned with the axis joining the two pinholes.

Table 6.2: Estimated difference in reconstructed and pre-defined source locations within the prostate phantom.

Source position	dx (mm)	dy (mm)	dz (mm)	$\sqrt{dx^2+dy^2+dz^2}$ (mm)
$h = 7.21$ mm, $\theta = 72°$	0.014	-0.053	1.475	1.476
$h = 7.21$ mm, $\theta = 57°$	0.020	-0.114	1.367	1.372
$h = 23.14$ mm, $\theta = 90°$	0.001	-0.075	-0.358	0.366
$h = 23.14$ mm, $\theta = 72°$	0.262	-0.248	-0.933	1.001
$h = 23.14$ mm, $\theta = 57°$	0.168	-0.057	0.593	0.619
$h = 47.21$ mm, $\theta = 90°$	-0.280	-0.189	-0.127	0.361
$h = 47.21$ mm, $\theta = 72°$	0.468	-0.290	1.030	1.168

prostate brachytherapy is around 370 GBq (corresponding to a photon flux of 870 billion photons per second), it is reasonable to predict that *HDR BrachyView* system is capable of resolving the source within a sub-second dwell time. Therefore, the system is suitable for real-time source tracking.

The uncertainty values listed in Table 6.1 demonstrate that the source positioning error on detector plane in the X direction is within the intrinsic spatial resolution of the detector. The maximum error in resolving the CoM of the source projection in the Y direction is 0.945 mm. This shift could be due to the asymmetry of pinhole sensitivity with respect to the point of origin of emitted photons along the longitudinal axis of the source. The sensitivity of a pinhole collimator S_t is defined as the fraction of photons emitted from a point source that reach the camera detector, and is the sum of the "direct" (S_d) and "penetrative" (S_p) sensitivities:

$$S_t(\theta) = S_d(\theta) + S_p(\theta) \tag{6.1}$$

where θ is the incidence angle of photons on the pinhole plane. For an aperture with a pinhole diameter of d, the direct sensitivity calculated for a point source placed at a distance h from the pinhole plane is given by [178]:

$$S_d(\theta) = \frac{d^2 \sin^3(\theta)}{16h^2} \tag{6.2}$$

The penetrative term can be analytically determined by calculating the path length of incident photons through the collimator from an ideal point source and then integrating the attenuated flux over all points constituting a line source such as an ^{192}Ir seed [179]. Furthermore, the penetrative sensitivity can be further approximated, assuming that photons with an incident angle of $\theta < (\pi - \alpha)/2$ are mostly stopped due to the large volume of material they traverse [179]. Therefore, for a pinhole collimator

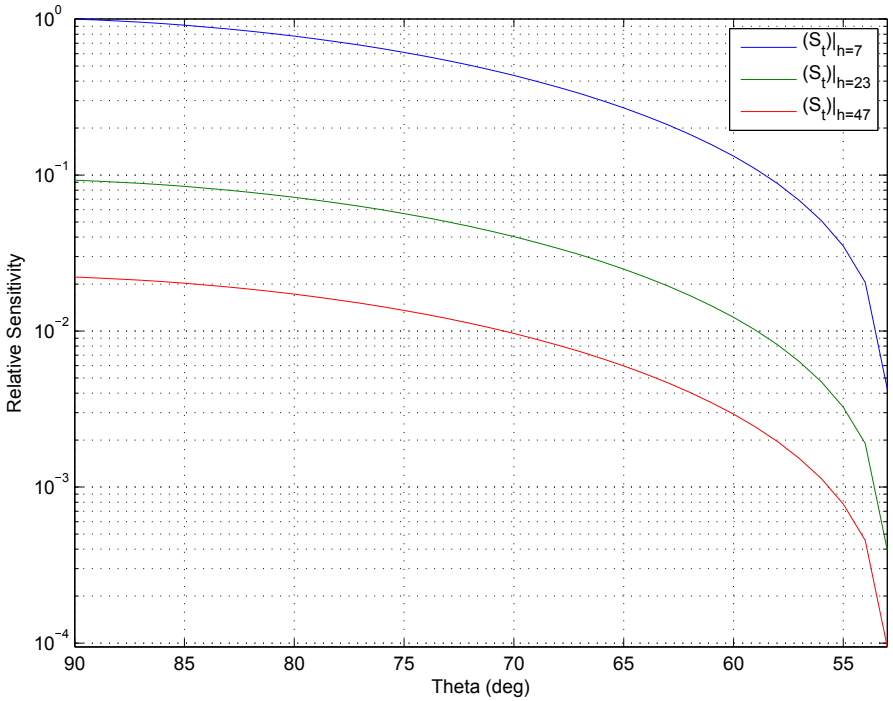

Figure 6.5: Analytical estimate of *HDR BrachyView* pinhole sensitivity (with penetration) versus *theta* using an ^{192}Ir point source with tungsten collimator, normalised to 1 at $\theta = 90°$ and $h = 7$ mm.

with an opening angle of α and a diameter of d:

$$S_p(\theta) \approx \frac{\sin^5\theta \tan^2\frac{\alpha}{2}}{8h^2\mu^2} \times \left(1 - \frac{\cot^2\theta}{\tan^2\frac{\alpha}{2}}\right)^{1/2} \times \left[1 - \frac{\cot^2\theta}{\tan^2\frac{\alpha}{2}} + \mu d \csc\theta cot\frac{\alpha}{2}\right] \tag{6.3}$$

The theoretical relative sensitivity of the *HDR BrachyView* pinhole is plotted for a point source placed at different heights above the collimator (normalised for $h = 7$ mm and $\theta = 90°$) and is shown in Figure 6.5. When the source is placed 7 mm above the pinhole, θ varies from 58° to 74° for photons emitted along the Y-axis, resulting in an 84% variation in sensitivity across the length of the source. The predicted relative reduction in the total sensitivity for different source positions based on the analytic model is in good agreement with the results of the Monte Carlo simulations presented

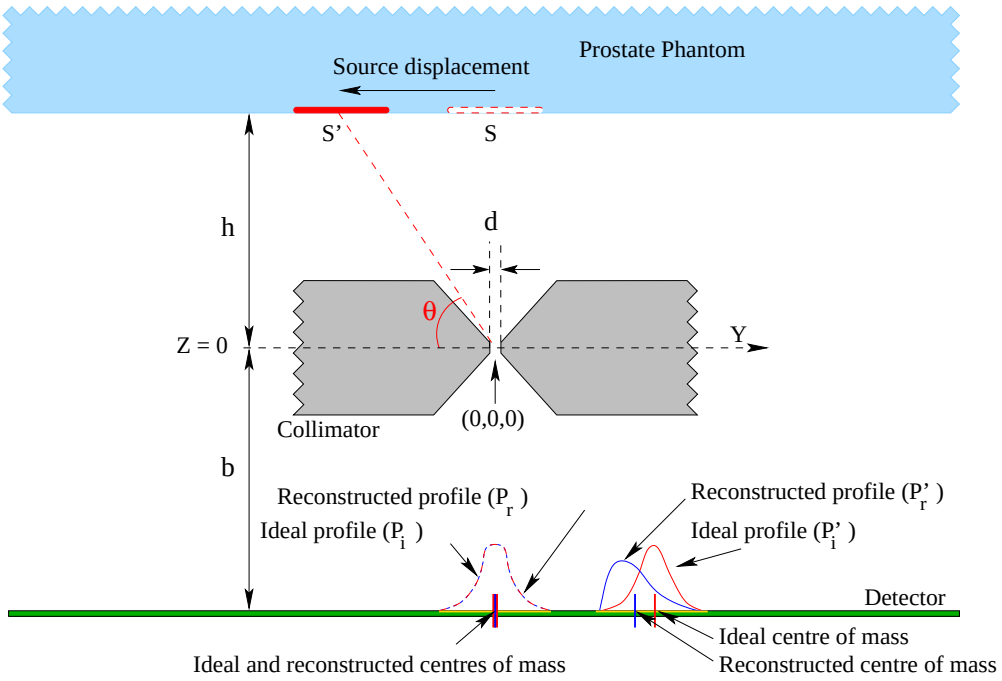

Figure 6.6: Geometry for asymmetric projection: Ideal centre projection is a reference position defined as the projection of source centre on detector through the centre of pinhole. The projection image centre is the centre position calculated from the image.

in Section 6.3.

The non-uniform distortion of the pinhole response function in the Y direction for a linear brachytherapy source is illustrated in Figure 6.6. As the source is moved along the Y axis (from position S to S'), its inverted projection moves in the opposite direction. While the Y-axis projection profile is symmetric at normal incidence angle ($\theta = 90°$), the reconstructed source profile is significantly distorted when the source is moved along the Y axis, with its CoM moving towards the pinhole. Since the variation of the relative sensitivity along the longitudinal source axis is inversely proportional to the square of the distance between the source and the pinhole (h^2), the error in the CoM (on the detector plane) also decreases with the increased source to pinhole distance.

To further investigate the effect of asymmetry of pinhole sensitivity on locating the CoM, a one dimensional sensitivity correction map was obtained from simulation and

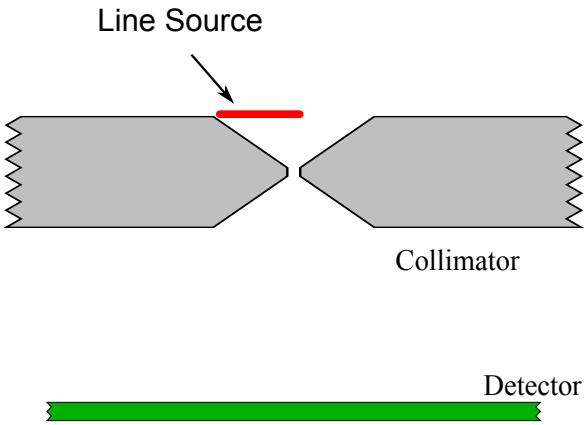

Figure 6.7: Figure illustrates the configuration of the simulation to obtain the sensitivity correction map.

applied to the source projections presented above. Then, the errors of CoMs located using the images before and after the sensitivity uniformity correction are compared. The configuration of the simulation is illustrated in Figure 6.7, the model of collimator is same as the single pinhole collimator described above. A line ^{192}Ir source is placed at the top surface of the collimator to cover half of the pinhole's FoV. The line source is parallel to the axis of the probe in the plane of X=0. The primary particles generated in the simulation is restricted in the plane of X=0 to accelerate the computing speed. Since the real ^{192}Ir source for HDR brachytherapy can be regarded as a part of the line source across half of the FoV, the distortion of the projection of real ^{192}Ir source can be corrected by the corresponding region of the profile of the image obtained in this line source simulation.

A line profile of X=0 is retrieved from the image obtained from the simulation. This profile is then normalized to its maximum (denoted as P(y),where y is the y coordinate of the pixel) and used to correct the asymmetry of pinhole sensitivity. The profile is plotted in Figure 6.8. The detector responds of the line source could reduce to 30% of its responds close to the centre of the detector. The drop of responds at the centre of the detector (in this scenario, the centre of the detector is refer to the

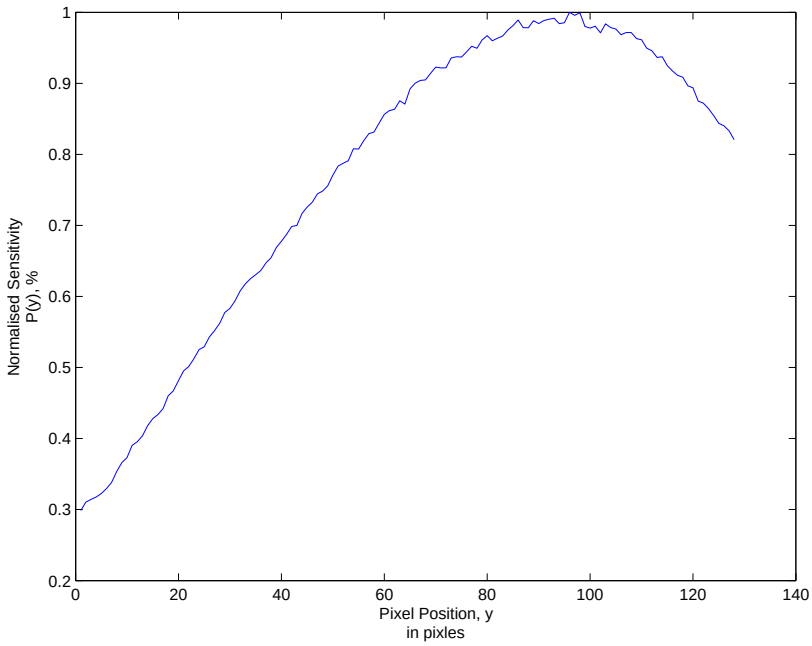

Figure 6.8: Plot demonstrates the change of detector respond of a line source cover half of the FoV along the line of X=0. The centre of the detector is represented as y = 128.

position of detector right below the center of pinhole) shown in the profile is due to the absence of source at the other side of pinhole's FoV (Figure 6.9). However, since the non-uniform distortion is not significant at the centre of the detector, the P(y) at the region close to centre is set as one.

The source projection images from single pinhole collimator simulation are modified by dividing the pixel values with the corresponding P(y). Figure 6.10 demonstrates the image after the sensitivity correction. As expected the overall counts distribution shifted toward the edge of the image. However a significant over boost of counts is observed at the edge of the image, although the source projection is still distinguishable. This over correction of sensitivity is caused by the under-estimation of sensitivity in the correction map. It could be due to the same reason of the under estimation at the centre of the detector, which has been discussed above. To avoid the effect of sensitivity over-correction on the CoM locating, the sensitivity correction only applied

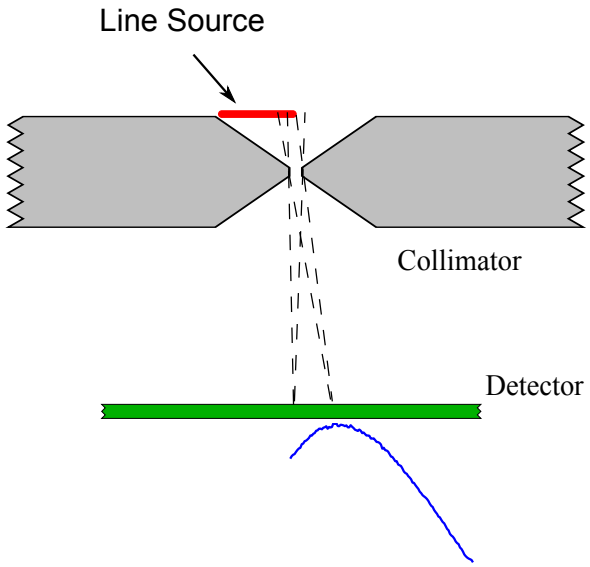

Figure 6.9: Figure demonstrate the reduce of detector respond at the centre of the detector

to the region of source projection and its perimeter. Then the CoMs of these modified images are calculated and compared to the original results.

The improvement of the accuracy of estimating the location of the calculated CoM caused by the sensitivity correction is presented in Table 6.3. No variation was observed for the source positions of $\theta = 90°$, since the P(y) was set as one at the centre of the detector. The errors are significantly reduced for other source positions at h=7.21 mm, where the effect of asymmetry of pinhole sensitivity dominants. Although the sensitivity correction was only applied at the region of source projection, shift of calculated CoMs toward the edge of the detector caused by over boost of sensitivity at the edge of the detector was found when sources were placed at $\theta = 67°$ (close to the edge of FoV). The significant improvement of accuracy after the sensitivity correction validated that the asymmetry of pinhole sensitivity is a majority source of error when estimating the position of CoM. However, it is hard to apply this correction in practise due to its dependency of pre-knowledge of the pinhole position corresponding to the target source projection. Thus, the evaluation of the localization of CoM in the fol-

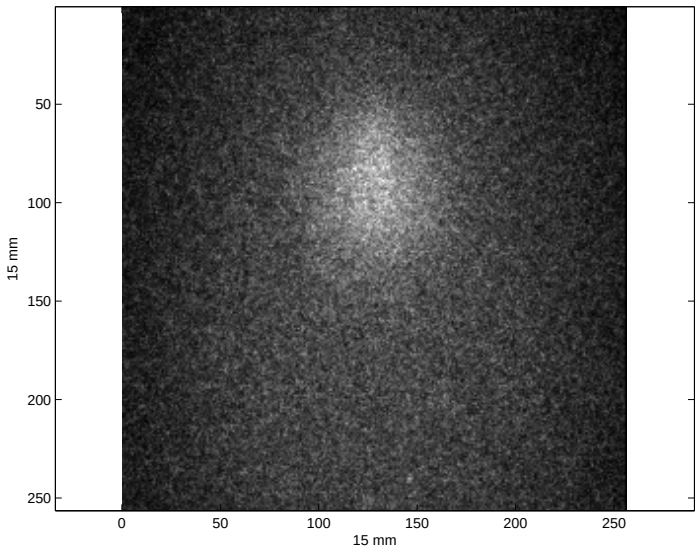

(a) $h = 7$mm, $\theta = 72°$, without sensitivity correction

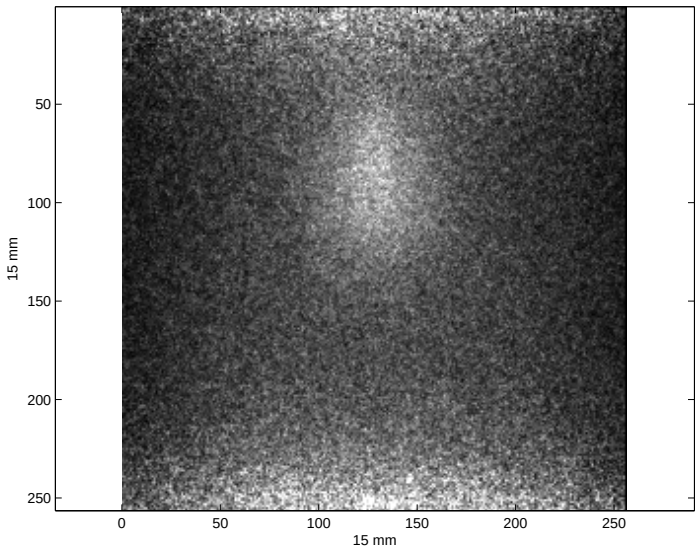

(b) $h = 7$mm, $\theta = 72°$, after sensitivity correction

Figure 6.10: Images of source projection before and after the sensitivity correction when source placed at $h = 7$mm, $\theta = 72°$.

Table 6.3: Error of estimated CoM in y direction on detector planewith and without sensitivity correction.

Source position	dy in detector plane (mm) with sensitivity correction	dy in detector plane (mm) without sensitivity correction
$h = 7.21$ mm, $\theta = 90°$	-0.012	-0.012
$h = 7.21$ mm, $\theta = 72°$	0.193	0.509
$h = 7.21$ mm, $\theta = 57°$	-0.215	0.945
$h = 23.14$ mm, $\theta = 90°$	0.027	0.027
$h = 23.14$ mm, $\theta = 72°$	0.016	-0.013
$h = 23.14$ mm, $\theta = 57°$	-0.077	0.155
$h = 47.21$ mm, $\theta = 90°$	0.034	0.034
$h = 47.21$ mm, $\theta = 72°$	0.050	0.107

lowing part of this chapter is still based on the source images without the sensitivity correction.

The error in resolving the location of the source within the prostate volume varies between 0.361 mm (where the source is directly above the collimator) and 1.476 mm (when the source is at the edge of the field of view). While the error is significant, it is worth noting that it was only calculated based on two projections, where as in reality, there will be seven projections for source placed at that distance. This will ultimately result in a more accurate estimation of the CoM of the source. Furthermore, the error clearly includes a component which is clearly a function of source position; this is due to the fact that the CoM of the projected image is not quite perfectly aligned with the ideal point of intersection of the line projected from the centre of the source. Therefore it will be possible to develop a model for the error as a function of position, either via simulation or experimentally using a calibration procedure, which can correct for this systematic component of the error. This issue will be addressed in the future phase of research.

6.5 Conclusion

The simulation results presented in this Chapter indicate that *HDR BrachyView* should be able to accurately determine the position of the ^{192}Ir source centre from multiple images projected on an array of Timepix detectors through a series of pinholes in a tungsten collimator within the minimum the dwell time of the source. Several sets of Geant4 simulations have been performed to validate the design. These simulations show that there is a small shift toward the perpendicular projection of the pinhole centre on the detector plane in each image, which is a result of the asymmetry of the projected image when the source is not placed directly above the pinhole. The simulation results show that the errors in estimating the CoM of the projection in the detector plane will not exceed 1 mm in the worst case, and that the positioning error decreases when the source is placed further away from the collimator. The simulated double pinhole studies indicate that the maximum error in calculating the source position within the prostate volume will be less than 1.5 mm.

A partial prototype of the *HDR BrachyView* system has been developed with two tiled Timepix chips (14 mm $\times$ 28 mm, half of the proposed detection area in the complete design, and sufficient for the purpose of this research. Experimental studies with this prototype collimator and an actual HDR source have been performed in a phantom to validate the simulation results; the result of these experiments are presented in next Chapter.

Chapter 7

Experimental Evaluation of *HDR BrachyView* Design

7.1 Introduction

The previous Chapter characterised the expected performance of *HDR BrachyView* in detail via Monte Carlo simulations. The results from simulations indicate that a maximum error of 1.5 mm within the maximum extent of the prostate volume can be obtained within a sub-second acquisition time (with the source up to 45 mm away from the collimator's top surface). Furthermore, additional Monte Carlo simulations and preliminary experimental work presented in Chapter 5 have demonstrated that the dose enhancement at the rectal wall resulting from backscatter from the tungsten wall of *HDR BrachyView* probe is negligible provided that the probe is encapsulated in a tissue-equivalent plastic shell with a thickness of at least 0.5 mm.

This Chapter presents an experimental validation of the range and accuracy of source position tracking using the *HDR BrachyView* probe. It starts with a feasibility validation of the design using a planar tungsten collimator with a single Timpix detector. Next, a prototype of the *HDR BrachyView* probe is introduced. A comprehensive

experimental evaluation of *HDR BrachyView* is performed using this prototype, and the results are presented.

The rest of this chapter is structured into two main sections. The preliminary experimental validation of the feasibility of the *HDR BrachyView* design is presented in Section 7.2; the complete evaluation of a system using a limited prototype of *HDR BrachyView* is presented in Section 7.3.

7.2 Experimental Feasibility Study with Planar Collimator and Single Timepix

7.2.1 Material and Methods

The experimental study was performed at St. George Hospital Cancer Care Centre, Kogorah, NSW. The objective of this study is to validate the feasibility of *HDR BrachyView* design in terms of its sensitivity and experimental uncertainty, in particular to assess the reliability of determining the CoM of the source projection (no 3D image reconstruction being performed at this stage; this will be explored in Section 7.3. Figure 7.1 shows the experimental apparatus, which consists of a 4 mm thick planar tungsten collimator with seven double-cone pinholes positioned 9 mm above a single Timepix detector (as measured from the top surface of detector to the centre plane of collimator). The planar collimator is used in this experiment rather than the cylindrical collimator as it permits more convenient repositioning of the detector for preliminary experimental characterisation of the design, and is considerably easier and cheaper to manufacture.

A catheter was placed inside a solid water prostate phantom, in a channel which is parallel to the collimator pinholes and positioned 45 mm above the central axis of the collimator. This height was selected as the worst case in terms of source tracking

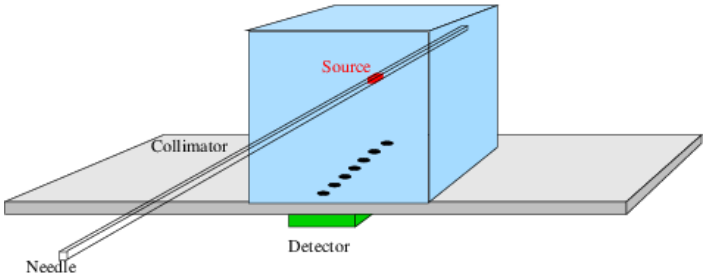

Figure 7.1: Experimental apparatus.

accuracy and uncertainty which are proportional to the source to detector distance. The source positions in a close proximity of the detector plane may also be interesting to study. However, due to single Timepix was used in this experiment, it is difficult to obtain multiple full size source projections for most source depths in the catheter placed most close to the detector (5 mm above the collimator surface). Measurement of source placed to a close proximity will be interesting to investigate the FoV of *HDR BrachyView* system in the future study with a prototype of full length Timepix detector array. A Flexitron afterloader was used to deliver a ^{192}Ir source into the phantom via the catheter. At the time of the experiment, the source activity is approximately 217.6 GBq; this source was stepped through the catheter in 1 mm increments, with a dwell time of 1.7 s for each source position. This dwell time is equivalent to 1 s for a standard 370 GBq source, which is calculated by afterloader system.

The Timepix detector was coupled to the Fitpix USB data acquisition module and connected to a dedicated data acquisition laptop. The detector was operated with a frame duration of 0.5 seconds per frame, with each frame displayed in real time via the Pixelman user interface. The index of the frame which registered the first source projection was recorded as the start frame. Since the source dwell time is 1.7 s, the 3 frames following the start frame correspond approximately to one particular source position. The position of the CoM for each projection in these images was then calculated as per the methods discussed in Chapter 4. As shown in Figure 7.2,

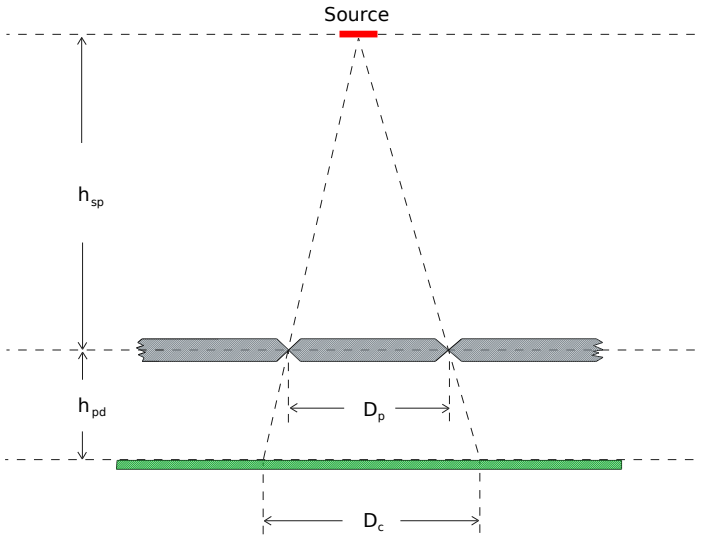

Figure 7.2: Schematic showing distance between CoMs

the distance between the CoMs of any two adjacent source projections (D_c) can be expressed as:

$$D_c = \frac{h_{pd} + h_{sp}}{h_{sp}} \times D_p \tag{7.1}$$

where h_{sp} is the distance between the source and collimator, h_{pd} is the distance between the detector and the collimator, and D_p is the distance between adjacent pinholes.

Because the value of h_{sp}, h_{pd} and D_p were kept constant as 45 mm, 9 mm and 6 mm, respectively, throughout the experiment, D_c on the detector plane also remains constant and is expected to be 7.2 mm. This quantity was measured and used to estimate the uncertainty of the *HDR BrachyView* probe in locating the projection's CoM.

7.2.2 Results

Two projection frames in which the source has been projected through adjacent pinholes on the detector are shown in Figure 7.3. The position of the centres of mass

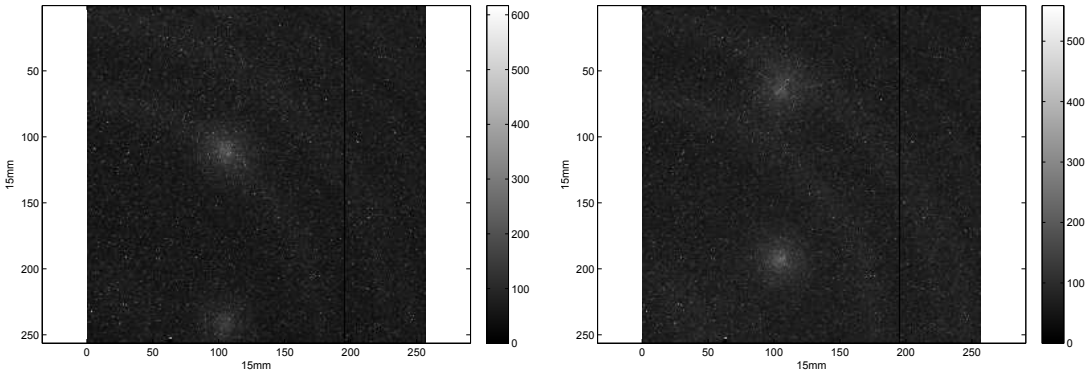

(a) Position 1, $h_{sp} = 43$ mm (b) Position 2, $h_{sp} = 43$ mm

Figure 7.3: Projection images of the source through two pinholes on the detector plane for two different source positions; exposure time is 0.5 s.

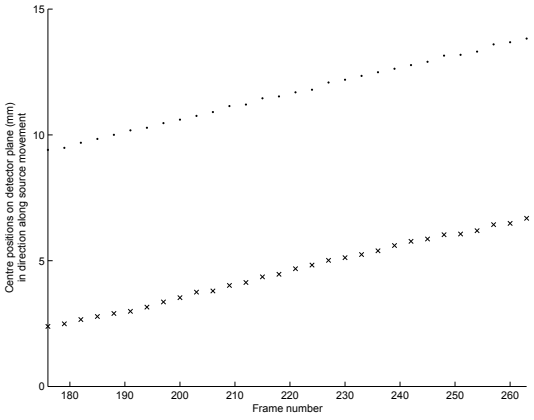

Figure 7.4: Positions of the source CoM on the detector plane

of the source projections through two adjacent pinholes for all source locations were plotted and are shown in Figure 7.4. The movement of the projection on the detector plane along the direction of the source movement in constant increments is clearly visible. The measured distance between the centres of mass of two adjacent projections on the detector plane is also shown in Figure 7.5. The average distance between the two projections in same frame was measured to be 7.1±0.1 mm and are shown for all source positions. This value is with a good agreement to the expected value (7.2 mm).

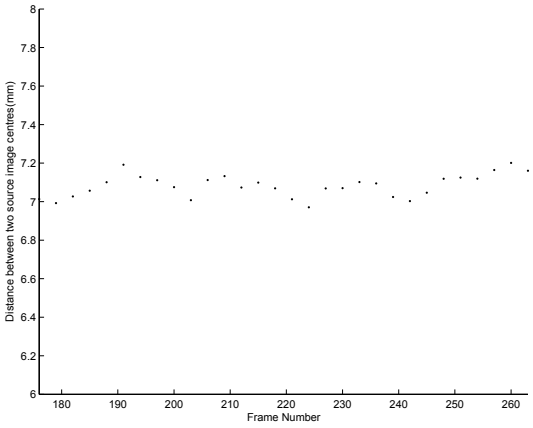

Figure 7.5: Distance between CoMs of projections on detector plane

7.2.3 Discussion

The experiment serves to validate several basic concepts used in the *HDR BrachyView* design. Although the experiment does not yet provide an estimate of the error of the estimated source position in three dimensions, it is a necessary preliminary step in quantifying the error in the detector plane (which is directly related to the final positioning error via the geometry of the detector and collimator arrangement).

The plot of the CoMs (Figure 7.3) demonstrates the capability of *HDR BrachyView* to resolve the projection CoMs when the source was placed 43 mm above the collimator. The Timepix has not been masked or equalised, and the raw response of the detector can be seen in the images, which show an interesting concentric artifact resulting from non-uniformities in the doping of the detector's semiconductor substrate (bias voltage of 100 V was applied to the sensor). The appearance of a minority of samples in an adjacent position are due to the difference between source dwell time and interval of samples. Since the frame duration is 0.5 s per frame and every third frame was plotted, the interval between samples is 1.5 s which is 0.2 s shorter than the source dwell time (1.7 s). This makes it possible that two adjacent plotted frames are obtained when source is in same position. The value of h_{sp} of 43 mm corresponds to the most distant extent of the maximum prostate size that *HDR BrachyView* probe is expected to need

to be able to to track with the specified sub-1 mm accuracy, which represents the worst case of 'minification' seen within the treatment volume.

As shown in Figure 7.5, the consistency of the distance between the CoMs of two projections in each frame is a confirmation of the ability of the system to precisely track the CoM of the source image independently of the angular view of the source. The distance is estimated with a maximum error of 0.2 mm on the detector plane, which includes the uncertainty of both CoMs. Therefore, for the source locations evaluated (43 mm above the plane of the centre of the collimator), the maximum error in CoM location determined by the *HDR BrachyView* probe is approximately 0.1 mm

7.3 Evaluation with *HDR BrachyView* prototype

A *HDR BrachyView* prototype has been fabricated and its accuracy in tracking the HDR source for sub-second dwell times was evaluated experimentally. The design of the *HDR BrachyView* prototype and the experimental configuration are detailed in Section 7.3.1. The resulting source positions are presented and compared with planned positions in Section 7.3.3. A thorough analysis of the results including a discussion on the possible sources of error is presented in Section 7.3.4. The conclusion and possible approaches to improve the accuracy of source tracking are provided in Section 7.4.

7.3.1 Material and Methods

The design of the prototype implementation of *HDR BrachyView* is described in subsection 7.3.1.1. The experimental configuration is detailed in subection 7.3.1.2. Finally, a description of the data processing methods is given in subsection 7.3.2.

7.3.1.1 Design of *HDR BrachyView* prototype

The prototype is developed based on the design of *HDR BrachyView* described in Chapter 3, while a small modification has been applied due to the different geometry of the Timepix array provided by the manufacturer. As shown in Figure 7.6, the prototype probe consists of a semi-cylindrical tungsten collimator, coupled to a semi-cylindrical aluminium base of the same diameter which houses two tiled Timepix detector arrays. The Timepix detectors array is located at one side of the probe axis while the PCB is connected at the side of the detector array. The detector array includes two 14 mm × 14 mm Timepix detectors, providing a total 14 mm × 28 mm sensitive detection area. Although this is smaller than the full *HDR BrachyView* design, it was the only working multi-detector module available at the time of the experiment, so a full four-detector array could not be tested. However, a two-detector array is sufficient to demonstrate the source tracking accuracy of the resulting system. The array of two Timpix detectors in the prototype is capable of covering half of the target volume. This is sufficient for the evaluation of the probe performance by moving the source within the first half of the FoV.

Seven equi-distant double-cone pinholes (centre-to-centre spacing of 6.5 mm) were machined into the collimator, parallel to the central axis of the probe. The axis of the pinholes is right above the central axis of the detector array. The geometry of the truncated double cone pinholes and their preferred placement have been discussed in previous Chapters. However, the geometry of the prototype board on which the Timepix chips were mounted were such that it was not possible to align the centre of the detectors with the centre of the collimator tube. Therefore the pinholes were fabricated with the same offset as the detectors to maintain the alignment of pinholes centre and the centre of detector array. As shown in Figure 7.6, such an arrangement of detector array and pinhole array results in a pinhole centre to detector distance of

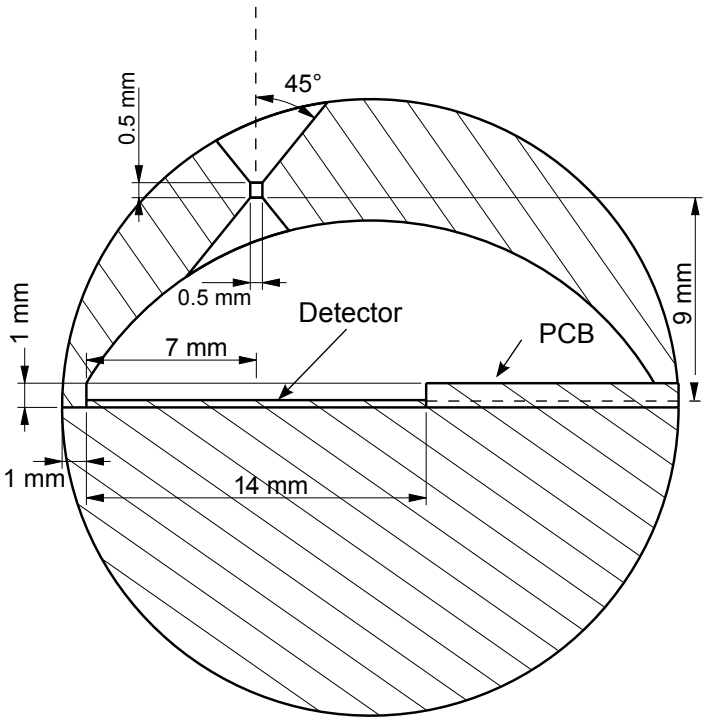

Figure 7.6: Schematic diagram showing the cross section of the prototype.

9 mm and an acceptance angle of the double cone pinhole of 90°. A cylindrical channel with a diameter of 0.5 mm and a length of 0.5 mm connects the top and bottom cones.

7.3.1.2 Configuration of Experimental Apparatus

The experiment was again conducted at the HDR Brachytherapy facilities at the St. George Hospital Cancer Care Centre, Kogorah, NSW. The experimental apparatus consists of four main components: the *HDR BrachyView* prototype probe, a linear translational stage, a simplified prostate phantom, and a HDR brachytherapy source delivered by an Flexitron HDR afterloader. The experimental configuration is shown in Figure 7.7(a). A schematic of the probe and the Plastic Water phantom is illustrated in Figure 7.7(b). A global Cartesian coordinate system was introduced and is also shown in Figure 7.7(b), with its origin placed at the top left corner of the first detector (first row and first column of the imaging plane).

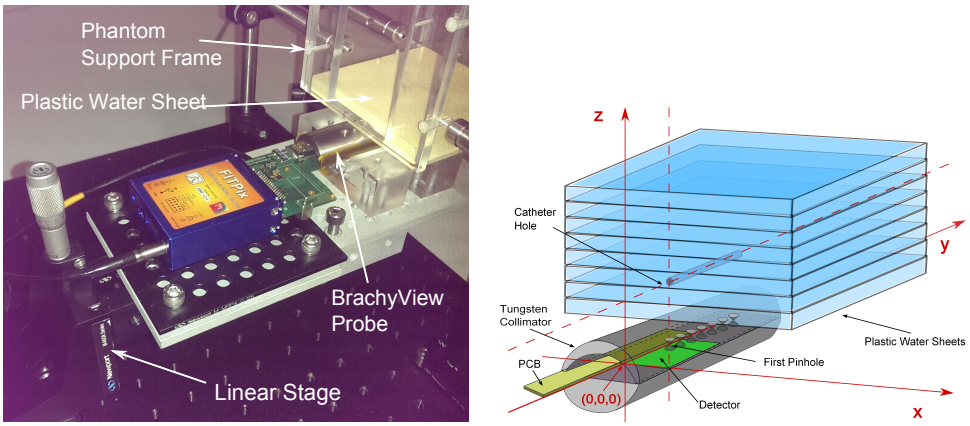

(a) Experimental Configuration (b) Schematic

Figure 7.7: The experimental configuration showing the probe, translational linear stage and the phantom; the relative positioning of the components and the coordinate system is shown in Figure 7.7(b)

The phantom comprises a series of 90 mm × 90 mm Computerized Imaging Reference Systems (CIRS) Plastic Water®sheets, each with a thickness of either 5 mm or 10 mm and optimised for photon energies from 15 keV to 8 MeV (agree with water within 1%). A 2 mm diameter channel was etched halfway along the central axis (y axis) of a 90 mm × 90 mm × 10 mm Plastic Water sheet. This allowed for the insertion of a catheter into which a ^{192}Ir HDR brachytherapy source was remotely moved by a Flexitron HDR afterloader. In each catheter, the source was moved into six preplanned positions along the y axis, starting at the entrance of the catheter within the phantom and moving in positive y direction in steps of 4 mm. The Plastic Water sheets were rearranged to place the catheter either 40 mm or 60 mm above the detector plane of the *HDR BrachyView* probe along the y axis, as illustrated in Figure 7.7(b) and Figure 7.8.

A Newport M-460A-XYZ linear translational stage with a 1 um accuracy was used to move the probe laterally (along the x axis) in four 2.5 mm steps, relative to the phantom and the catheter. A total of eight catheter positions were thus simulated. The position of the phantom relative to the probe is shown in Figure 7.8(a), where

Table 7.1: Planned Source Positions for each test.

Test	Source Positions x (mm)	y(mm)	z (mm)
1	7	6 positions from 8.5 to 28.5 with a step of 4	37
2	7		57
3	9.5		57
4	9.5		37
5	12		37
6	12		57
7	17		57
8	17		37

the front face of the phantom is offset from the centre of the first pinhole by 0.3 mm, due to the mechanical constraints of the experimental apparatus.

Source dwell times were calculated for an equivalent full strength ^{192}Ir source, with an air kerma strength of 40.7 mGyh^{-1}m^2. A 43 s dwell time at each preplanned source position was calculated by the Nucletron treatment planning system, equivalent to a 20 s dwell time for a full strength source. A list of all planned source positions is provided in Table 7.1.

7.3.2 Image Acquisition and Source Position Computation

The two Timepix2 chips were calibrated and equalised to ensure a uniform response across the full array and were configured to continuously acquire and record frames at a rate of ten frames per second. Groups of ten frames were accumulated to produce images with an effective acquisition time of one second; an average of 18 such images were collected for each source position, with any frames captured during source movement being discarded. The images collected for each source position were then individually processed to extract the centres of mass (CoMs) of all visible projections, which is used as an approximation for the projected source centre. The CoMs were backprojected through their corresponding pinholes and the three dimensional source

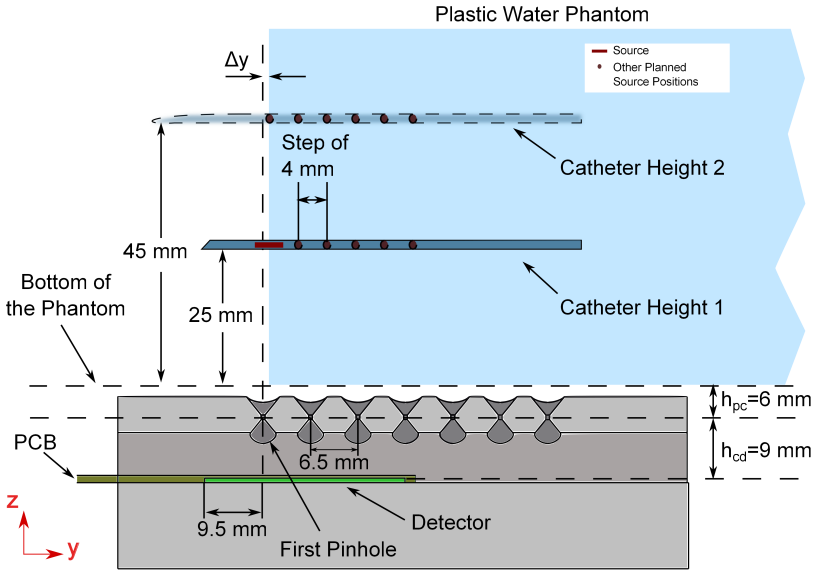

(a) Longitudinal Cross-section

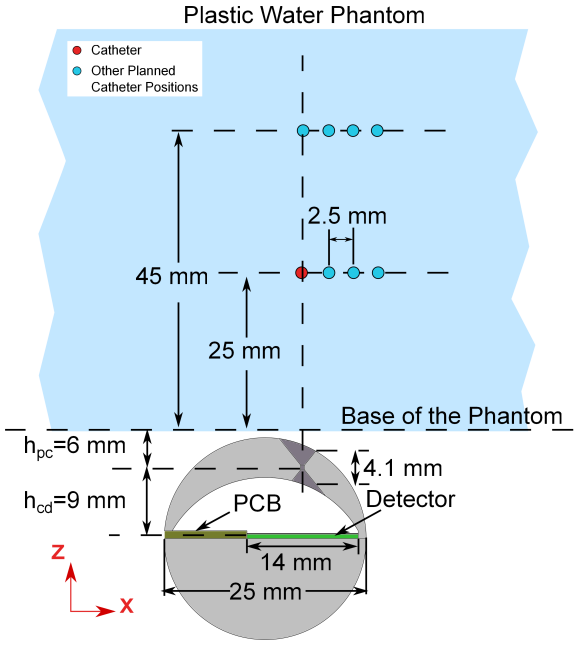

(b) Transversal Crosss-ection

Figure 7.8: The cross-sections of the *HDR BrachyView* prototype probe, the phantom and the planned source positions. The experimentally evaluated catheter positions are marked within the phantom. Sheet boundaries are omitted.

location, the point with the least square distance to these rays is found for each one-second acquisition. The mean source position estimate and corresponding standard deviation for each source position were then calculated across the set of images for that position.

The detail of the image processing and the calculation of source position in the volume has been explained in detail in Chapter 4. For the prototype probe, an additional complication was that the pixels at the boundary between the two adjacent detectors were observed to suffer from very high levels of background noise. Therefore, the counts recorded by these pixels are replaced by a linear interpolation between the neighbouring pixel values. An example of the detector response recorded before and after the correction is shown in (Figure 7.9).

7.3.2.1 Film Verification of the Displacement in y Direction

The source displacement along the y axis was independently verified using a set of film projection images, taken concurrently with the measurements acquired by the *HDR BrachyView* probe.

Gafchromic®EBT3 films were cut into 90 mm × 90 mm pieces and inserted between the plastic water sheets comprising the phantom, 5 mm below the centre of the catheter. The source was moved into five pre-planned positions along the y axis in steps of 10 mm, starting at the entrance of the catheter within the phantom. The measurements were repeated for two source to detector plane distances of 40 mm and 60 mm.

The source projection images on each films were analysed and their CoMs were calculated. The y coordinates of the CoMs were compared with the source positions tracked by the *HDR BrachyView* probe.

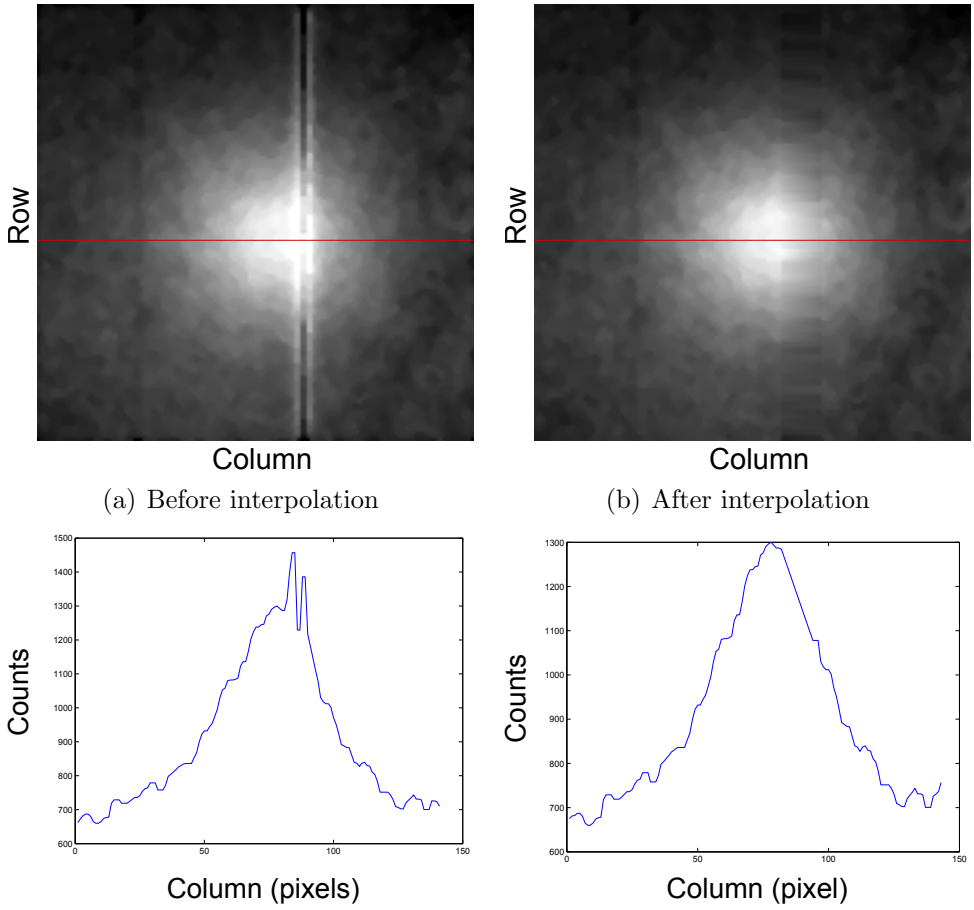

(a) Before interpolation

(b) After interpolation

(c) Line profile, before interpolation

(d) Line profile, after interpolation

Figure 7.9: Source projection shown at the boundary of the two Timepix detectors; the non-uniform response of the detector array has been corrected using linear interpolation.

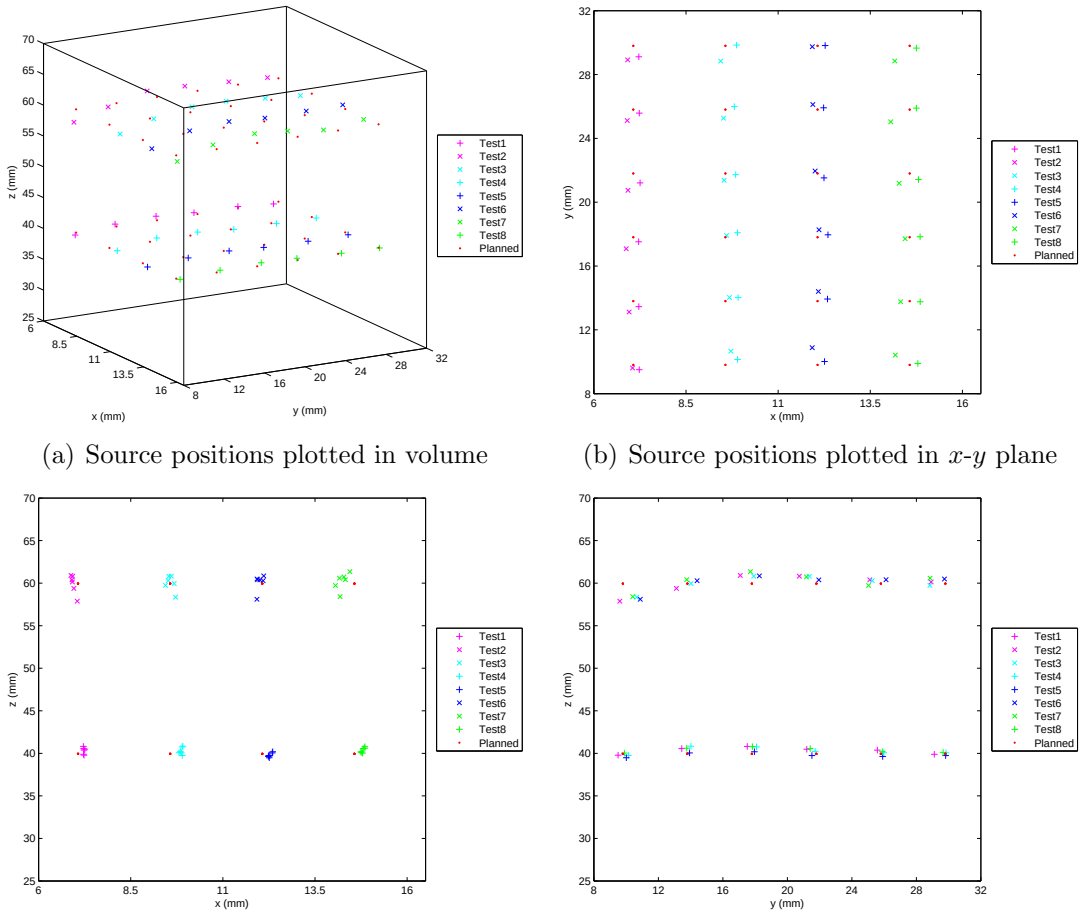

(a) Source positions plotted in volume

(b) Source positions plotted in x-y plane

(c) Source positions plotted in x-z plane

(d) Source positions plotted in y-z plane

Figure 7.10: Figures demonstrate the coordinates of calculated and planned source positions.

7.3.3 Results

The mean calculated source positions are plotted in Figure 7.10, both in three dimensions and projected on to the three main planes of the coordinate system (defined in Section 7.3.1.2); nominal (planned) source positions are shown in red for comparison. The difference between the calculated and planned source positions is greatest in the z (vertical) direction, with the error in x slightly greater than for y at $z = 40$ mm and the error in y greater than that in x at $z = 60$ mm.

The mean and standard deviation of the experimentally-estimated source positions are listed together with the nominal (planned) source position, mean error in each

Table 7.2: The coordinates of calculated and planned source positions for a vertical source displacement of 40 mm from the top surface of the detector plane. Standard deviation is denoted SD. The total error between planned and measured/estimated source position $d_{total} = \sqrt{d_x^2 + d_y^2 + d_z^2}$.

Planned (mm)		Mean Estimated Source Positions (mm)						Difference (mm)			
x	y	x	SD_x	y	SD_y	z	SD_z	d_x	d_y	d_z	d_{total}
7.1	9.8	7.2	0.03	9.5	0.04	39.8	0.15	0.1	-0.3	-0.1	0.3
7.1	13.8	7.2	0.02	13.5	0.09	40.6	0.14	0.1	-0.3	0.7	0.8
7.1	17.8	7.2	0.03	17.5	0.09	40.8	0.20	0.1	-0.3	0.9	1.0
7.1	21.8	7.3	0.03	21.2	0.14	40.5	0.20	0.2	-0.6	0.6	0.9
7.1	25.8	7.2	0.03	25.6	0.07	40.4	0.16	0.1	-0.2	0.5	0.5
7.1	29.8	7.2	0.02	29.1	0.12	39.9	0.19	0.1	-0.7	0.0	0.7
9.6	9.8	9.9	0.03	10.1	0.05	39.8	0.16	0.3	0.3	-0.1	0.4
9.6	13.8	9.9	0.04	14.0	0.23	40.8	0.30	0.3	0.2	0.9	1.0
9.6	17.8	9.9	0.05	18.1	0.04	40.8	0.22	0.3	0.3	0.9	1.0
9.6	21.8	9.8	0.03	21.7	0.05	40.2	0.16	0.2	-0.1	0.3	0.4
9.6	25.8	9.8	0.03	26.0	0.11	40.1	0.15	0.2	0.2	0.2	0.3
9.6	29.8	9.9	0.03	29.8	0.09	40.1	0.16	0.3	0.0	0.2	0.4
12.1	9.8	12.3	0.04	10.0	0.05	39.5	0.14	0.2	0.2	-0.4	0.5
12.1	13.8	12.3	0.04	13.9	0.03	40.0	0.14	0.2	0.1	0.1	0.2
12.1	17.8	12.4	0.04	18.0	0.06	40.2	0.13	0.3	0.2	0.3	0.5
12.1	21.8	12.2	0.04	21.5	0.08	39.7	0.17	0.1	-0.3	-0.2	0.4
12.1	25.8	12.2	0.04	25.9	0.07	39.6	0.14	0.1	0.1	-0.3	0.3
12.1	29.8	12.3	0.02	29.8	0.06	39.7	0.11	0.2	0.0	-0.2	0.3
14.6	9.8	14.8	0.05	9.9	0.06	40.0	0.18	0.2	0.1	0.1	0.2
14.6	13.8	14.9	0.05	13.8	0.04	40.6	0.17	0.3	0.0	0.7	0.8
14.6	17.8	14.9	0.07	17.8	0.03	40.8	0.20	0.3	0.0	0.9	0.9
14.6	21.8	14.8	0.06	21.4	0.11	40.6	0.23	0.2	-0.4	0.7	0.8
14.6	25.8	14.8	0.05	25.9	0.07	40.2	0.15	0.2	0.1	0.3	0.4
14.6	29.8	14.8	0.05	29.7	0.09	40.1	0.14	0.2	-0.1	0.2	0.3

dimension (the difference between planned and estimated positions) and overall mean error in Table 7.2 and 7.3 for nominal vertical (z) source-detector distances of 40 mm and 60 mm respectively. Larger errors (nominal to measured) and uncertainties (standard deviation between measurements) were found for the larger vertical source-detector distance, especially in the z direction. For 60 mm nominal vertical source-detector distance, the four largest positioning errors of 2.0 mm, 1.8 mm, 2.1 mm and 1.7 mm were observed when the source was at the front of the phantom (i.e. when $y = 9.8$ mm) for each of the four respective values of x. The errors observed in these positions are significantly greater than for other source positions, for which the maximum overall error is 1.4 mm. The main contributing component to the overall error is an error in the z direction, which is negative for the extreme values of y (at the front surface of the phantom and at the end of the catheter). There is also a smaller positive error in z for the central y positions. It is noted that this pattern in the positioning error is not observed at $z = 40$ mm; a complete explanation of this error is presented in Section 7.3.4.

Table 7.3: The coordinates of calculated and planned source positions for a vertical source displacement of 60 mm from the top surface of the detector plane. Standard deviation is denoted SD. The total error between planned and measured/estimated source position $d_{total} = \sqrt{d_x^2 + d_y^2 + d_z^2}$.

Planned (mm)		Mean Estimated Source Positions (mm)						Difference (mm)			
x	y	x	SD_x	y	SD_y	z	SD_z	d_x	d_y	d_z	d_{total}
7.1	9.8	7.0	0.07	9.6	0.08	57.9	0.50	-0.1	-0.2	-2.0	2.0
7.1	13.8	7.0	0.09	13.1	0.07	59.4	0.63	-0.1	-0.7	-0.5	0.9
7.1	17.8	6.9	0.09	17.1	0.12	60.9	0.69	-0.2	-0.7	1.0	1.2
7.1	21.8	6.9	0.07	20.7	0.08	60.8	0.63	-0.2	-1.1	0.9	1.4
7.1	25.8	6.9	0.06	25.1	0.20	60.4	0.66	-0.2	-0.7	0.5	0.9
7.1	29.8	6.9	0.06	28.9	0.17	60.1	0.59	-0.2	-0.9	0.2	0.9
9.6	9.8	9.7	0.08	10.7	0.10	58.3	0.50	0.1	0.9	-1.6	1.8
9.6	13.8	9.7	0.08	14.0	0.16	60.0	0.77	0.1	0.2	0.1	0.2
9.6	17.8	9.6	0.10	17.9	0.25	60.8	0.75	0.0	0.1	0.9	0.9
9.6	21.8	9.5	0.07	21.4	0.09	60.8	0.60	-0.1	-0.4	0.9	1.0
9.6	25.8	9.5	0.10	25.3	0.23	60.3	0.74	-0.1	-0.5	0.4	0.6
9.6	29.8	9.4	0.07	28.8	0.16	59.7	0.60	-0.2	-1.0	-0.2	1.0
12.1	9.8	11.9	0.12	10.9	0.09	58.1	0.64	-0.2	1.1	-1.8	2.1
12.1	13.8	12.1	0.11	14.4	0.09	60.3	0.60	0.0	0.6	0.4	0.7
12.1	17.8	12.1	0.11	18.3	0.13	60.8	0.71	0.0	0.5	0.9	1.0
12.1	21.8	12.0	0.09	22.0	0.18	60.4	0.68	-0.1	0.2	0.5	0.5
12.1	25.8	11.9	0.09	26.1	0.20	60.4	0.85	-0.2	0.3	0.5	0.6
12.1	29.8	11.9	0.10	29.7	0.21	60.5	0.64	-0.2	-0.1	0.6	0.6
14.6	9.8	14.2	0.12	10.4	0.08	58.4	0.66	-0.4	0.6	-1.5	1.7
14.6	13.8	14.3	0.13	13.8	0.10	60.4	0.74	-0.3	0.0	0.5	0.6
14.6	17.8	14.4	0.17	17.7	0.09	61.3	0.79	-0.2	-0.1	1.4	1.4
14.6	21.8	14.3	0.12	21.2	0.12	60.7	0.79	-0.3	-0.6	0.8	1.0
14.6	25.8	14.1	0.14	25.0	0.21	59.7	0.68	-0.5	-0.8	-0.2	1.0
14.6	29.8	14.2	0.13	28.9	0.21	60.6	0.64	-0.4	-0.9	0.7	1.2

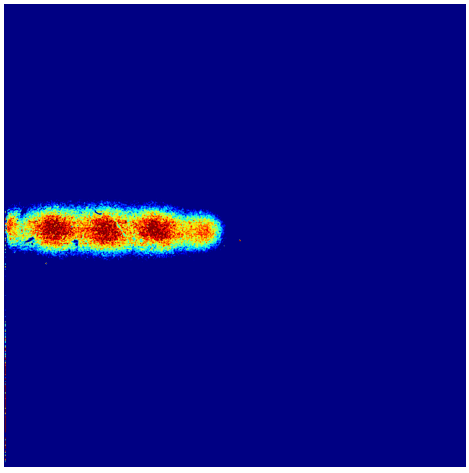

Figure 7.11: Film image obtained for 5 source positions at $z = 60$ mm, with y-axis steps of 10 mm. The image obtained for $z = 40$ mm is essentially identical.

Figure 7.11 shows the image recorded on EBT3 Gafchromic film (placed 5 mm below the source) when the source is located 60 mm above the top of the detector (the image obtained when the source is located at $z = 40$ mm is essentially identical, since the source-film distance is also 5 mm). Five horizontal source displacements were evaluated using this method for each value of z; however, only three full source images were obtained at each position. From left to right, only part of the image of the first source position is visible on the image, and the optical density of the last source image is significant lower than the others. Thus, only the three full source images were used for comparison with the source positions tracked by the *HDR BrachyView* probe. Table 7.4 shows the three source positions in the y direction as measured by film and the *HDR BrachyView* probe, for both values of z. The differences between the two methods are up to 0.31 mm for all measured source positions.

Table 7.4: Measured position of source in y direction, as measured by EBT3 film placed 5 mm from the source and the *HDR BrachyView* probe. The height listed in the table is measured from the bottom of the phantom.

	Measured distance of source centre from the edge of the phantom (mm)		
Height (mm)	Film	*HDR BrachyView*	Difference
25	9.96	10.05	-0.09
	19.60	19.87	-0.27
	29.68	29.86	-0.18
45	9.71	9.9	-0.19
	19.73	19.84	-0.11
	29.38	29.69	-0.31

7.3.4 Discussion

The measurement of the source position when the source was placed at a nominal height of 60 mm above the detector plane demonstrates the performance of the *HDR BrachyView* probe in terms of source tracking accuracy and consistency in the worst case for both sensitivity and minification. Standard deviations of less than 1 mm

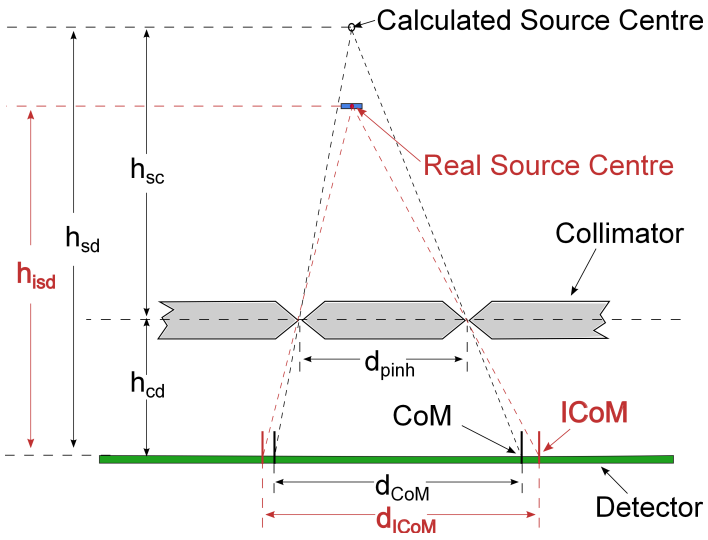

Figure 7.12: Illustration of the calculation of z, demonstrating the overestimation in z that results from using centres of mass of non-uniform-intensity source projections on the imaging plane.

were obtained for all evaluated source positions within a 1 s acquisition time using a 19.5 $mGyh^{-1}m^2$ source (equivalent to an acquisition time of 0.5 s for a full strength source). The increase in standard deviation of measurements with increased source-detector distance is expected, since increasing this distance results in a smaller number of photons being collected within the fixed acquisition period, reducing the signal to noise ratio in the calculation of the projection's CoM. In addition, the magnification of random error during the pinhole imaging reconstruction is also proportional to the distance between the source and the pinhole centres. However, in therapeutic practice, the dwell time of the source is usually much longer than 0.5 s; therefore, this uncertainty will be reduced when the probe is put into clinical use. The accuracy obtained in these experiments closely matched the performance obtained from the simulation studies presented in Chapter 6, although the errors are somewhat larger due to source positioning uncertainties which are not present in the simulation.

Several factors contribute to the error in the estimated position in the z direction. Firstly, although the phantom itself is solid, and therefore the channel in which the

catheter is inserted is rigid, there could be a small difference between the diameter of the channel and the diameter of the catheter. Due to the position of the afterloader relative to the phantom, a small downward force is exerted on the external part of the catheter, which is greater at (nominal) $z = 60$ mm than for $z = 40$ mm. This force results in the catheter being deflected into an approximately parabolic shape inside the channel through the phantom. The central region of the catheter is deflected upward, while the catheter is deflected downward at both the tip of the catheter and at the point of entrance to the phantom. This partially explains the discrepancy between the planned and measured values of z at the nominal height of $z = 60$ mm, rather than being a measurement error, it is an error in the accuracy of the experimental configuration, which is being correctly measured by *HDR BrachyView* system. In particular, the first position of the source appears to have been partially outside the volume of the phantom (confirmed by the images obtained on Gafchromic film, which will be discussed at the end of this Section), and therefore subjected to a greater bend in the catheter, resulting in the offset in z of approximately -2 mm for nominal $z = 60$ mm. The problem of the bend in the catheter is much less significant for other source positions deep inside the catheter hole when nominal $z = 60$ mm and all the source positions when nominal $z = 40$ mm.

The remainder of the error (at both $z = 60$ mm and $z = 40$ mm) is a consequence of the fact that the centre of mass (CoM) of the projection is not precisely collinear with the source and pinhole, but rather is shifted slightly both in x and y in the direction of the corresponding pinhole, a phenomenon which was also observed in the simulation study and has been explained in Chapter 6. The shift is due to the source being cylindrical rather than a point source, with photons from the more distant end of the source travelling a greater distance (and arriving at a shallower angle) at the detector plane compared to photons emitted from the near end. Because of the difference

in path distances, the *intensity* (but not the *geometry*) of projections of a cylindrical source with uniform activity distribution oriented parallel to the detector plane will be non-uniform. The CoM will therefore be biased in the direction of maximum projection intensity (in the direction of the pinhole) and will not perfectly coincide with the true 'ideal' geometric centre of the projection (CoM_i). For projections closest to the source, this effect is further exaggerated by the background of photons which penetrate the body of the collimator directly under the source.

As can be seen from Figure7.12, the error resulting from the use of the projection CoM to estimate the geometric centre of the projection causes an overestimation of the height of the source (i.e., a positive error in z). This error is smallest for the projections nearest to the source in x and y, progressively increasing in the more distant projections. Currently, all projections are equally weighted during the position reconstruction process (with the estimated position being calculated as the point with minimum mean squared distance from all backprojected lines). Therefore, position estimates for those source positions from which a larger number of distant projections are visible will be more severely degraded by this error than those from which only a few nearby projections can be seen. This explains the apparently paradoxical result that source positions above the middle of the detector array, from which multiple projections are visible, accumulate a greater positive bias in height estimation compared to source positions near either end of the detector array, which effectively give more weight to the projection with a smaller error between projection CoM and the true geometric centre of the projection. The same error was observed in the Monte Carlo simulation study discussed in Chapter 6, confirming that it is a consequence of the simplified methods used to estimate the geometric centre of the projection from the projection's CoM.

This latter source of error will be reduced in future versions of the reconstruction

software, by using a non-equal weighting of projections (preferentially weighting the brighter projections, which also gives greater weight to projections with higher SNR). It will also be possible to improve the localisation of the geometric centre of the projection by deconvolving the projection by the point spread function of the pinhole (which will reduce blurring, although it cannot eliminate the effect of photon penetration through the collimator) and iterative post-segmentation intensity correction (i.e., following initial segmentation and approximate determination of the CoMs and hence source position, the intensity of the projection can be corrected for the $1/d^2$ reduction in intensity, after which the CoM should be equal to the geometric centre of the projection).

It is also noted that there is some variation in y between individual runs of the experiment; this is due to the afterloader's own intrinsic positioning error of ± 1 mm (95% confidence interval). Incremental movements in y during each individual run remain highly consistent, but due to mechanical backlash in the afterloader's actuator following the complete retraction and reinsertion of the source, combined with slight differences in catheter insertion between runs, small, random inter-run translations in y are observed.

The intrinsic accuracy of *HDR BrachyView* (i.e., independent of afterloader positioning error) in the y direction was further evaluated using Gafchromic films. Excellent agreement is observed from the results of film and *HDR BrachyView* probe. The difference in y displacement between the measurements by film and the *HDR BrachyView* probe is significantly smaller than the error between the estimated and planned source positions. This is further confirmation that the catheter shift or afterloader positioning uncertainty are the main reason for the differences between planned and estimated source position in the y direction shown in Tables 7.2 and 7.3. Furthermore, the incomplete projection of the first source position in the film image confirms

that the first source position is partly outside the phantom, which was observed in the results plotted in Figure 7.10.

7.4 Conclusion

In this Chapter, a feasibility study was performed for *HDR BrachyView* with a planar collimator combined with single Timepix detector, and the results of the experimental evaluation of *HDR BrachyView* probe in term of source tracking accuracy have been presented.

The result of the initial experimental work demonstrated that the design is capable of tracking the HDR source within a sub-second acquisition time. The source was moved parallel to the detector plane with a source-collimator distance of 43 mm, the maximum (worst-case) distance during HDR prostate brachytherapy treatment. Projection frames demonstrate the accurate resolution of source position in the detector plane within a sub-second dwell time.

The experimental evaluation of the prototype confirmed that most planned source positions (more than 90%) could be measured with an sub-millimetre accuracy in an equivalent acquisition time of 0.5 s for a full strength HDR source, with the largest difference found between planned and measured source position being 2.1 mm (although part of that error is a result of uncertainties in the mechanical positioning of the source). The overall performance, including a systemic overestimation of the source height, was in good agreement with the results of the previous GEANT4 simulation study, and can potentially be improved through more sophisticated image processing techniques. A fully-populated four-detector prototype with integrated trans-rectal ultrasound is currently under development, which will be able to register the calculated source position with the prostate volume.

Chapter 8

Conclusion and Future Work

An in-body source tracking system (*HDR BrachyView*) which can be used to perform intra-fraction quality assurance for HDR prostate brachytherapy has been successfully developed. Its functionality and source tracking accuracy have been evaluated through simulations and experiments performed using a prototype device with a Plastic Water phantom.

8.1 Conclusion

Chapter 2 presented a thorough literature review, including a general introduction to the prostate and prostate cancer, a review of all major treatment options currently available, the specific treatment modality known as brachytherapy (in particular, high dose rate prostate brachytherapy), and a detailed review of current quality assurance methods used in HDR prostate brachytherapy. In particular, several approaches related to the methods proposed in this Thesis were discussed in detail.

After analysing the limitations of image-based source tracking using out-of-body imaging systems, a novel in-body multi pinhole collimated gamma camera imaging system featuring an ultra high resolution solid state detector array was introduced in

Chapter 3. In the same chapter, the key design parameters of *HDR BrachyView* , including the characteristics of the detector, the material and thickness of the collimator, the shape of pinhole and the coverage of the field of view were investigated, derived analytically and validated using Monte Carlo simulations.

The complete process of source position reconstruction is achieved by a series of software modules developed in Matlab, which are discussed in Chapter 4). Potential problems during the identification and segmentation of source projections, projection grouping, CoM calculation and projection-to-pinhole matching were introduced and the corresponding solutions implemented in the software were presented.

To ensure the safety of placing the high-Z material comprising *HDR BrachyView* 's collimator in the patient's rectum during HDR brachytherapy source delivery, Chapter 5 evaluated the dose enhancement observed at the tissue-tungsten interface resulting from back-scatter radiation caused by irradiation of the tungsten collimator by the ^{192}Ir source. Although the dose enhancement is significant in the region extremely close to the surface of the collimator, it only affects the first 0.5 mm of the tissue side of the interface. Therefore, if the tissue is protected by a 1 mm thick tissue-equivalent plastic shell, as will be the case with the *HDR BrachyView* probe, no dose enhancement will occur in rectal tissue due to the backscattered radiation from *HDR BrachyView* probe. Therefore, *BrachyView* probe is safe for clinical application during the delivery of HDR brachytherapy source.

The design of *HDR BrachyView* was validated by simulations and experiments conducted using a combination of a planar pinhole collimator and single Timepix detector. The system was evaluated in terms of efficiency, positioning uncertainty (i.e. the variance between individual measurements) and accuracy (i.e. the deviation of the positions estimated by *HDR BrachyView* from the known physical position of the source). A more complete prototype of *HDR BrachyView* probe was then constructed

using a cylindrical collimator with a two-detector Timepix array, which was used to perform experimental evaluation of the system under more realistic conditions. For both the prototype systems, results of the simulations and experiments were observed to be in close agreement, and are presented in Chapters 6 and 7. These results demonstrated the ability of *HDR BrachyView* to track the source position with an average sub-millimetre accuracy, within a sub-second acquisition time, as per the original design specifications for the probe.

8.2 Recommendations for Future Work

A number of potential opportunities to improve the performance of the *HDR BrachyView* probe have been identified. The first is to optimise the reconstruction algorithm; a systematic shift in the calculated CoM from its ideal position was observed in both the simulation and experimental studies, which is correlated to the distance between the projection and its corresponding pinhole. Therefore this error could be reduced by using a non-equal weighting of projections (preferentially weighting the brighter projections, which also gives greater weight to projections with higher SNR). It may also be possible to improve the localisation of the geometric centre of an individual projection by deconvolving the projection by the point spread function of its corresponding pinhole (which will reduce blurring, although it cannot eliminate the effect of photon penetration through the collimator). Finally, iterative post-segmentation intensity correction should be able to reduce the systemic shift by compensating for the $\frac{1}{d^2}$ variation in intensity resulting from the range of path lengths of photons emitted by the cylindrical source as they travel to the detector plane. This last point should result in the CoM of the segmented projection to be be equal to the ideal centre of mass of the projection (that is, collinear with the pinhole and the geometric centre of the source).

Another direction for future potential improvement to the *HDR BrachyView* probe is its potential for monitoring the source dwell time. Timepix is capable of capturing up to 400 images per second. Although a short acquisition time will lead to insufficient statistics to accurately track the source position, the difference in response map may still be enough to measure source movement. Thus, a comprehensive evaluation of methods to evaluate source transit with *HDR BrachyView* would be interesting.

Finally, the ultimate objective of the project is real-time correction of treatment plans during treatment; once the trans-rectal ultrasound probe is fully integrated, it will be necessary to develop plug-ins to treatment planning systems to enable them to utilise the information provided by *HDR BrachyView* .

References

[1] E. Marieb and K. Hoehn. *Human Anatomy & Physiology, 7th edition.* Pearson Benjamin Cummings, 2007.

[2] F. Martini, M. Timmons, and R. Tallitsch. *Human Anatomy, 7th edition.* Pearson Benjamin Cummings, 2012.

[3] A.J. Costello, B.W. Dowdle, B. Namdrian, J. Pederden, and D.G. Murphy. Immunohistochemical study of the cavernous nerves in the periprostatic region. *BJU Int.*, 107(8):1210–1215, April 2011.

[4] J. Cheng, J. Dai, Y. Liu, H. Hong, X. Zhang, and Q. Ye. Anatomic observation of the prostate for clinical application of local drug injection through the rectum for chronic prostatitis. *Di Yi Jun Yi Da Xue Xue Bao*, 23(6):633–635, 2003.

[5] S. Rasmussen and P. Riis. Rectal wall thickness measured by ultrasound in chronic inflammatory diseases of the colon. *Scand. J. Gastroenterol.*, 20(1):109–114, 1985.

[6] S.R. Denmeade and J.T. Isaacs. A history of prostate cancer treatment. *Nat. Rev. Cancer*, 2(5):389–395, May 2002.

[7] Australian Institute of Health and Welfare. *Australian Cancer Incidence & Mortality Books*, volume Prostate cancer. AIHW:Canberra, 2014.

[8] R. Siegel, J. Ma, Z. Zou, and A. Jemal. Cancer statistics, 2014. *CA. Cancer J. Clin.*, 64(1):9–29, 2014.

[9] B.S. Carter, T.H. Beaty, G.D. Steinberg, B. Childs, and P.C. Walsh. Mendelian inheritance of familial prostate cancer. *Proc. Natl. Acad. Sci. U. S. A.*, 89(8):3367–3371, April 1992.

[10] O. Bratt. Hereditary prostate cancer: clinical aspects. *J. Urol.*, 3:906–913, September 168.

[11] G. Wilding. The importance of steroid hormones in prostate cancer. *Cancer Surv.*, 14:113–130, 1992.

[12] C. F. Heyns, M. Fisher, A. Lecuona, and A. Merwe. Prostate cancer among different racial groups in the western cape: Presenting features and management. *S. Afr. Med. J.*, 101(4):267–270, 2011.

[13] A. Jemal, F. Bray, M.M. Center, J. Ferlay, E. Ward, and D. Forman. Global cancer statistics. *CA. Cancer J. Clin.*, 61(2):69–90, March/April 2011.

[14] O.W. Brawley, A.B. Jani, and V. Master. Prostate cancer and race. *Curr. Probl. Cancer*, 31:211–225, May/June 2007.

[15] R.J. Maclnnis and D.R. English. Body size and composition and prostate cancer risk: systematic review and meta-regression analysis. *Cancer Causes Control*, 17(8):989–1003, 2006.

[16] T. Mistry, J. Digby, K. Desai, and H. Randeva. Obesity and prostate cancer: a role for adipokines. *Eur. Urol.*, 52(1):46–53, July 2007.

[17] D.M. Freedman, M. Dosemeci, and K. McGlynn. Sunlight and mortality from breast, ovarian, colon, prostate, and non-melanoma skin cancer: a composite

death certificate based case-control study. *Occup. Environ. Med.*, 59(4):257–262, 2002.

[18] G.P. Studzinski and D.C. Moore. Sunlight–can it prevent as well as cause cancer? *Cancer Res.*, 55(18):4014–4022, September 1995.

[19] D. Bodiwala, C.J. Luscombe, S. Liu, M. Saxby, M. French, P.W. Jones, A.A. Fryer, and R.C. Strange. Prostate cancer risk and exposure to ultraviolet radiation: further support for the protective effect of sunlight. *Cancer Lett.*, 192(2):145–149, 2003.

[20] C. Luscombe, M. French, S. Liu, M. Saxby, P. Jone, and A. Fryer. Prostate cancer risk: associations with ultraviolet radiation, tyrosinase and melanocortin-1 receptor genotypes. *Br. J. Cancer*, 85(10):1504–1509, November 2001.

[21] S. Manolagas. Vitamin d and its revelance to cancer. *Anticancer Res.*, 7(4A):625–638, 1987.

[22] G. Schwartz and B. Hulka. Is vitamin d deficiency a risk factor for prostate cancer? (hypothesis). *Anticancer Res.*, 10(5A):1307–1311, September/Octpber 1990.

[23] R. Gilbert, R.M. Martin, R. Beynon, R. Harris, J. Savovic, L. Zuccolo, G.E. Bekkering, W.D. Fraser, J.A.C. Sterne, and C. Metcalfe. Associations of circulating and dietary vitamin d with prostate cancer risk: a systematic review and dose-response meta-analysis. *Cancer Causes Control*, 22(3):319–340, 2011.

[24] S. Frankel, G.D. Smith, J. Donovan, and D. Neal. Screening for prostate cancer. *Lancet*, 361(9363):1122–1128, March 2003.

[25] B. Djavan, A. Kazzazi, L. Dulabon, M. Margreiter, A. Farr, M.J. Handl, and H. Lepor. Diagnostic strategies for prostate cancer. *Eur. Urol., Supp.*, 10(3):e26–e37, 2011.

[26] W. Kutscher and H. Wolbergs. Prostata phosphatase. *Hoppe. Seylers Z. Physiol. Chem.*, pages 236–237, 1935.

[27] E.J. King and K.A. Jegatheesan. A method of the determination of tartrate-labile prostatic acid phosphatase in serum. *J. Clin. Pathol.*, 12(1):85, January 1959.

[28] T.J. Sullivan. *Theory and application of the serum" acid" phosphatase determination in metastasizing prostatic carcinoma: early effects of castration.* PhD thesis, Williams and Wilkins Company, 1943.

[29] R. Nesbit and W. Baum. Serum phosphatase determination in diagnosis of prostatic cancer. a review of 1,150 cases. *JAMA*, 145(17):1321–1324, April 1951.

[30] L.D. Papsidero, M. Wang, L.A. Valenzuela, G.P. Murphy, and T.M. Chu. A prostate antigen in sera of prostatic cancer patients. *Cancer Res.*, 40:2428–2432, July 1980.

[31] E. Lalani, M. Laniado, and P. Abel. Molecular and cellular biology of prostate cancer. *Cancer Metastasis Rev.*, 16(1-2):29–66, 1997.

[32] M.J. Barry. Prostate-specific–antigen testing for early diagnosis of prostate cancer. *N. Engl. J. Med.*, 344(18):1373–1377, May 2001.

[33] I.M. Thompson, D.K. Pauler, M.S. Lucia P.J. Goodman, C.M. Tangen, H.L. Parnes, L.M. Minasian, L.G. Ford, S.M. Lippman, E.D. Crawford, J.J. Crowley,

and C. A. Coltman. Prevalence of prostate cancer among men with a prostate-specific antigen level $\leq$ 4.0 ng per milliliter. *N. Engl. J. Med.*, 350(22):2239–2246, May 2004.

[34] P. Beatty and A. Glaser. Prostate cancer with low psa levels. *N. Engl. J. Med.*, 351:1802–1803, October 2004.

[35] H. Backer. Prostate cancer screening: Exploring the debate. *Perm. J.*, 3(3):30–40, 1999.

[36] C. Becker and H Lilja. Individual prostate-specific antigen (psa) forms as prostate tumor markers. *Clin. Chim. Acta*, 257(1):117–132, 1997.

[37] F. Labrie, A. Dupont, R. Suburu, L. Cusan, M. Tremblay, J.L. Gomez, and J. Emond. Serum prostate specific antigen as pre-screening test for prostate cancer. *J. Urol.*, 147(3 Pt 2):846–851, 1992.

[38] W. Cooner, B. Mosley, C.L. Rutherford, J.H. Beard, H.S. Pond, W.J. Terry, T.C. Igel, and D.D. Kidd. Prostate cancer detection in a clinical urological practice by ultrasonography, digital rectal examination and prostate specific antigen. *J. Urol.*, 167(2):966–974, February 2002.

[39] S. Selley, J. Donovan, A. Faulkner, J. Coast, and D. Gillatt. Diagnosis, management and screening of early localised prostate cancer. *Health Technol. Assess.*, 1(2):i:1–96, 1997.

[40] Saint Francis / Mount Sinai Regional Cancer Centre. Online; available URL: `https://saintfranciscare.com/saintfrancisdoctors/cancercenter/nci/CancerSummary.aspx?id=CDR62965.xml`. Last Accessed: 2015-03-21.

[41] N. Borley and M.R. Feneley. Prostate cancer: diagnosis and staging. *Asian J. Androl.*, 11:74–80, 2009.

[42] M.T. Ismail and L.G. Gomella. Transrectal prostate biopsy. *Urol. Clin. North Am.*, 40(4):457–472, November 2013.

[43] D.F. Gleason, G.T. Mellinger, Veretans Administration Cooperative Urological Research Group, et al. Prediction of prognosis for prostatic adenocarcinoma by combined histological grading and clinical staging. *J. Urol.*, 167(2):953–958, February 2002.

[44] D.F. Gleason. Histologic grading of prostate cancer: A perspective. *Hum. Pathol.*, 23(3):273–279, March 1992.

[45] J.I. Epstein, W.C. Allsbrook Jr, M.B. Amin, L.L. Eqevad, and ISUP Grading Committee. The 2005 international society of urological pathology (isup) consensus conference on gleason grading of prostatic carcinoma. *Am. J. Surg. Pathol.*, 29(9):1228–1242, September 2005.

[46] C.K. Gjertson and P.C. Albertsen. Use and assessment of psa in prostate cancer. *Med. Clin. North Am.*, 95(1):191–200, January 2011.

[47] J. Mohler, R. Bahnson, B. Boston, and etc. Nccn clinical practice guidelines in oncology: prostate cancer early detection. *J. Natl. Compr. Canc. Netw.*, 8(2):240–262, February 2010.

[48] J. Warmkessel. *Contemporary Issues in Prostate Cancer: A Nursing Perspective, Second Edition*. Jones and Bartlett, 2005.

[49] American Joint Committee on Cancer. *AJCC Cancer Staging Manual*. Springer, 2002.

[50] M. Roach, J. Lu, M.V. Pilipech, S.O. Asbell, M. Mohuidden, R. Terry, and D. Grignon. Four prognostic groups predict long-term survival from prostate

cancer following radiotherapy alone on radiation therapy oncology group clinical trials. *Int. J. Radiat. Oncol. Biol. Phys.*, 47(3):609–615, June 2000.

[51] S. Sriprasad, M.R. Feneley, and P.M. Thompson. History of prostate cancer treatment. *Surg. Oncol.*, 18(3):185–191, September 2009.

[52] T. Millin. Retropubic prostatectomy, a new extravesical technique: report on 20 cases. *Lancet*, 246(6379):693–696, December 1945.

[53] D.I. Lee. Robotic prostatectomy: what we have learned and where we are going. *Yonsei Med. J.*, 50:177–181, April 2009.

[54] A. Krongrad. Laparoscopic radical prostatectomy. *Curr. Urol. Rep.*, 1(1):36–40, 2000.

[55] T.M. Webster, S.D. Herrell, S.S. Chang, M.S. Cookson, R.G. Baumgartner, L.W. Anderson, and J.A. Smith. Robotic assisted laparoscopic radical prostatectomy versus retropubic radical prostatectomy: a prospective assessment of postoperative pain. *J. Urol.*, 174(3):912–914, September 2005.

[56] T. Bivalacqua, P. Pierorazio, and L. Su. Open, laparoscopic and robotic radical prostatectomy: optimizing the surgical approach. *Surg. Oncol.*, 18(3):233–241, 2009.

[57] J. Smith, R. Chan, and S. Chang. A comparison of the incidence and location of positive surgical margins in robotic assisted laparoscopic radical prostatectomy and open retropubic radical prostatectomy. *J. Urol.*, 178(6):2385–2390, December 2007.

[58] S. R. Denmeade and J. T. Isaacs. *Cancer Medicine 5th.* B C. Decker Inc., 2000.

[59] F. Labrie, A. Dupont, A. Belanger, L. Cusan, Y. Lacourciere, G. Monfette, J.G. Laberge, J.P. Emond, A.T. Fazekas, J.P. Raynaud, et al. New hormonal therapy in prostatic carcinoma: combined treatment with an lhrh agonist and an antiandrogen. *Clin. Invest. Med.*, 5(4):267–275, 1982.

[60] G. Tolis, D. Ackman, A. Stellos, A. Mehta, F. Labrie, A.T. Fazekas, A.M. Comaru-Schally, and A.V. Schally. Tumor growth inhibition in patients with prostatic carcinoma treated with lutenizing hormonereleasing hormone agonists. *Proc. Natl. Acad. Sci. U. S. A.*, 79(5):1658–1662, March 1982.

[61] P. Metcalfe, T. Kron, and P. hoban. *The Physics of Radiotherapy X-Rays and Electrons*. Medical Physics Publishing, 2007.

[62] E.J. Hall and A.J. Giaccia. *Radiobiology for the Radiologist*. Lippincott Williams & Wilkins, 2006.

[63] R. Hill, B. Healy, L. Holloway, Z. Kuncic, D. Thwaites, and C. Baldock. Advances in kilovoltage x-ray beam dosimetry. *Phys. Med. Biol.*, 59(6):R183–R231, 2014.

[64] G.E. Hanks, K.L. Martz, and J.J. Diamond. The effect of dose on local control of prostate cancer. *Int. J. Radiat. Oncol. Biol. Phys.*, 15(6):1299–1305, December 1988.

[65] M.J. Zelefsky, Z. Fuks, M. Hunt, H.J. Lee, D. Lombardi, C.C. Ling, V. Reuter, E.S. Venkatraman, and S.A. Leibel. High dose radiation delivered by intensity modulated conformal radiotherapy improves the outcome of localized prostate cancer. *J. Urol.*, 166(3):876–881, September 2001.

[66] A. Pollack, G.K. Zagars, G. Starkschall, J.A. Antolak, J.J. Lee, E. Huang, A.C von Eschenbach, D.A. Kuban, and I. Rosen. Prostate cancer radiation dose

response: results of the md anderson phase iii randomized trial. *Int. J. Radiat. Oncol. Biol. Phys.*, 53(5):1097–1105, August 2002.

[67] A.L. Zietman, M.L. DeSilvio, J.D. Slater, C.J. Rossi, D.W. Miller, J.A. Adams, and W.U. Shipley. Comparison of conventional-dose vs high-dose conformal radiation therapy in clinically localized adenocarcinoma of the prostate: a randomized controlled trial. *JAMA*, 294(10):1233–1239, September 2005.

[68] A.L. Zietman, K. Bae, J.D. Slater, W.U. Shipley, J.A. Efstathiou, J.J. Coen, D.A. Bush, M. Lunt, D.Y. Spiegel, R. Skowronski, B.R. Jabola, and C.J. Rossi. Randomized trial comparing conventional-dose with high-dose conformal radiation therapy in early-stage adenocarcinoma of the prostate: long-term results from proton radiation oncology group/american college of radiology 95-09. *J. Clin. Oncol.*, 28(7):1106–1111, March 2010.

[69] G.A. Viani, L.G. da Silva, and E.J. Stefano. High-dose conformal radiotherapy reduces prostate cancer-specific mortality: results of a meta-analysis. *Int. J. Radiat. Oncol. Biol. Phys.*, 83(5):e619–e625, August 2012.

[70] T.M. Pisansky, D.G. Gold, K.M. Furutani, O.K. Macdonald, R.H. McLaren, L.A. Mynderse, T.M. Wilson, J.R. Hebl, and R. Choo. High-dose-rate brachytherapy in the curative treatment of patients with localized prostate cancer. *Mayo Clin. Proc.*, 83(12):1364–1372, December 2008.

[71] M. Ferrer, J.F. Suárez, F. Guedea, P. Fernández, V. Macías, A. Mariño, A. Hervas, I. Herruzo, M. Ortiz, H. Villavicencio, et al. Health-related quality of life 2 years after treatment with radical prostatectomy, prostate brachytherapy, or external beam radiotherapy in patients with clinically localized prostate cancer. *Int. J. Radiat. Oncol. Biol. Phys.*, 72(2):421–432, 2008.

[72] M. Fatyga, J.F. Williamson, N. Dogan, D. Todor, J.V. Siebers, R. George, I. Barani, and M. Hagan. A comparison of hdr brachytherapy and imrt techniques for dose escalation in prostate cancer: A radiobiological modeling study. *Med. Phys.*, 36(9):3995–4006, September 2009.

[73] J. Hermesse, S. Biver, N. Jansen, E. Lenaerts, N. De Patoul, S. Vynckier, P. Coucke, P. Scalliet, and P. Nickers. A dosimetric selectivity intercomparison of hdr brachytherapy, imrt and helical tomotherapy in prostate cancer radiotherapy. *Strahlenther. Onkol.*, 185(11):736–742, 2009.

[74] G.C. Morton and P.J. Hoskin. Brachytherapy: Current status and future strategies—can high dose rate replace low dose rate and external beam radiotherapy? *Clin. Oncol.*, 25(8):474–482, August 2013.

[75] A. Challapalli, E. Jones, C. Harvey, G.O. Hellawell, and S.A. Mangar. High dose rate prostate brachytherapy: an overview of the rationale, experience and emerging applications in the treatment of prostate cancer. *Br. J. Radiol.*, 85:s18–s27, 2014.

[76] C. Shah, T.B. Lanni Jr, M.I. Ghilezan, G.S. Gustafson, K.S. Marvin, H. Ye, F.A. Vicini, and A.A. Martinez. Brachytherapy provides comparable outcomes and improved cost-effectiveness in the treatment of low/intermediate prostate cancer. *Brachytherapy*, 11(6):441–445, November/December 2012.

[77] C. Kirisits, M.J. Rivard, D. Baltas, F. Ballester, M. De Brabandere, R. van der Laarse, Y. Niatsetski, P. Papagiannis, T.P. Hellebust, J. Perez-Calatayud, K. Tanderup, and F.A. Siebert J.L.M. Venselaarm. Review of clinical brachytherapy uncertainties: Analysis guidelines of gec-estro and the aapm. *Radiother. Oncol.*, 110(1):199–212, January 2014.

[78] Varian Medical Systems. *Varisource afterloader feature sheet*, 06 2014.

[79] Elekta AB. *microSelectron digital brachytherapy afterloading platform*, 2014.

[80] R.J.M. Elfrink, I.K.K. Kolkman-Deurloo, H.J. Kleffens, A. Rijnders, B. Schaeken, T.H.L. Aalbers, W.J.F. Dries, and J.L.M. Venselaar. Determination of the accuracy of implant reconstruction and dose delivery in brachytherapy in the netherlands and belgium. *Radiother. Oncol.*, 59(3):297–306, 2001.

[81] A. Manikandan, S. Biplab, P.A. David, R. Holla, T.R. Vivek, and N. Sujatha. Relative dosimetrical verification in high dose rate brachytherapy using two-dimensional detector array imatrixx. *J. Med. Phys.*, 36(3):171, July/September 2011.

[82] P. Kohr and F.A. Siebert. Quality assurance of brachytherapy afterloaders using a multi-slit phantom. *Phys. Med. Biol.*, 52(17):N387, 2007.

[83] T.P. Hellebust, K. Tanderup, E.S. Bergstrand, B.H. Knutsen, J. Røislien, and D.R. Olsen. Reconstruction of a ring applicator using ct imaging: impact of the reconstruction method and applicator orientation. *Phys. Med. Biol.*, 52(16):4893, 2007.

[84] D. Waid, J. Morrison, and G. Glennie. Su-ff-t-30: Commissioning the ring & tandem combination applicator set-ct & mr compatible, for clinical use with the varisource hdr unit. *Med. Phys.*, 36(6):2525–2525, 2009.

[85] R. Stern and T. Liu. Dwell position inaccuracy in the varian gammamed hdr ring applicator. *J. Appl. Clin. Med. Phys.*, 11(4):291–296, Fall 2010.

[86] A. Q. Jangda, S. Hussein, and Z. Rehman. A new approach to measure dwell position inaccuracy in hdr ring applicators-quantification and corrective qa. *J. Appl. Clin. Med. Phys.*, 12(1):3–13, September 2011.

[87] R. McMahon, T. Zhuang, B.A. Steffey, H. Song, and O.I. Craciunescu. Commissioning of varian ring & tandem hdr applicators: reproducibility and interobserver variability of dwell position offsets. *J. Appl. Clin. Med. Phys.*, 12(4):50–62, Fall 2011.

[88] D. Berger, J. Dimopoulos, R. Pötter, and C. Kirisits. Direct reconstruction of the vienna applicator on mr images. *Radiother. Oncol.*, 93(2):347–351, July 2009.

[89] P.J. Hoskin, P.J. Bownes, P. Ostler, K. Walker, and L. Bryant. High dose rate afterloading brachytherapy for prostate cancer: catheter and gland movement between fractions. *Radiother. Oncol.*, 68(3):285–288, 2003.

[90] T. Simnor, S. Li, G. Lowe, P. Ostler, L. Bryant, C. Chapman, D. Inchley, and P.J. Hoskin. Justification for inter-fraction correction of catheter movement in fractionated high dose-rate brachytherapy treatment of prostate cancer. *Radiother. Oncol.*, 93(2):253–258, November 2009.

[91] A.A. Martinez, I. Pataki, G. Edmundson, E. Sebastian, D. Brabbins, and G. Gustafson. Phase ii prospective study of the use of conformal high-dose-rate brachytherapy as monotherapy for the treatment of favorable stage prostate cancer: a feasibility report. *Int. J. Radiat. Oncol. Biol. Phys.*, 49(1):61–69, January 2001.

[92] J.D. Kiffer, W.A. Schumer, C.A. Mantle, B.J. McKenzie, M. Feigen, G.G. Quong, and F.M. Waterman. Impact of oedema on implant geometry and dosimetry for temporary high dose rate brachytherapy of the prostate. *Australas. Radiol.*, 47(2):172–176, June 2003.

[93] Y. Kim, I.C. Hsu, E. Lessard, J. Vujic, and J. Pouliot. Dosimetric impact of prostate volume change between ct-based hdr brachytherapy fractions. *Int. J. Radiat. Oncol. Biol. Phys.*, 59(4):1208–1216, July 2004.

[94] F.L. Cury, M. Duclos, A. Aprikian, H. Patrocinio, and L. Souhami. Prostate gland edema after single-fraction high-dose rate brachytherapy before external beam radiation therapy. *Brachytherapy*, 9(3):208–212, July/September 2010.

[95] N. Kovalchuk, K.M. Furutani, O.K. MacDonald, and T.M. Pisansky. Dosimetric effect of interfractional needle displacement in prostate high-dose-rate brachytherapy. *Brachytherapy*, 11(2):111–118, March/April 2012.

[96] A.M. Dinkla, B.R. Pieters, K. Koedooder, N. van Wieringen, R. van der Laarse, and A. Bel. Prostate volume and implant configuration during 48 hours of temporary prostate brachytherapy: limited effect of oedema. *Radiat. Oncol.*, 9(1):272, 2014.

[97] S.J. Damore, A.M.N. Syed, A.A. Puthawala, and A. Sharma. Needle displacement during hdr brachytherapy in the treatment of prostate cancer. *Int. J. Radiat. Oncol. Biol. Phys.*, 46(5):1205–1211, 2000.

[98] E. Mullokandov and G. Gejerman. Analysis of serial ct scans to assess template and catheter movement in prostate hdr brachytherapy. *Int. J. Radiat. Oncol. Biol. Phys.*, 58(4):1063–1071, March 2004.

[99] Y. Kim, I. Hsu, and J. Pouliot. Measurement of cranio-caudal catheter displacement between fractions in ct-based hdr brachytherapy of prostate cancer. *J. Appl. Clin. Med. Phys.*, 8(4):1–13, 2007.

[100] M. Whitaker, G. Hruby, A. Lovett, and N. Patanjali. Prostate hdr brachytherapy catheter displacement between planning and treatment delivery. *Radiother. Oncol.*, 101(3):490–494, December 2011.

[101] P. Ortiz. Lessons learned form accidental exposures in radiotherapy. *IAEA Safety Reports Series*, 17:59–61, 2000.

[102] I.J. Das, C. Cheng, R.J. Watts, A. Ahnesjö, J.Gibbons, X. Li, J. Lowenstein, R.K. Mitra, W.E. Simon, and T.C. Zhu. Accelerator beam data commissioning equipment and procedures: report of the tg-106 of the therapy physics committee of the aapm. *Med. Phys.*, 35(9):4186–4215, September 2008.

[103] Z. Li, T.P. Mitchell, J.R. Palta, and C. Liu. A quality assurance test tool for high dose-rate remote afterloading brachytherapy units. *Med. Phys.*, 25(2):232–235, February 1998.

[104] A. Espinoza, B. Beeksma, M. Petasecca, I. Fuduli, C. Porumb, D. Cutajar, S. Corde, M. Jackson, M.L.F. Lerch, and A.B. Rosenfeld. The feasibility study and characterization of a two-dimensional diode array in "magic phantom" for high dose rate brachytherapy quality assurance. *Med. Phys.*, 40(11):111702, November 2013.

[105] D.A. Wilkinson. High dose rate (hdr) brachytherapy quality assurance: a practical guide. *Biomed. Imaging. Interv. J.*, 2(2):1–7, 2006.

[106] R.J.M. Elfrink, H.J. van kleffens, I.K.K. Kolkman-Deurloo, A.H.L. Aalbers, W.J.F. Dries, A. Rijnders, B. Schaeken, and J.L.M. Venselaar. Quality control in brachytherapy. Technical Report 13, Netherlands Commission on Radiation Dosimetry, Task Group Quality Control in Brachytherapy, 2000.

[107] F. Bochud, B. Leemann, R. Linder, R. Moeckli, K. Munch, H. Nemec, M. Sassowsky, and G. Stucki. Dosimetry and quality assurance in high dose rate brachytherapy with iridium-192. Technical Report 13, Swiss Society for Radiobiology and Medical Physics, january 2005.

[108] J.F. Williamson. Current brachytherapy quality assurance guidance: Does it meet the challenges of emerging image-guided technologies? *Int. J. Radiat. Oncol. Biol. Phys.*, 71(1):S18–S22, May 2008.

[109] C. Dempsey, R. Smith, T. Nyathi, A. Ceylan, L. Howard, V. Patel, R. Das, and A. Haworth. Acpsem brachytherapy working group recommendations for quality assurance in brachytherapy. *Australas. Phys. Eng. Sci. Med.*, 36(4):387–396, December 2013.

[110] G.J. Kutcher, L. Coia, M. Gillin, W.F. Hanson, S. Leibel, R.J. Morton, J.R. Palta, J.A. Purdy, L.E. Reinstein, G.K. Svensson, M. Weller, and L. Wingfield. Comprehensive qa for radiation oncology: report of aapm radiation therapy committee task group 40. *Med. Phys.*, 21:581–581, April 1994.

[111] M.A. Gadhi, S.A. Buzdar, M. Afzal, Sh. Fatmi, M.S. Akhtar, and A.H. Nizamani. Calibration of iridium-192 source by ionization chamber for high dose rate brachytherapy. *Int. J. Radiat. Res.*, 11(3):189–193, July 2013.

[112] T.P. Loftus. Standardization of iridium-192 gamma-ray sources in terms of exposure. *J. Res. Nat. Bur. Stand*, 85(1):19–25, January/February 1980.

[113] S. J. Goetsch, F. H. Attix, D. W. Pearson, and B. R B. R. Thomadsen. Calibration of 192Ir high-dose-rate afterloading systems. *Med. Phys.*, 18(3):462–467, 1991.

[114] S. J. Goetsch, F. H. Attix, L. A. DeWerd, and B. R. Thomadsen. A new re-entrant ionization chamber for the calibration of iridium-192 high dose rate sources. *Int. J. Radiat. Oncol. Biol. Phys.*, 24(1):167–170, 1992.

[115] N . Reynaert, F. Verhaegen, and H. Thierens. In-water calibration of pdr 192ir brachytherapy sources with an ne2571 ionization chamber. *Phys. Med. Biol.*, 43(8):2095–2107, 1998.

[116] L.A. DeWerd, P. Jursinic, R. Kitchen, and B.R. Thomadsen. Quality assurance tool for high dose rate brachytherapy. *Med. Phys.*, 22(4):435–440, April 1995.

[117] A.S. Kirov, J.F. Williamson, A.S. Meigooni, and Y. Zhu. Tld, diode and monte carlo dosimetry of an 192ir source for high dose-rate brachytherapy. *Phys. Med. Biol.*, 40(12):2015–2036, 1995.

[118] P. Karaiskos, A. Angelopoulos, L. Sakelliou, P. Sandilos, C. Antypas, L. Vlachos, and E. Koutsouveli. Monte carlo and tld dosimetry of an 192ir high dose-rate brachytherapy source. *Med. Phys.*, 25(10):1975–1984, October 1998.

[119] K.R. Russell and A. Ahnesjö. Dose calculation in brachytherapy for a source using a primary and scatter dose separation technique. *Phys. Med. Biol.*, 41(6):1007, 1996.

[120] A.S. Meigooni, J.A. Meli, and R. Nath. Influence of the variation of energy spectra with depth in the dosimetry of 192ir using lif tld. *Phys. Med. Biol.*, 33(10):1159, 1988.

[121] A. Niroomand-Rad, C.R. Blackwell, B.M. Coursey, K.P. Gall, J.M. Galvin, W. McLaughlin, A.S. Meigooni, R. Nath, J.E. Rodgers, and C.G. Soares. Radiochromic film dosimetry: recommendations of aapm radiation therapy committee task group 55. *Med. Phys.*, 25(11):2093–2115, 1998.

[122] C.G. Soares. Radiochromic film dosimetry. *Radiat. Meas.*, 41,Supplement 1:S100–S116, December 2006.

[123] D.M. Duggan, C.W. Coffey II, J.L. Lobdell, and M.C. Schell. Radiochromic film dosimetry of a high dose rate beta source for intravascular brachytherapy. *Med. Phys.*, 26(11):2461–2464, November 1999.

[124] J.F. Dempsey, D.A. Low, S. Mutic, J. Markman, A. Kirov, G.H. Nussbaum, and J.F. Williamson. Validation of a precision radiochromic film dosimetry system for quantitative two-dimensional imaging of acute exposure dose distributions. *Med. Phys.*, 27(10):2462–2475, October 2000.

[125] S. Aldelaijan, H. Mohammed, N. Tomic, . H. Liang, F. Deblois, A. Sarfehnia, W. Abdel-Rahman, J. Seuntjens, and S. Devic. Radiochromic film dosimetry of HDR (192)Ir source radiation fields. *Med. Phys.*, 38(11):6074–6083, November 2011.

[126] S.D. Sharma, C. Bianchi, L. Conte, R. Novario, and B.C. Bhatt. Radiochromic film measurement of anisotropy function for high-dose-rate ir-192 brachytherapy source. *Phys. Med. Biol.*, 49(17):4065, 2004.

[127] M.D.C. Evans, C.J. Arsenault, and M.B. Podgorsak. Quality assurance for variable-length catheters with an afterloading brachytherapy device. *Med. Phys.*, 20(1):251–253, Jan/Feb 1993.

[128] D.W. Rickey, D. Sasaki, and J. Bews. A quality assurance tool for high-dose-rate brachytherapy. *Med. Phys.*, 37(6):2525–2532, June 2010.

[129] P. Jursinic. Quality assurance measurements for high-dose-rate brachytherapy without film. *J. Appl. Clin. Med. Phys.*, 15(1):246–261, 2014.

[130] C Austerlitz, H Mota, CE Almeida, R Allison, and C Sibata. Quality assurance of hdr ir192 sources using a fricke dosimeter. *Med. Phys.*, 34(4):1348–1353, April 2007.

[131] V.Z. Zilio, O.P. Joneja, Y. Popowski, A.B. Rosenfeld, and R. Chawla. Absolute depth-dose-rate measurements for an ir192 hdr brachytherapy source in water using mosfet detectors. *Med. Phys.*, 33(6):1532–1539, June 2006.

[132] G. Kertzscher, A.B. Rosenfeld, S. Beddar, K. Tanderup, and J.E. Cygler. In vivo dosimetry: trends and prospects for brachytherapy. *Br. J. Radiol.*, 87(1041), July 2014.

[133] J.M. Fagerstrom, J.A. Micka, and L.A. DeWerd. Response of an implantable mosfet dosimeter to ir192 hdr radiation. *Med. Phys.*, 35(12):5729–5737, December 2008.

[134] Z. Qi, X. Deng, S. Huang, J. Lu, M.L.F. Lerch, D. Cutajar, and A.B. Rosenfeld. Verification of the plan dosimetry for high dose rate brachytherapy using metal-oxide-semiconductor field effect transistor detectors. *Med. Phys.*, 34(6):2007–2013, June 2007.

[135] I. S. Kwan, D. Wilkinson, D. Cutajar, M. Lerch, A. Rosenfeld, A. Howie, J. Bucci, Y. Chin, and V. L. Perevertaylo. The effect of rectal heterogeneity on wall dose in high dose rate brachytherapy. *Med. Phys.*, 36(1):224–232, January 2009.

[136] C. Tenconi, M. Carrara, M. Borroni, A. Cerrotta, D. Cutajar, M. Petasecca, M.L.F. Lerch, J. Bucci, G. Gambarini, E. Pignoli, and A.B. Rosenfeld. Trus-probe integrated mos*kin* detectors for rectal wall in vivo dosimetry in hdr

brachytherapy: in phantom feasibility study. *Radiat. Meas.*, 71:379–383, December 2014.

[137] N. Suchowerska, J. Lambert, T. Nakano, S. Law, J. Elsey, and D.R. McKenzie. A fibre optic dosimeter customised for brachytherapy. *Radiat. Meas.*, 42(4):929–932, April/May 2007.

[138] J. Lambert, T. Nakano, S. Law, J. Elsey, D.R. McKenzie, and N. Suchowerska. In vivo dosimeters for hdr brachytherapy: a comparison of a diamond detector, mosfet, tld, and scintillation detector. *Med. Phys.*, 34(5):1759–1765, May 2007.

[139] L.W. Cartwright, N. Suchowerska, Y. Yin, J. Lambert, M. Haque, and D.R. McKenzie. Dose mapping of the rectal wall during brachytherapy with an array of scintillation dosimeters. *Med. Phys.*, 37(5):2247–2255, May 2010.

[140] N. Suchowerska, M. Jackson, J. Lambert, Y. Yin, G. Hruby, and D.R. McKenzie. Clinical trials of a urethral dose measurement system in brachytherapy using scintillation detectors. *Int. J. Radiat. Oncol. Biol. Phys.*, 79(2):609–615, February 2011.

[141] L. Archambault, T. M. Briere, F. Pönisch, L. Beaulieu, D. A. Kuban, A. Lee, and S. Beddar. Toward a real-time in vivo dosimetry system using plastic scintillation detectors. *Int. J. Radiat. Oncol. Biol. Phys.*, 78(1):280–287, March 2010.

[142] J. Duan, D.J. Macey, P.N. Pareek, and I.A. Brezovich. Real-time monitoring and verification of in vivo high dose rate brachytherapy using a pinhole camera. *Med. Phys.*, 28(2):167–173, February 2001.

[143] M. Batic, J. Burger, V. Cindro, G. Kramberger, I. Mandic, M. Mikuz, A. Studen, and M. Zavrtanik. Verification of high dose rate ir source position during

brachytherapy treatment using silicon pixel detectors. *IEEE Trans. Nucl. Sci.*, 58(5):2250–2256, October 2011.

[144] H. Song, J. Bowsher, S. Das, and F. Yin. Tracking brachytherapy sources using emission imaging with one flat panel detector. *Med. Phys.*, 36(4):1109–1111, April 2009.

[145] X. Llopart, M. Campbell, D. San Segundo, E. Pernigotti, and R. Dinapoli. Medipix2, a 64k pixel read out chip with 55 μm square elements working in single photon counting mode. *IEEE. Tran. Nucl. Sci.*, 49(5):2279–2283, 2002.

[146] Gisela Anton, Ulrike Gebert, Thilo Michel, and Tilman K. Rügheimer. A hybrid photodetector using the timepix semiconductor assembly for photoelectron detection. *Nucl. Instrum. Methods Phys. Res., Sect. A*, 602(1):205–208, 2009.

[147] C Ponchut and M Ruat. Energy calibration of a cdte x-ray pixel sensor hybridized to a timepix chip. *Journal of Instrumentation*, 8(01):C01005, 2013.

[148] E. Hamann, T. Koenig, M. Zuber, A. Cecilia, A. Tyazhev, O. Tolbanov, S. Procz, A. Fauler, M. Fiederle, and T. Baumbach. Investigation of gaas:cr timepix assemblies under high flux irradiation. *J. Inst.*, 10(01):C01047, 2015.

[149] X. Llopart, R. Ballabriga, M. Campbell, L. Tlustos, and W. Wong. Timepix, a 65k programmable pixel readout chip for arrival time, energy and/or photon counting measurements. *Nucl. Instrum. Methods Phys. Res., Sect. A*, 581(1-2):485–494, 2007.

[150] D Turecek, T Holy, J Jakubek, S Pospisil, and Z Vykydal. Pixelman: a multi-platform data acquisition and processing software package for medipix2, timepix and medipix3 detectors. *Journal of Instrumentation*, 6(01):C01046, 2011.

[151] V Kraus, M Holik, J Jakubek, M Kroupa, P Soukup, and Z Vykydal. Fitpix — fast interface for timepix pixel detectors. *J. Inst.*, 6(01):C01079, 2011.

[152] J. Dammera, P.M. Frallicciardib, J. Jakubeka, M. Jakubeka, S. Pospisila, E. Prenerovac, D. Vavrika, L. Volterd, F. Weydad, and R. Zemekd. Real-time in-vivo μ-imaging with medipix2. *Nucl. Instrum. Methods Phys. Res., Sect. A*, 607(1):205–207, 2009.

[153] Jerrold T. Bushberg, J. Anthony Seibert, Adwin Ml Leidholdt, and John M. Boone. *The Essential Physics of Medical Imaging.* Lippincott Williams & Wilkins, second edition, 2002.

[154] G.F. Knoll. *Radiation Detection and Measurement, 3rd edition.* Wiley, 1999.

[155] J.H. Hubbell, S.M. Seltzer, John H Hubbell, and Stephen M Seltzer. Tables of x-ray mass attenuation coefficients and mass energy-absorption coefficients from 1 kev to 20 mev for elements z = 1 to 92 and 48 additional substances of dosimetric interest. Technical report, National Inst. of Standards and Technology-PL, Gaithersburg, MD (United States). Ionizing Radiation Div., May 1995.

[156] J. Borg and D.W.O. Rogers. Monte carlo calculations of photon spectra in air from ^{192}ir sources. Technical report, Ionizing Radiation Standards, Institute for National Measurement Standards, National Research Council, March 1999.

[157] F. van der Have and F.J. Beekman. Photon penetration and scatter in micro-pinhole imaging: a monte carlo investigation. *Phys. Med. Biol.*, 49(8):1369–1386, 2004.

[158] S. Agostinelli, J. Allison, K. Amako, J. Apostolakis, H. Araujo, et al. Geant4 - a simulation toolkit. *Nucl. Instrum. Methods Phys. Res., Sect. A*, 506(3):250–303, 2003.

[159] J. Allison, K. Amako, J. Apostolakis, H. Araujo, P.A. Dubois, et al. Geant4 developments and applications. *IEEE Trans. Nucl. Sci.*, 53(1):270–278, Feb 2006.

[160] J. Canny. A computational approach to edge detection. *IEEE Trans. Pattern Anal. Mach. Intell*, PAMI-8(6):679–698, Nov 1986.

[161] R. Gonzales and R. Woods. *Digital Image Processing, 2-nd Edition.* Prentice Hall, 2004.

[162] N. Otsu. A threshold selection method from gray-level histogram. *IEEE Trans. Syst. Man. Cyb.*, SMC-9(1):62–64, January 1979.

[163] R. Penrose. A generalized inverse for matrices. *Math. Proc. Cambridge*, 51:406–413, 7 1955.

[164] J.C. Lagarias, J.A. Reeds, M. Wright, and P.E. Wright. Convergence properties of the nelder–mead simplex method in low dimensions. *SIAM J. Optimz.*, 9(1):112–147, 1998.

[165] D.F. Regulla, L.B. Hieber, and M. Seidenbusch. Physical and biological interface dose effects in tissue due to x-ray-induced release of secondary radiation from metallic gold surfaces. *Radiat. Res.*, 150(1):92–100, July 1998.

[166] R. Nadrowitz and T. Feyerabend. Backscatter dose from metallic materials due to obliquely incident high-energy photon beams. *Med. Phys.*, 28:959 – 965, June 2001.

[167] L. Beaulieu, Å.C. Tedgren, J.F. Carrier, S.D. Davis, F. Mourtada, M.J. Rivard, R.M. Thomson, F. Verhaegen, T.A. Wareing, and J.F. Williamson. Report of the task group 186 on model-based dose calculation methods in brachytherapy

beyond the tg-43 formalism: Current status and recommendations for clinical implementation. *Med. Phys.*, 39(10):6208–6236, October 2012.

[168] M.H. Castillo, T.M. Button, R. Doerr, M.I. Homs, C.W. Pruett, and J.I. Pearce. Effects of radiotherapy on mandibular reconstruction plates. *Am. J. Surg.*, 156(4):261–263, October 1988.

[169] M. Farahani, F.C. Eichmiller, and W.L. McLaughlin. Measurement of absorbed doses near metal and dental material interfaces irradiated by x- and gamma-ray therapy beams. *Phys. Med. Biol.*, 35(3):369–385, 1990.

[170] A. Niroomand-Rad, R. Razavi, S. Thobejane, and K.W. Harter. Radiation dose pertubation at tissue-titanium dental interfaces in head and neck cancer patients. *Int. J. Radiat. Oncol. Biol. Phys.*, 34(2):475–480, January 1996.

[171] M. Ravikumar, R. Ravichandran, S. Sathiyan, and S.S. Supe. Backscattered dose perturbation effects at metallic interfaces irradiated by high-energy x- and gamma- ray therapeutic beams. *Strahlenther. Onkol.*, 108(3):173–178, March 2004.

[172] D.W.H. Chin, N. Treister, B. Friedland, R.A. Cormack, R.B. Tishler, G.M. Makrigiorgos, and L.E. Court. Effect of dental restorations and prostheses on radiotherapy dose distribution: a monte carlo study. *J. Appl. Clin. Med. Phys.*, 10(1):80–89, Winter 2009.

[173] I.J. Das and F.M. Kahn. Backscatter dose perturbation at high atomic number interfaces in megavoltage photon beams. *Med. Phys.*, 16(3):367–375, May/June 1989.

[174] I.J. Das and K.L. Chopra. Backscatter dose perturbation in kilovoltage photon beams at high atomic number interfaces. *Med. Phys.*, 22(6):767–773, 1995.

[175] M. Safavi-Naeini, Z. Han, D. Cutajar, S. Guatelli, M. Petasecca, M.L.F. Lerch, D.R. Franklin, J. Bucci, M. Zaider, and A.B. Rosenfeld. Brachyview, a novel inbody imaging system for hdr prostate brachytherapy: design and monte carlo feasibility study. *Med. Phys.*, 40(7):071715, July 2013.

[176] I.S. Kwan, A.B. Rosenfeld, Z.Y. Qi, D. Wilkinson, M.L.F. Lerch, D.L. Cutajar, M. Safavi-Naeni, M. Butson, J.A. Bucci, Y. Chin, and V.L. Perevertaylo. Skin dosimetry with newmosfet detectors. *Radiat. Meas.*, 43(2):929–932, February/June 2008.

[177] S. Sathiyan, M. Ravikumar, and S. S. Supe. Measurement of backscattered dose at metallic interfaces using high energy electron beams. *Rep. Pract. Oncol. Radiother.*, 11(3):117–121, June 2006.

[178] H.O. Anger and D.J. Rosenthal. Scintillation camera and positron camera. *Medical radioisotope scanning*, pages 59 – 75, February 1959.

[179] S. D. Metzler, J. E. Bowsher, M. F. Smith, and R. J. Jaszczak. Analytic determination of pinhole collimator sensitivity with penetration. *IEEE Tran. Med. Imaging*, 20(8):730 –741, August 2001.

Appendix A

Software Documentations

The appendix documents the codes of Matlab functions developed for *HDR BrachyView* project. These functions cover the whole source tracking process, which starts from the image outputted from the readout system of Timepix, ends with the coordinates of the source. The codes with annotation are included below following the consequence of their applications:

- `BV_MultiFindCentre.m`, master function, accomplishes the whole process of source tracking by controlling the implantation of other developed functions.

```
1 function [SP_Info] = BV_MultiFindCentre(varargin)
2 %%
3 %BV_MultiFindCentre find the centre coordinate of source ...
      images from input_image.
4 %BV_MultiFindCentre first filters out pixel with value less ...
      than p*maximum in input_image.
5 %Then group remain pixels into clusters with a radius of R
6 %Then calculate the centre of each cluster
7 %Then Reconstruct all possible source positions
8 %Then calculate the CoM of the whole image
```

```
9  %ind is the index of frames
10 %ff is the flag to control visualization
11 %varargin{1}:imi
12 %varargin{2}: testnumber
13 %varargin{3}: ind of source position
14 %varargin{4}: figure flag
15 %varargin{5}: R
16 %Varargin{6}: P
17 %[SP_Info] = BV_MultiFindCentre(input_image,p,R,ind) returns
18 %SP_Info{1}:CoC: the coordinate of Euclidean centres of source...
       images pixel)
19 %SP_Info{2}:CoM: the coordinate of mass centres of source ...
      images (pixel)
20 %SP_Info{3}:NoC: number of pixel clusters (source images ...
      without selection)
21 %SP_Info{4}:NoPic: number of pixels in each cluster
22 %SP_Info{5}:matrix of initial source positions in volume (mm)
23 %SP_Info{6}:matrix of possible source positions in volume (mm)
24 %Sp_Info{7}:CoM of the whole medfiltered image (mm)
25 %Sp_Info{8}:final source postion in volume
26 %Sp_Info{9}: Distance between first and last CoC
27 %Sp_Info{10}: Distance between first and last CoM
28 %Sp_Info{11}: Distance between each projections
29 %Sp_Info{12}: Sum of distance from source centre to each back ...
      projection
30 %Sp_Info{13}: shift from ideal position of projection 3
31 %%
32 %%%%%%%%%%%%%%%%%%%%%%%%% initial %%%%%%%%%%%%%%%%%%%
33 close all
34 warning off
35 %%%%%%%%%%%%%%%%%%%%%%%%initial parameters
36 ff=0;           %triger of visualization
```

```
37 R=50;            %radius of projection for grouping
38 p=0;             %percentage for threshold
39 th_pre=0.7;      %Global threshold
40 th_reg=1000;     %regional threshold
41 para_gap=0;      %gap between two detectors
42 para_interpW=5; %width of interpilation
43 diskSize=3;      %Module size for erode anddilate
44 CoC_Pre=[];      %initial the rough projection centres of mass
45 distEPAll=[];    %initial distance beween projection centres
46 Ridle=0;         %initial the idle space at right
47 %%
48 %%%%%%%%%%%%%%Define a cell of out put SP_Info
49 SP_Info=cell(1,13);
50 Pre_SP_Info=SP_Info;
51 %%
52 %%%%%%%%%%%%%%%%%%%%%%get input
53 imi=varargin{1};
54 test_number=varargin{2};
55 ind=varargin{3};
56 if nargin>4 || nargin==4
57     ff=varargin{4};
58     if nargin>5 || nargin==5
59     R=varargin{5};
60     if nargin==6
61     p=varargin{6};
62     end
63     end
64 end
65 %%
66 %%%%%%%%%%%%%% h_flag for exp3
67 if test_number==6 || test_number == 9 || test_number == 15 || ...
       test_number == 25
```

```
68      h_flag=29;
69  elseif test_number==7 || test_number == 8 || test_number == 16...
        || test_number == 23
70      h_flag=49;
71  else
72      error('no such test ')
73  end
74  %%
75  %%%%%%%%%%%%%%%%%%%%%%%%%%%preprocessing of image
76  if p>1
77      th_reg=p;
78  end
79  %%
80  %%%%%%%%%%%%%%%%%%%%%%%% save the ori to im_ori and ...
        temp_image
81  %im_ori=input_image;
82  temp_im=imi;
83  %%%%%%%%%%%%%%%%%normalise for each detectors
84  temp_im=BV_NorDoubleD(temp_im);
85  %%%%%%%%%%%%%%%%%%%%%%%%%%%%%%%%correct the gap
86  gap_length=para_gap; %define the length of gap between the 2 ...
        detectors
87  temp_im=BV_GapFix(temp_im,gap_length);
88  %%%%%%%%%%%%%%%%%%%%%%%%%%%%%%%Bilinear interpulation
89  interp_halfWidth=para_interpW;
90  interp_range=[256+1-interp_halfWidth,256+gap_length+...
        interp_halfWidth];
91  % mask high count region between 2 detectors
92  temp_im=BV_Mask_range(temp_im,interp_range);
93  %medfilter on masked image
94  temp_im=medfilt2(medfilt2(medfilt2(temp_im)));
95  % bilinear interpulate the gap
```

```
96  temp_im=BV_Interp_bilinear1D(temp_im,interp_range);
97  %%
98  %%%%%%%%%%%%%%%%%%%%%%%%%store filered img
99  im_prefilt=temp_im;
100 SZ_im_pre=size(im_prefilt);%find the size of prefiltedIm
101 %%
102 %%%%%%%%%%%%%%%%%%%%%%visualization of interpulated image%%%
103 if flag_figure == 1
104     figure;
105     imagesc(temp_im);
106     colormap gray;
107     axis equal;
108 end
109 %%
110 %toc;
111 %%%%%%%%%%%%%%%%%thresholding the back-ground counts
112 %%%%%%%%%%%%%%%%%%%global TH
113 %%
114 %tic;
115 while Ridle<SZ_im_pre(2)
116     temp_im=BV_Thresholding(temp_im,th_pre);
117     %%%%%%%%%%%%%%%%%%visualization of thresholded image
118     if flag_figure == 1
119         figure;
120         imagesc(temp_im);
121         colormap gray;
122         axis equal;
123     end
124     %%
125     %%%%%%%%%%%%%%%%%%%%%%%%regular the shape of projections
126     %tic;
127     if flag_sim==0
```

```
128         mdl=strel('disk',diskSize);   %create a disk model
129         temp_im=imerode(temp_im,mdl); %erode the image with a ...
                disk model
130         temp_im=imdilate(temp_im,mdl);%dilate the image with a...
                 disk model
131         if flag_figure == 1      %visualiation of regulared ...
                projections
132             figure;
133             imshow(temp_im,[]);
134             colormap gray;
135             axis equal;
136         end
137     end
138     %toc;
139     %%
140     %%%%%%%%%%%%%%%%%%%%%%%%%%find projection centres (inpixel...
            )
141     %tic;
142     [Pre_SP_Info{1},Pre_SP_Info{2},Pre_SP_Info{3},Pre_SP_Info...
            {4},Pre_SP_Info{9},Pre_SP_Info{10},Pre_SP_Info{11}]=...
            BV_MultiCentroid(temp_im,R,h_flag,ind);%find source ...
            image mass centre
143     %%
144     %%%%%%%%%%%%%%%%%%%%%%%%%determine the width of idle area
145     clear CoC_Temp
146     CoC_Temp(:,:)=Pre_SP_Info{1}(:,:);
147     if CoC_Temp(:,:)==0;
148         CoC_Temp=[];
149         break;
150     end
151     if size(CoC_Pre)>0
152         if max(CoC_Temp(:,1))-mean(CoC_Pre(:,1))>10
```

```
153             break;
154         end
155
156         if mean(CoC_Pre(:,1))-min(CoC_Temp(:,1))>10
157             break;
158         end
159     end
160     CoC_Pre=[CoC_Pre;CoC_Temp];
161     CoC_Pre=sortrows(CoC_Pre,2);
162     SZ_SPTemp=size(CoC_Temp);
163     SZ_SPInfo1=size(CoC_Pre);
164
165     if SZ_SPTemp>1
166         distEPAll_temp=Pre_SP_Info{11};
167         distEPAll=[distEPAll;distEPAll_temp];
168         distEP=mean(distEPAll);
169     else
170         %distEPAll=200;
171         distEP=200;
172     end
173     Ridle=CoC_Pre(end,2)+distEP;
174     temp_im=im_prefilt;
175     temp_im(:,1:CoC_Pre(end,2)+0.5*distEP)=0;
176     if flag_figure==1
177         imshow(temp_im,[]);
178     end
179 end
180 %%
181 %%%%%%%%%%%%Regional threshold
182 %%%%%%%%%%%%%%%%%initial
183 temp_im=im_prefilt;
184 clear distEP;
```

```
185 SZ_CoC_Pre=size(CoC_Pre);
186 distEP=(CoC_Pre(end,2)-CoC_Pre(1,2))./SZ_CoC_Pre(1);
187 if (CoC_Pre(1,2)-distEP/2)>0
188 temp_im(:,1:floor((CoC_Pre(1,2)-distEP/2))+1)=0;
189 end
190 if floor(CoC_Pre(end,2)+distEP/2)<SZ_im_pre(2)
191 temp_im(:,floor(CoC_Pre(end,2)+distEP/2):SZ_im_pre(2))=0;
192 end
193 %%%%%%%%%%%%%%%%%%%%%%%%%%%%%%%%%%%%%%%%%%%%%%%%%%%%%%%%%%%%
194 if SZ_CoC_Pre(1)>1
195 clear i;
196 last_end=1;
197 for i=1:SZ_CoC_Pre(1)
198     th_reg_start=floor(CoC_Pre(i,2)-distEP/2)-1;
199     th_reg_end=floor(CoC_Pre(i,2)+distEP/2)+1;
200     if th_reg_start>last_end
201         temp_im(:,last_end:th_reg_start)=0;
202     end
203     last_end=th_reg_end;
204     if i==1
205         temp_im(:,1:th_reg_end)=BV_TH_hist(temp_im(:,1:...
                th_reg_end),th_reg,1 );
206     elseif i==SZ_SPInfo1(1)
207         temp_im(:,th_reg_start:end)=BV_TH_hist(temp_im(:,...
                th_reg_start:end),th_reg,1 );
208     else
209         temp_im(:,th_reg_start:th_reg_end)=BV_TH_hist(temp_im...
                (:,th_reg_start:th_reg_end),th_reg,1 );
210     end
211 end
212 end
213 %%%%%%%%%%%%%%%%%%visualization of thresholded image
```

```
214 if flag_figure == 1
215     figure;
216     imagesc(temp_im);
217     colormap gray;
218     axis equal;
219 end
220 %%
221 %%%%%%%%%%%%%%%%%%%%%%%%regular the shape of projections
222 %tic;
223 if flag_sim==0
224     mdl=strel('disk',diskSize);   %create a disk model
225     temp_im=imerode(temp_im,mdl); %erode the image with a disk...
          model
226     temp_im=imdilate(temp_im,mdl);%dilate the image with a ...
         disk model
227     if flag_figure == 1      %visualiation of requlared ...
         projections
228         figure;
229         imagesc(temp_im);
230         colormap gray;
231         axis equal;
232     end
233 end
234 %toc;
235 %%
236 %%%%%%%%%%%%%%%%%%%%%%%%%find projection centres (inpixel)
237 %tic;
238 [SP_Info{1},SP_Info{2},SP_Info{3},SP_Info{4},SP_Info{9},...
      SP_Info{10},SP_Info{11}]=BV_MultiCentroid(temp_im,R,h_flag...
      ,ind);%find source image mass centre
239     %%%%%%%%%%%%%%%%%%%%%%%%%%%%%%%%%%%%%%%%%%%%%%%%%%%%%%%%
240     [SP_Info{5},SP_Info{6},SP_Info{12}]=BV_3DRecon(SP_Info{1})...
```

```
        ;
241     %toc;
242     %%%%%%%%%%%%find the COM of the whole image%%%%%%%%%%%%
243     %tic;
244     if special_flag==15
245     temp_im=whole_im;
246     end
247     [SP_Info{7}]=BV_FindCOMwhole(temp_im);
248     %toc;
249     %%%%%%%%%%%find the final source position in volume...
            %%%%%%%%
250     %tic;
251     SP_Info{8}=BV_ChooseSP(SP_Info{6},SP_Info{7});
252     %toc;
253 end
```

- `BV_GapFix.m`, corrects the gap betwen different detectors if necessary.

```
1  function [ imo ] = BV_GapFix( imi,Gap_length)
2  % This fucntion fix if a gap is existing between the detectors
3  % imi: input image
4  % Gap_length: gap length IN PIXEL
5  % imo: output image
6  GL=Gap_length;
7  SZ_imi=size(imi); %get the size of input image
8  SZ_imo=SZ_imi;
9  SZ_imo(2)=SZ_imo(2)+GL; %calculate the size of output image
10 %fill the gap between the detectors with 0
11 imo=zeros(SZ_imo);
12 imo(:,1:256,:,:)=imi(:,1:256,:,:);
13 imo(:,257+GL:512+GL,:,:)=imi(:,257:512,:,:);
```

```
14
15 end
```

- `BV_Interp_bilinear1D.m`, interpolates the masked region.

```
1  function [ imo ] = BV_Interp_bilinear1D( imi,range)
2  %This function interpolate the masked columns
3  %imi: input image
4  %range: start and end of the columns will be interpolated
5  r=[252,260];
6  if range
7      r=range;
8  end
9  %linear interpolation
10 imo=imi;
11 R=r;
12 R(1)=r(1)-1;
13 R(2)=r(2)+1;
14 for i=r(1):r(2)
15     F1=(R(2)-i)/(R(2)-R(1));
16     F2=(i-R(1))/(R(2)-R(1));
17     imo(:,i,:,:)=imo(:,R(1),:,:).*F1+imo(:,R(2),:,:).*F2;
18 end
19 end
```

- `BV_Thresholding.m`, isolates source projections by thresholding the image according to a pre-set percentage of maximum count in the image.

```
1  function imo=BV_Thresholding(imi,t)
```

```
2  %This function filter out pixel value smaller than t* the ...
       maxium counts
3  %imi: input image
4  %t: threshold in percentage
5  %imo: output image
6  %Value in imo =0 if the value with same position in imi is ...
       less than t* maximum value of imi
7  %Value in imo = the value with same position in imi, if this ...
       value is larger or equal to t* maximum value of imi
8  imo=imi; %copy imi to imo
9  Max_imi=max(max(imi)); %calculate the maximum of imi
10 th_index= imi< t*Max_imi; %find index of pixel with value ...
       smaller than threshold
11 imo(th_index)=0;
12 end
```

- BV_TH_hist.m, isolates source projections by thresholding the image according to its histogram.

```
1  function [ imo ] = BV_TH_hist(imi,ts,flag_dir)
2  % threshold the image based on its accumulated histram
3  % imi: input image
4  % ts: the amount of pixels that will be kept/removed by the ...
       thresholding
5  % flag_dir: falg determine the operation of keep or remove;
6  % 1 means keep; -1 means removed
7  imo=imi; %copy input_image to output_image
8  if max(imi(:))>100
9      n_bins=max(imi(:));
10 else
11     n_bins=1000;
```

```
12 end
13 hist_imi=hist(imi(:),n_bins); %histgram of imi
14 Cum_hist_imi=cumsum(hist_imi); % cumulative integral of ...
      histgram of imi
15 mx_cumh_imi=sum(hist_imi); %calculate the total number of ...
      pixels
16 %find the counts value that there are ts of pixels have the ...
      counts above it
17 th=find(Cum_hist_imi>mx_cumh_imi-ts, 1 );
18 switch flag_dir
19     case 1
20         %find index of pixel with value smaller than threshold
21         th_index= imi < th;
22     case -1
23         %find index of pixel with value bigger than threshold
24         th_index= imi > th;
25 end
26 imo(th_index)=0;
27 end
```

- `BV_Mask_range.m`, masks the abnormal high counts region at the connection of the detectors.

```
1 function [ imo ] = BV_Mask_range( imi,range)
2 %This function masks the abnormal columns with 0
3 %imi: input image
4 %range: start and end of abnormal columns
5 r=[252,260];% default start and end of abnormal columns
6 if range
7     r=range;
8 end
```

```
9  %masks the abnormal columns with 0
10 imo=imi;
11 imo(:,r(1):r(2),:,:)=0;
12 end
```

- `BV_MultiCentroid.m`, locates the centre of mass of all the projections. It is able to recognise and group the pixels clusters (source projections) in any two dimensional distribution of clusters. Either continue or discrete clusters could be resolved. This function is only applicable in case that the diameter of the cluster is smaller than the minimum distance between the cluster centres.

```
1  function [CCoC,CCoM,NoC,NoPiC,DistC,DistM,DistEP]=...
       BV_MultiCentroid(input_image,R)
2  %BV_MultiCentroid find the centre of source projections from ...
       input_image.
3  %input_image is thresholded image with all pixel value equal ...
       to 0 except
4  %source projections(clusters). R is the radius to determine a ...
       cluster.
5  %[CoC CoM NoC] = BV_MultiFindCentre(input_image,p,R) returns
6  %CoC: the coordinate of Euclidean centres of source ...
       projections
7  %CoM: the coordinate of mass centres of source projections
8  %NoC: number of pixel clusters (source projections)
9  if nargin==1
10     R=50;                                          %set default R
11 end
12 %%
13 %%%%%%%%%%%%%%%%%%%% Initialization
14 clear CoC CoM NoC CoPiC DistC DistM DistEP;
```

```
15 if max(max(input_image))==0
16     NoC=0; CCoM=0; NoPiC=0; CCoC=0;
17     DistC=0;
18     DistM=0;
19     DistEP=0;
20 else
21 temp=input_image;
22 sizeIm=size(input_image);
23 iniflag=0;
24 for i=1:sizeIm(1)
25     if iniflag==1
26         break;
27     end
28     for j=1:sizeIm(2)
29         if temp(i,j)~=0
30             iniflag=1;
31             CoC(1,1)=i;     %set first non-zero pixel as centre...
                   of cluster1
32             CoC(1,2)=j;
33             CoM(1,1)=i;
34             CoM(1,2)=j;
35             NoC=1;          %Set Number of clusters as 1
36             NoPiC(1)=0;     %Set Number of pixels in cluster1 ...
                  as 0
37             MoPiC(1)=0;     %Set Mass of pixels in cluster1 as ...
                  0
38             %break;
39         end
40     end
41 end
42 clear i j;
```

```
43 %% Group the cluster of pixels corresponding to each ...
       projection and
44 %% calcualte the centre
45 for i=1:sizeIm(1)             %scan image matrix in vertical ...
       dir
46 for j=1:sizeIm(2)         %scan image matrix in horizontal dir
47 if temp(i,j)~=0       %find non-zero pixel
48    flagiC=0;
49 %check distance of cerrent pixel to existing cluster euclidean...
        centres
50    for k=1:NoC
51        if (i-CoC(k,1))^2+(j-CoC(k,2))^2<R^2
52            flagiC=1;
53            %calculate euclidean centres
54            CoC(k,1)=(CoC(k,1)*NoPiC(k)+i)/(NoPiC(k)+1);
55            CoC(k,2)=(CoC(k,2)*NoPiC(k)+j)/(NoPiC(k)+1);
56            NoPiC(k)=NoPiC(k)+1;
57            %Calculate Mass centre
58            CoM(k,1)=(CoM(k,1)*MoPiC(k)+i*temp(i,j))/(MoPiC(k)+...
                  temp(i,j));
59            CoM(k,2)=(CoM(k,2)*MoPiC(k)+j*temp(i,j))/(MoPiC(k)+...
                  temp(i,j));
60            MoPiC(k)=MoPiC(k)+temp(i,j);
61            %break;
62        end
63    end
64
65 %when current pixel don't belong to all existing clusters, ...
       create a new
66 %cluster, then initialize.
67    if flagiC==0
68            NoC=NoC+1;
```

```
69              CoC(NoC,1)=i;
70              CoC(NoC,2)=j;
71              CoM(NoC,1)=i;
72              CoM(NoC,2)=j;
73              NoPiC(NoC)=1;
74              MoPiC(NoC)=temp(i,j);
75      end
76  end
77  end
78  end
79  %%
80  %remove cluster whos size were smaller than 10 pixels
81  clear i j;
82  threshSize=50;
83  j=0;
84  for i=1:NoC
85      if NoPiC(i)>threshSize
86          j=j+1;
87          CCoC(j,:)=CoC(i,:);
88          CCoM(j,:)=CoM(i,:);
89          NNoC=j;
90          %NoPiC(i)=[];
91          %i=i-1;
92      end
93  end
94  if ~exist('CCoC','var')
95      CCoC=[0,0;0,0];
96      CCoM=[0,0;0,0];
97  end
98  if size(CCoC,2)~=2;
99      CCoC=[0,0;0,0];
100     CCoM=[0,0;0,0];
```

```
101 end
102 %%
103 %%%%%%%%%%%%%%%%%%%%%%%%sort the matrix
104 CCoC=sortrows(CCoC,2);
105 CCoM=sortrows(CCoM,2);
106 %%
107 %%%%%%%%%%%%%remove projection close to the edge of left ...
       detector
108 if ind<51
109     if CCoC(1,2)<1
110         CCoC(1,:)=[];
111         CCoM(1,:)=[];
112     end
113 else
114     if CCoC(1,2)<40
115         CCoC(1,:)=[];
116         CCoM(1,:)=[];
117     end
118 end
119
120 if h<19
121     if CCoC(1,2)<50
122         CCoC(1,:)=[];
123         CCoM(1,:)=[];
124     end
125 end
126 %%
127 SzC=size(CCoC);
128
129 DistC=max(CCoC(:,2))-min(CCoC(:,2));
130 DistM=max(CCoM(:,2))-min(CCoM(:,2));
131 DistEP=zeros(1,SzC(1)-1);
```

```
clear i
for i=1:SzC(1)-1
    DistEP(i)=CCoC(i+1,2)-CCoC(i,2);
end

end
end
```

- BV_3DRecon.m, calculates all the possible source positions in volume.

```
function [ pp, mindis ] = BV_3DRecon( CentPs)
% This function solves the source position in volume
% CentPs: the array of projection centres IN PIXEL
% CentPs should be sorted by its 2nd column
% pp: store all the possible source positions in volume
% mindis: the sum distance from the calculated source centre ...
    to all the
% line of interest
clear i Sx Sy Pinhole P;
%%
% %%%%%%%%%%%%%%%%%%%%%%%%use only 2 projections
% if Sc(1)>2
%     Sc(1)=2;
%     %Sc(1)=3;
% end

%%%%%%%%%%%%%%%check number of centres
 if Sc(1) > 7 || Sc(1)<2
%set an impossible value in case of the number centre is not a...
     a resolvable
%range to prevent expected interruption
```

```
20        pp=[-50 -50 -50];
21        mindis=0;
22     %end
23     else
24 %%
25 %%%%%%%%%%%%%%% get array of projections centre
26 PC3D=zeros(Sc(1),3);
27 %%%%%%%%%%%%%%%%%%%%%transfer the coordinate of CoM on ...
       detector (in pixel) to the coordinate in volume (in mm) ...
       %%%%%%%%%%%%%%%%%%%%%%
28 PC3D(:,1)=(MCentPsX+Xpd-0.5).*0.055-7;
29 PC3D(:,2)=19.5-(CentPs(1:Sc(1),2)+Ypd-0.5).*0.055;
30 PC3D(:,3)=0-Hdp;
31 %%
32 %%%%%%%%%%%%%%%define pinhole positions
33 Pinhole=zeros(7,3);
34 for i=1:7
35     Pinhole(i,:)=[0 39-(i-1).*dpin 0];
36 end
37 %%
38 %%%%%%%%%%%%%%%% reconstruct all possible source contre
39 %create symbolic variable of temp source centre in volume
40 Symp=sym(zeros(Sc(1),3));
41 Symp(:,1)=sym('Sympp(1)');
42 Symp(:,2)=sym('Sympp(2)');
43 Symp(:,3)=sym('Sympp(3)');
44 SymPinhole=sym(Pinhole);
45 %%%%%%%sort series of pinhole&projection groups
46 pp=zeros(8-Sc(1),3);
47 ppinit=zeros(8-Sc(1),3);
48 mindis=zeros(8-Sc(1),1);
49 for j=1:8-Sc(1) %%%7-Sc(1)+1
```

```
50 %protential source centres in volume in each pinhole&...
       projection group
51      clear Dir Pinit;
52      Dir=Pinhole(j:j+Sc(1)-1,:)-PC3D;   %get direction of each ...
           projection
53 %get a init source position for searching poition with minimum...
        with fixed X
54  A=[Dir(1,2) -1.*Dir(2,2);Dir(1,3) -1.*Dir(2,3)];
55  B=[Pinhole(j+1,2)-Pinhole(j,2);Pinhole(j+1,3)-Pinhole(j,3)];
56
57  r=A\B;
58  Pinit=Pinhole(j,:)+r(1).*Dir(1,:);
59  ppinit(j,:)=Pinit;
60 %distance to all projection
61 %create symbolic variable of dirctions and temp source centre ...
       in volume
62      SymDir=sym(Dir);
63      SymPV=Symp-SymPinhole(j:j+Sc(1)-1,:);
64 %distances from the temp source centre to each back ...
       projections
65     % tic; %% 0.05 s
66      for i=1:Sc(1)
67          TempDSP(i)=norm(cross(SymDir(i,:),SymPV(i,:)))./norm(...
               SymDir(i,:));
68      end
69     % toc;
70 %Sum of the distance and find the minimum
71     % tic;
72      Sum_TempDSP=sum(TempDSP);
73      Char_Sum_TempDSP=char(Sum_TempDSP);
74      f_Sum_TempDSP=eval(['@(Sympp)' Char_Sum_TempDSP]);
```

```
75      [pp(j,:),mindis(j),exi_flag]=fminsearch(f_Sum_TempDSP,...
            Pinit());
76      %pp is the matrix of possible source centre in volume
77      if exi_flag==0
78          pp(j,:)=[-50 -50 -50];
79      end
80  %%directly calculate z use distance between first and last CoC
81  %MeanDistc=(max(PC3D(:,2))-min(PC3D(:,2)))./(Sc(1)-1);
82  %pp(j,3)=dpin.*Hdp./(MeanDistc-dpin);
83  % toc;
84  end
85  end
86  end
```

- BV_ChooseSP.m, chooses the correct source position in volume.

```
1  function [ SP_Inf7 ] = BV_ChooseSP( pp,CoM_whl )
2  %This function choose the right source position in volume ...
       based on the mass
3  %centre of the whole image
4  %pp: possible source centres in volume
5  %CoM_whl: centre of mass of the whole image
6  %SP_Inf7: choose source centre in volume
7  clear size_pp M_d M_dd SP_Inf7
8  size_pp=size(pp);
9  M_d=zeros(size_pp(1),2);
10 %colulate the distance between the source centre and the CoM ...
       of the whole
11 %image in plane of XY
12 M_d(:,1)=CoM_whl(1)-pp(:,1);
13 M_d(:,2)=CoM_whl(2)-pp(:,2);
```

```
14 M_dd=sum(M_d.^2,2).^0.5;
15 %choose the source centre position with minimun distance to ...
      the CoM of the
16 %whole image
17 SP_Inf7=pp(M_dd==min(M_dd),:);
18 end
```